Investigation of Uncertainties Associated with the MammoSite™ Breast Brachytherapy Technique: Monte Carlo Simulations and TLD Measurements

Saleh M Ben Saleh

Thesis submitted for the degree of
Doctor of Philosophy
in
The School of Chemistry and Physics,
The University of Adelaide

Supervisors
A/Prof. Eva Bezak
Dr. Martin Borg

November 2010

Contents

3. Modelling of high dose rate ^{192}Ir brachytherapy source 38

4. Uncertainties in source position and balloon deformation and their impact on NTCP and TCP 51

5. Uncertainty in contrast concentration inside the MammoSite balloon: Monte Carlo simulations and thermoluminescent dosimetry measurements 69

Part one: Monte Carlo simulation 69

Part two: Thermoluminescent dosimetry measurements **78**

8. Conclusions and further work 131

Appendix 136

Bibliography 150

List of Tables

List of Figures

Page

Page

Page

Abstract

The MammoSite Radiation Therapy System is a novel brachytherapy technique for treatment of patients with early stage breast cancer. It is used as a sole radiation treatment or in combination with external beam radiotherapy. There are several uncertainties associated with the dose distribution from the MammoSite brachytherapy.

In this research study, the ^{192}Ir brachytherapy source was accurately modelled using the EGSnrc Monte Carlo code. A voxel size of 1.5 mm^3 was found to be suitable for dose calculations as reducing the voxel size any further would increase the simulation time without improving the accuracy of dose simulation.

The impact of uncertainties in balloon deformation and source position on the tumour control probability (TCP) and the normal tissue complication probability (NTCP) were assessed. The effects on the treatment outcome were assessed from (a) organ differential dose volume histograms (dDVHs) obtained from the Plato brachytherapy planning system and (b) EGSnrc Monte Carlo simulations based on actual computed tomography (CT) images of a breast cancer patient who underwent MammoSite brachytherapy treatment.

This study gave low probabilities for developing heart and lung complications.
Monte Carlo calculations showed that a deviation of the source by 1 mm caused approximately 7% dose reduction in the treated target volume at 1 cm from the balloon surface. A 4 mm source deviation produced underdosing of some portions of the PTV by 40% leading to poor treatment outcomes. Furthermore, 4 mm uncertainty in source deviation leads to overdosing of regions of the PTV by about 40%. This results to an excessive dose to the skin and increases the probability of skin complications.

Balloon deformation and incorrect source position had significant effect on the prescribed dose within the treated volume. A 4 mm balloon deformation resulted in reduction of the tumour control probability by 24%. The current study suggested that

the MammoSite treatment protocols should allow for a balloon deformation of less than 2 mm and a maximum source deviation of ≤ 1 mm.

The extent of the dose perturbation for various concentrations of the contrast medium in a MammoSite balloon was investigated using Monte Carlo simulations and thermoluminescent dosimeters (TLDs) measurements. The Monte Carlo simulation was performed using CT images of in-house tissue equivalent breast phantom. The breast phantom was also used for TLD measurements.

The measured and Monte Carlo calculated doses were in agreement within the measurement uncertainty and Monte Carlo statistical errors. The dose reduction resulting from the use of high atomic number contrast (Iodine) caused considerable uncertainty in the MammoSite dose. Our results showed that 100%, 50% and 15% contrast concentrations reduced the dose at the prescription point by 10%, 5% and 2% respectively relative to the dose calculated with the balloon filled with saline (water) only.

The BEAMnrc and DOSXYZnrc Monte Carlo codes were used to model an external beam radiotherapy treatment and simulate a dose distribution using a patient CT data set respectively. The external beam radiotherapy model was validated with measurements and the data analysis was performed using the gamma function algorithm.

The gamma function analysis algorithm was used and the acceptance criteria for comparison were set to distance-to-agreement of 2 mm and 2% dose difference. An excellent agreement (99.4% of detectors passed the criteria) was found between the Monte Caro computed dose maps and the measured ones. This proved that a reliable Monte Carlo model was constructed and used for dose calculations from EBRT treatment. The simulated dose distribution from EBRT was combined with the simulated MammoSite dose distribution.

Finally, it would be beneficial (to the oncologist) to visualize the final (combined) dose distributions from the two modalities to assist with an assessment of treatment plans and the treatment outcome. Currently, combining the dose distributions from the two modalities is difficult to achieve because the two modalities use different planning systems and different dose calculations algorithms and the patient anatomy looks different (balloon is present for brachytherapy). Consequently, the project aimed to build a Monte Carlo linac model to calculate dose delivery to a breast due to external beam radiotherapy.

Having MC models (EBRT & MB) constructed and verified, the dose distributions calculated from each modality were converted using appropriate algorithms to equivalent dose distributions and combined to yield the total dose distribution to a breast from the combined treatment.

Signed Statement

This work contains no material which has been accepted for the award of any other degree or diploma in any university or other tertiary institution and, to the best of my knowledge and belief, contains no material previously published or written by another person, except where due reference has been made in the text.

I consent to this copy of my thesis, when deposited in the University Library, being available for loan and photocopying.

SIGNED: ………………….……………… DATE: ……………………………….……

Acknowledgements

I wish to acknowledge the scholarship support of the Libyan government, which made this project possible.

I am extremely grateful to have had A/Prof. Eva Bezak as my principal supervisor. She was always available to discuss issues related to my project. She taught me the skills of a researcher. Her guidance, intelligence and support were invaluable. I would also like to express my sincere gratitude to my co-supervisor Dr. Martin Borg for his clinical advice.

I strongly appreciate the encouragement, moral support and help from the staff of the Medical Physics Department at the Royal Adelaide Hospital: Thomas Rutten, Daniel Ramm, John Lawson, John Schneider, Tim Willams, Kim Quach, Scott Penfold, Raelene Nelligan, Siva Saranandarajah, Mohammad Mohammadi and Christine Robinson. A special thanks to Dr. Justin Shepherd for proof reading the thesis.

I would also like to thank Thuc Pham for sharing his knowledge of the Monte Carlo technique with me. Special thanks to Hologic Corporation who have supplied me with their MammoSite images.

My friendship with my fellow graduate students has been a delightful part of my life.

Finally my greatest thanks go to my family for their love and support.

Publications in refereed journals

The work in this thesis has been published and presented in the following:

1. Saleh benSaleh, Eva Bezak and Martin Borg, “Review of MammoSite brachytherapy: Advantage, disadvantages and clinical outcomes”. Acta Oncologica 48: 487-494 (2009).
2. Saleh benSaleh, Eva Bezak and Thuc Pham, “Combined Dose Distribution for External Beam Whole Breast Irradiation and MammoSite Breast Brachytherapy: Monte Carlo Investigation” published in Proceedings of Medical Physics and Biomedical Engineering World Congress 2009.
3. Bensaleh S and Bezak E. Investigation of source position uncertainties & balloon deformation in MammoSite brachytherapy on treatment effectiveness. Australas Phys Eng Sci Med 2010; 33:35-44.

Papers submitted to refereed journals

Bensaleh S, Bezak E, “The effect of uncertainties associated with MammoSite® brachytherapy on the dose distribution in the breast: Monte Carlo simulations and TLD measurements” submitted to Brachytherapy.

Papers in preparation

Bensaleh S, Bezak E, “Combined dose distribution for MammoSite brachytheray and external beam breast irradiation” to be submitted to Medical Physics.

Conference presentations

International

1. Saleh benSaleh and Eva Bezak “MammoSite Brachytherapy Tecnique Review, Monte Carlo Modelling and Measurements of Uncertainties” International Conference on Medical Physics, Radiation Protection and Radiobiology (2009), Feburary11-13, Jaipur, India [Invited Paper].

2. Saleh benSaleh, Eva Bezak and Thuc Pham, “Combined Dose Distribution for External Beam Whole Breast Irradiation and MammoSite Breast Brachytherapy: Monte Carlo Investigation” Medical Physics and Biomedical Engineering World Congress 2009. Munich, Germany.

National

1. Saleh benSaleh, Eva Bezak and Martin Borg, “Dose Investigation of the MammoSite Applicator using Monte Carlo Method”. Engineering and Physical Science in Medicine (2007), October 14-18, Fremantle, Western Australia.

2. Saleh benSaleh and Eva Bezak, “Investigation of the Dose Reduction in the Breast due to Various Contrast Concentrations in the MammoSite Balloon: Monte Carlo Simulations and TLD Measurements”. Engineering and Physical Science in Medicine (2008), November 16-20, Christchurch, New Zealand.

3. Saleh benSaleh and Eva Bezak, “The Effect of Source Positioning Errors on TCP & NTCP in MammoSite® Breast Brachytherapy”. Engineering and Physical Science in Medicine (2008), November 16-20, Christchurch, New Zealand.

4. Saleh benSaleh and Eva Bezak, “Quantitative Analysis of Dose Reduction in MammoSite Brachytherapy Breast Cancer Technique by Monte Carlo Simulations”. Australian Institute of Physics 18th National Congress (2008), November 30th – December 5th, Adelaide, South Australia.

5. Saleh benSaleh and Eva Bezak, “Monte Carlo Modelling of Combined Dose Distributions in Breast Radiotherapy” Engineering and Physical Science in Medicine (2009), November 8-12, Canberra, Australia.

6. Bensaleh S, Bezak E. Dose equivalent for the combination of external beam breast irradiation and MammoSite breast brachytherapy: Monte Carlo simulations. 3rd Modelling of Tumour (MOT) Meeting. 2010. Adelaide, Australia.

Other presentations

1. Saleh benSaleh and Eva Bezak, “Dose Uncertainties in MammoSite Breast Brachytherapy” Postgraduate Student Papers Night. Adelaide, Australia. 2006. Sponsored by ACPSM, SAMBE and EACBE (SA branches) [**].

2. Saleh benSaleh, Eva Bezak and Martin Borg, “Dose Investigation of the MammoSite Applicator using Monte Carlo Method” Postgraduate Student Papers Night. Adelaide, Australia. 2007. Sponsored by ACPSM, SAMBE and EACBE (SA branches) [*].

3. Saleh benSaleh and Eva Bezak, “Investigation of the Effects of Contrast Medium on the MammoSite Dose distribution: Monte Carlo Simulations and TLD Measurements”. Student Paper Competition 2008, sponsored by the South Austral Branch of the Australian Radiation Protection Society.

* Awarded first prize

**Awarded second prize

TO MY FAMILY

Chapter 1

General introduction

1.1 Breast cancer & radiotherapy

Breast cancer is the main cancer causing deaths among women worldwide. According to the World Health Organization (WHO), breast cancer accounts for about 519,000 deaths each year [1]. Breast cancer can be cured if it is detected early and patients receive effective treatment. A common treatment for early stage breast cancer involves surgery (lumpectomy) and radiotherapy. Surgery involves the removal of the tumour and some of the surrounding tissues. Radiotherapy is employed to eliminate any residual cancer cells within the tumour volume. One method of irradiating the tumour bed is by using external beam radiotherapy (EBRT). Traditionally external beam whole breast irradiation is usually administered 5 days per week daily over a 5-7 week course. At present accelerated partial breast irradiation (APBI) is also increasingly used. One form of APBI uses the MammoSite radiation therapy system (Hologic, Marlborough, MA) as a sole radiation treatment or in combination with EBRT for patients with early stage breast cancer following lumpectomy.

1.1.1 MammoSite bracytherapy

The MammoSite applicator is a radionuclide applicator specifically designed to deliver brachytherapy to the site of the local breast tumour resection. Generally, the MammoSite applicator is used for treatment of patients diagnosed with ductal carcinoma in situ (DCIS), invasive ductal carcinoma (IDC) and a primary tumour of size ≤ 3 cm. Chapter 2 of this thesis describes the MammoSite brachytherapy technique in more details. Briefly, the device consists of a small balloon (4-5 cm in diameter) connected to an inflation channel and a catheter for the passage of a high dose rate ^{192}Ir brachytherapy source, see Figure 1.1. The device is placed into the tumour resection cavity and inflated with a mixture of saline and radiographic contrast agent to a size that fills the cavity. The ^{192}Ir brachytherapy source is placed at the centre of the balloon through a remote afterloader to deliver dose to the treated volume.

Figure 1.1. The MammoSite® Radiation Therapy System, courtesy of Hologic Corporation and affiliates.

1.1.2 Uncertainties in MB

There are several uncertainties associated with the dose distribution from the MammoSite brachytherapy (MB). They include balloon deformation, source deviation and the concentration of the contrast medium inside the balloon. These parameters need to be thoroughly investigated as they represent significant impact on the treatment efficacy. The EGSnrc Monte Carlo code is used in the current study to investigate the impact of these parameters on the dose distribution in the breast. The Monte Carlo simulation is performed using computed tomography (CT) images of a patient. Measurements with lithium fluoride thermoluminescent dosimeters (LiF TLD) are also conducted to validate the Monte Carlo simulations.

1.1.3 Combining MB and EBRT

For some patients, different radiation treatment modalities are combined to prevent the risk of the probability of tumour recurrence and to reduce tissue complications. At our institution, patients with early stage breast cancer were treated with the combination of MB and EBRT. The MB was used as a boost with prescriptions of 9-10 Gy at 10 mm from the balloon surface in two fractions of 4.5-5 Gy at least 6 h apart [2]. EBRT commenced 1-5 days after MB. During the EBRT procedure a total of 50 Gy was prescribed to the isocentre, at 2 Gy per fraction, using tangential fields and 6 MV photons, in 5 weeks, following the departmental protocol [3]. The treatment planning was done separately for each modality using different treatment planning systems. For EBRT, the treatment plan was generated using the Pinnacle^3 treatment planning system (v6.26, Phillips Medical Systems). At our institution, the MammoSite brachytherapy treatment planning is performed with the Nucletron Plato's treatment planning system (Plato BPS v14.3.2, Nucletron B-V., Veenendaal, The Netherlands). It would be highly beneficial to combine the final dose distributions from the two modalities to assist with an assessment of the treatment plans and of the treatment outcome.

1.2 Aims of the current thesis

Uncertainties associated with the MammoSite brachytherapy may alter the prescribed dose within the treated volume. They may also expose the normal tissues in balloon proximity to excessive dose. The aim of this thesis is to investigate the impact of these uncertainties on the dose distribution in the breast using dose volume histograms and Monte Carlo simulations. The Lyman-Kutcher and relative seriality models are employed to estimate the normal tissues complications associated with the MammoSite dose distributions. The tumour control probability is calculated using the Poisson model.

Furthermore, this study developed two separate Monte Carlo models for MB and EBRT techniques. The Monte Carlo models were validated with measurements. The Monte Carlo dose distributions, for the two models, were calculated using patient CT datasets. This study also developed a technique for combing the dose distributions from the MammoSite brachytherapy and external beam radiotherapy techniques.

1.3 Thesis outline

Chapter 1 describes briefly the radiotherapy techniques used for treatment of early stage breast cancer.

In chapter 2 part one, a review of the literature related to the MammoSite brachytherapy of the breast cancer is given. Potential issues of the MammoSite dosimetry, cosmetic outcomes and treatment complications associated with the use of the technique are discussed. In chapter 2 part two, the use of Monte Carlo methods in radiotherapy is discussed.

Chapter 3 discusses the use of DOSXYZnrc Monte Carlo in the current work for modelling of the ^{192}Ir high dose rate brachytherapy source. It also contains the determination of the suitable voxel size for the calculation of dose distribution around the ^{192}Ir source.

Chapter 4 contains investigation of the source position and balloon deformation uncertainties and their impact on the MammoSite treatment outcome. The impact is assessed through the use of the radiobiological models of normal tissue complication probability (NTCP) and normal tissue complication probability (TCP).

Chapter 5 concerns with the impact of the contrast medium inside the MammoSite balloon on the dose distribution in the breast. Here the contrast media is modelled within the Monte Carlo code and the simulations are based on the CT data of a designed breast phantom. Also, LiF TLD detectors are used for the measurements of the dose perturbations caused by the contrast media. The chapter concludes by comparing the Monte Carlo simulations with TLD measurements.

Chapter 6 describes the use of EGSnrc / BEAMnrc Monte Carlo code in the current work for modelling of a clinical accelerator (Varian 600 C/D). The model is validated with measurements.

Chapter 7 is dedicated to combining the dose distributions from the MammoSite technique and external beam breast radiotherapy. The Monte Carlo model for external beam radiotherapy is constructed from a patient treatment plan. The concepts of the biological equivalent dose and equivalent dose are used to do the dose combination.

Chapter 8 provides a conclusion of the thesis and suggestions for future research.

Chapter 2

Literature review

Part one: MammoSite brachytherapy technique

2.1.1 Introduction

Breast cancer is the main cancer causing deaths among women worldwide. According to the World Health Organization (WHO), breast cancer accounts for 519,000 deaths each year [1]. Breast cancer can be cured if it is detected early and patients receive effective treatment. For patients with early stage (I or II) breast cancer, breast conserving therapy (BCT) is the most commonly employed treatment technique. It consists of the removal of breast tumour surgically (lumpectomy) followed by radiotherapy treatment course. Different radiotherapy modalities are available and include external beam radiotherapy (EBRT) to the whole breast, 3D conformal radiotherapy (3D-CRT), intra-operative radiotherapy, interstitial brachytherapy, and more recently MammoSite brachytherapy. This chapter describes the use of MammoSite brachytherapy technique for the treatment of early stage breast cancer.

2.1.2 External beam whole breast irradiation

The accepted approach to BCT for early stage breast cancer is the surgical removal of the primary breast lesion followed by 6 to 6.5 weeks course of external beam irradiation to the whole breast with or without a boost. Conventional whole breast irradiation technique commonly uses two tangential parallel opposed beams with lateral and medial wedges targeting the entire breast. Evidence from studies has shown that long-term survival after breast conserving surgery (BCS) and radiation therapy is equivalent to survival after mastectomy [4-8]. Although this is a successful and well accepted treatment, many patients choose to avoid whole breast irradiation as a result of the time and travel difficulties they are unable to overcome [9]. To tackle this problem, Accelerated Partial Breast Irradiation (APBI) has been introduced as an alternative treatment method for patients with early stage breast cancer.

2.1.3 Accelerated partial breast irradiation

Accelerated partial breast irradiation is a technique in which the tissue surrounding the lumpectomy cavity receives high radiation dose in short treatment time. There are several techniques that can deliver APBI including interstitial brachytherapy, three dimensional conformal radiotherapy, intra-operative radiotherapy, and MammoSite brachytherapy.

2.1.4 MammoSite brachytherapy technique

A novel brachytherapy form of APBI has been developed in recent years [10]. This technique uses the MammoSite brachytherapy system (Hologic, Marlborough, MA) as a sole radiation treatment for patients with early stage breast cancer following lumpectomy. It consists of a small balloon connected to a catheter which has an inflation channel and a catheter for the passage of a high dose rate brachytherapy source (Ir-192) shown in Figure 2.1. The device is placed in the lumpectomy cavity during or following breast surgery [10]. The MammoSite balloon is inflated with the sterile saline with a small amount of radiographic contrast to a size that both completely fills the cavity and ensures conformance of the tissue to the balloon [11, 12]. Then a Computed Tomography (CT) scans are obtained to assess balloon conformance to the lumpectomy cavity and to determine the distance from the surface of the balloon to the skin, the symmetry, diameter of the inflated balloon, the planning target volume and the dose distribution [10]. The treatment with the MammoSite device is generally 34 Gy delivered in 10 fractions (3.4 Gy/fraction twice daily) at 1.0 cm from the balloon surface with minimum of 6 hours between fractions on the same day [10, 13].

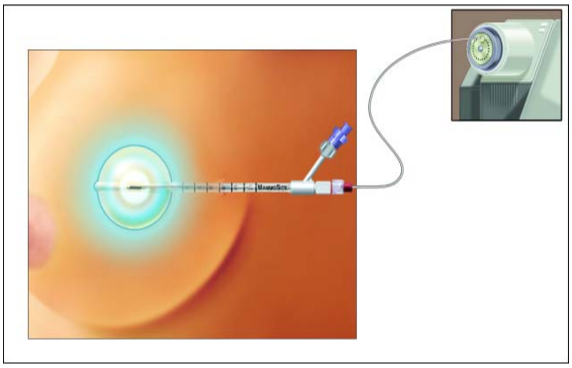

Figure 2.1. The MammoSite® Radiation Therapy System, courtesy of Hologic Corporation and affiliates.

2.1.4.1 Dosimetry of MammoSite

Limited publications have evaluated the dosimetry achieved with the MammoSite technique [10, 14-17]. Edmundson et al. (2002) reported the first study on the dosimetry of the MammoSite breast brachytherapy device [10]. Eight patients were treated. A computed tomography scan of each patient was used to determine the treatment parameters, namely the balloon radius, balloon symmetry, the Planning Target Volume (PTV) and the distance from the balloon surface to the skin. These parameters were verified using functions available in a three–Dimensional (3D) treatment planning system (Pinnacle[3], ADAC Laboratories, Milpitas, CA). The dosimetric data of the MammoSite were analysed and compared to a similar group of patients that were treated with interstitial High Dose Rate (HDR) brachytherapy using Ir-192 source. The study compared the planning target volume of the MammoSite patients to those of a similar group of patients treated with the interstitial brachytherapy technique at the same institution. The mean PTV of the MammoSite patients was 112.1 cm^3 compared with 98.3 cm^3 for interstitial brachytherapy implant patients. The MammoSite technique provided better planning target volume coverage compared to that achieved with interstitial implants. The D_{90}, which is the minimum dose to 90% of the PTV, was calculated for both the MammoSite and interstitial patients. The mean values were 90.0% and 69.8% for the MammoSite and the interstitial brachytherapy methods respectively. These results showed that the MammoSite device provided significant improvements in dose coverage. However, the study also indicated that MammoSite device with the balloon radius larger than 3.0 cm would result in longer treatment times and would give rise to higher doses to the normal structures, such as the heart and the lungs. As a result, there should be an upper limit on the size of the cavity that can be treated with the MammoSite balloon.

Dickler et al. (2004) presented results regarding the volume of the breast tissue treated with the MammoSite applicator [14]. The study included 21 patients with early stage breast cancer. The volume of the treated breast tissue was constructed on the basis of scans of the lumpectomy cavity of each patient both with and without the inflated balloon. The study found that the volume of breast tissue treated by the MammoSite device was equal to the volume encompassed by a margin of 1.6 cm around the empty lumpectomy cavity. This is comparable with interstitial high dose rate brachytherapy technique which treats a 1-2 cm tissues margin around the lumpectomy cavity.

The previous publications have evaluated the dosimetry achieved with the MammoSite device alone. It was Weed et al. (2005) who reported the first single-institutional dosimetric comparison of patients treated with three forms of accelerated partial breast irradiation techniques: Interstitial High Dose Rate Brachtherapy (IB), the MammoSite HDR Brachytherapy (MB) and 3D Conformal Radiation Therapy (3D-CRT) [17]. The 3D-CRT plans were performed using 3D planning system, Pinnacle^3 6.0. For the MammoSite and interstitial brachytherapy patients, the plans were generated using the HDR Plato Nucletron Planning System. Dose Volume Histograms (DVHs) were used to evaluate the dose coverage of the PTV and the normal structures including the ipsilateral breast, ipsilateral lung, and heart for all patients. A summary of patient information is shown in Table 2.1. Coverage of the PTV varied according to the technique used and the margin drawn around the lumpectomy cavity. The average PTV volume for the 3D-CRT patients was twice larger than the average PTV for the MB patients and slightly larger than the average PTV for the IB patients at 237 cm^3, 107 cm^3 and 192 cm^3, respectively. The average ipsilateral breast volume was at 1568, cm^3 1628 cm^3 and 1920 cm^3 for the 3D-CRT, MB and IB patients, respectively. The average ipsilateral lung volume was similar in all patient groups. It was at 1116 cm^3, 1355 cm^3 and 1404 cm^3 for the IB, 3D-CRT and MB patients, respectively. The average heart volume was 563 cm^3, 586 cm^3 and 584 cm^3 for the IB, MB and 3D-CRT patients, respectively.

Table 2.1. Patient characteristics including total dose, volume of lumpectomy cavity, volume of ipsilateral breast, volume of ipsilateral lung and heart volume.

Variables	IB	MB	3D-CRT
Number of patients	10	10	10
Total dose (cGy)	3200	3400	3850
Average lumpectomy cavity (cm^3)	38	53	24
Range (cm^3)	5-101	37-70	8-44
Average PTV volume (cm^3)	192	107	237
Range (cm^3)	97-357	83-125	104-380
PTV expansion (cm^3)	1.5	1	1 + CTV (1.5)
Average breast volume (cm^3)	1920	1628	1568
Range (cm^3)	1059-2654	1147-2729	633-2569
Average lung volume (cm^3)	1116	1404	1355
Average heart volume (cm^3)	563	568	584

The results indicated that the 3D-CRT method offered the best PTV coverage of the three treatment techniques. The percentage of the PTV receiving 100% of the prescribed dose was 58% in the IB method compared with 76% and 94% with the MB and 3D-CRT techniques respectively. The percentage of the PTV receiving 90% of the prescribed dose was 68%, 91% and 100% for the IB, the MB and 3D-CRT techniques respectively. It must be mentioned that the three cohorts were very dissimilar and hence the dosimetric comparisons are unwarranted. In addition, the IB coverage of the PTV was well below the normal coverage of 97%.

Furthermore, the results showed that both brachytherapy techniques delivered significantly less dose to the normal breast tissue as compared with the 3D-CRT. For example, the percentage volume of the ipsilateral breast receiving 100% of the prescribed dose was 5%, 10% and 24% for the MB, IB and 3D-CRT patients, respectively. However, both brachytherapy methods treated higher portion of the breast volume above 115% of the prescribed dose compared with the 3D-CRT. For example, the MammoSite and interstitial brachytherapy techniques treated 4% and 5% of the breast volume to 115% of the prescribed dose, respectively while 0% of the breast volume received 115% of the prescribed dose with the three-dimensional conformal radiotherapy technique.

The results have also shown that each of the three techniques has contributed to a limited dose to normal structures namely the ipsilateral lung and heart. The average volume of the ipsilateral lung receiving 10% and 20% of the prescribed dose was 9% and 5% for 3D-CRT compared with 3% and 0% for IB and 4% and 0% for the MB patients. The average volume of the heart receiving 10% of the prescribed dose was 1% for each of the three techniques.

The study concluded that the MammoSite device consistently provided better dose coverage of the PTV as compared to the interstitial brachytherapy. But the three-dimensional conformal radiotherapy offered better coverage of the PTV in comparison to either of the brachytherapy techniques. However, this resulted in a higher dose to the normal breast tissues and lung. The study highlighted that the optimal partial breast irradiation technique is a clinical decision. The shortcoming of the study is that it does not compare dosimetry in identical patient datasets. The patients representing the three different treatment groups were different which can make the dosimetric comparison less straightforward.

Khan et al. (2006) presented results of dosimetric comparison of three different methods of Partial Breast Irradiation (PBI): The MammoSite Brachytherapy, 3D Conformal Radiotherapy and Intensity Modulated Radiation Therapy (IMRT) [15]. The study consisted of 15 patients with early stage breast cancer who underwent breast conserving therapy. With the use of CT images, plans were developed for each patient using each of the three methods. The study compared the plans by specifying the following dosimetric parameters: the volume of planning target volume (V_{PTV}), the percent of PTV that received 90% (V_{90}) and 100% (V_{100}) of the prescription dose, the percent of the ipsilateral normal breast that received 50% (V_{50}) of the prescription dose, the percent of the contralateral breast that received 3% (V_3) of the prescription dose, the percent of the ipsilateral lung that received 30% (V_{30}) of the prescription dose. In addition, the dose to the heart V_5 (percent of the heart that received 5% of the prescription dose) was determined for patients who had left-sided breast tumours.

The results of the study are summarized in Table 2.2. The volume of the PTV was smaller in MB plans than in 3D-CRT and IMRT plans. This can be attributed to the 2.5 cm margin which was used around the lumpectomy cavity to generate the PTV for both 3D-CRT and IMRT methods. All three groups had low volume of the lung receiving 30% of the prescribed dose, but the IMRT patients had the lowest value. An interesting result from the study is that the MB technique resulted in significantly higher dose to the heart (V_5) as compared to both 3D-CRT and IMRT method for the 10 patients with left-sided tumours. This is because, as opposed to MammoSite brachytherapy treatment planning, the heart is contoured as an organ risk in both 3D-CRT and IMRT plans and the dose delivered can thus be constrained and optimized. The study highlighted that both 3D-CRT and IMRT methods have the advantage of not requiring a placement of foreign object inside the patient. However, the difficulty of identifying the cavity in certain patients, respiratory motion and patient setup are of the main concerns when using 3D-CRT and IMRT techniques. On the other hand, these issues are not significant with the use of the MammoSite device. The study concluded that the choice of optimal PBI method is complex and requires both doctor decision and suitable patient selection.

Table 2.2. Summary of dosimetric comparison.

Variables	MB	3DCRT	IMRT
PTV volume (cm^3)	94.3	184.3	184.3
V_{110} (%)	84.2	0.99	0.8
V_{100} (%)	94.9	92.3	93.7
V_{95} (%)	97.9	99.9	99.9
V_{90} (%)	99.3	99.9	100.0
Ipsilateral breast V_{50} (%)	29.2	55.8	46.2
Ipsilateral lung V_{30} (%)	5.4	6.7	1.9
Heart V_5 (%)	11.6	4.1	1.2

Major et al. (2006) reported a dosimetric comparison between treatment plans of Interstitial Brachytherapy and MammoSite Brachytherapy patients with early stage breast cancer [16]. The study included seventeen patients that were treated with IB and twenty-four that were treated with MB. The plans for all patients were based on CT images, and the dose distributions were evaluated using DVH. The evaluation of the dose distributions were carried out by calculating and comparing the following parameters: the volume of the planning target volume (V_{PTV}), the V_{PTV} in percent that receives 90%, 100%, 150% and 200% of the prescribed dose ($V_{90\%}$, $V_{100\%}$, $V_{150\%}$, $V_{200\%}$), the percentage of the dose that covers 90% of the PTV ($D_{90\%}$), the percentage minimum dose in the PTV ($D_{min\%}$), the maximum point dose to both the lung ($D_{lung\%}$) and the heart ($D_{heart\%}$). The average volume and dose parameters for interstitial brachytherapy (IB) and MammoSite brachytherapy (MB) techniques are listed in Table 2.3.

Table 2.3. Average volume and dose parameters for interstitial and MammoSite brachytherapy patients.

Variables	MB	IB
V_{PTV} (cm^3)	109.6	63.4
$V_{90\%}$	96	92
$V_{100\%}$	88	87
$V_{150\%}$	27	55
$V_{200\%}$	3	32
$D_{90\%}$	99	94
$D_{min\%}$	67	58
$D_{lung\%}$	66	55
$D_{heart\%}$	27	29

It can be seen from the above table that the average volume of PTV was higher for MB than IB patients at 109.6 cm^3 and 63.4 cm^3, respectively. The small volume of the PTV for interstitial brachytherapy patients is because of the safety margin of 1.0 cm that was used around the lumpectomy cavity. The study reported that the $V_{150\%}$ was 55% for the IB. This value was much higher the accepted practice which would limit the $V_{150\%}$ to less than 25% of the PTV. The results also showed that the volume of the PTV receiving twice the prescribed dose ($V_{200\%}$) was less for the MB patients. The dose distribution was much more conformal in MammoSite device than the interstitial implants. However, it should be mentioned that the shapes of the PTV were very different in the IBT and MBT groups. In interstitial brachytherapy individual safety margin can be used in different directions, while in MammoSite brachytherapy a uniform margin of 1.0 cm from the balloon surface is used. The doses to the heart were not significantly different between the two groups. However, the Maximum point dose to the lung was higher in MammoSite plans compared to interstitial plans. Overall, the study pointed out the MammoSite brachytherapy device has produced acceptable dosimetry, but longer follow-up time was recommended to evaluate its clinical efficacy.

2.1.4.2 MammoSite and cosmetic outcomes

The two important factors for achieving treatment effectiveness and optimal cosmetic results are balloon cavity conformance and skin-to-balloon surface distance. The former is essential in order to achieve good dose homogeneity within the PTV. The latter is for restraining the maximum skin dose. A minimum distance of 5 mm was chosen to keep the skin dose less than 150% of the prescribed dose [10, 18]. However, recent publications have reported that a balloon-to-skin distance of larger than 7 mm is recommended to optimize the probability of excellent cosmetic results [19, 20]. The clinical results of recent publications using the MammoSite technique as sole radiation treatment following lumpectomy are summarized in Table 2.4. For example, Dragun et al.(2007) reported excellent cosmetic results in 68.9%, good in 21.1%, fair in 8.9% and poor in 1.1% of 100 patients treated with the MammoSite device at a median fellow up of 2 years [19]. No breast tumour recurrence was reported. Overall, the excellent cosmetic results were associated with a balloon to skin distance larger than 7 mm.

Jeruss et al. (2006) reported clinical results of 169 patients who had breast cancer treatment with the MammoSite balloon device [21]. The follow up data was available for 158 patients. The average length of the follow up was more than seven months. Patients with balloon to skin distance greater than or equal to 7 mm had the best cosmetic results and lower skin damage [21]. These findings were confirmed using data on forty three patients who had a follow up period of at least one year. No patient in the study has experienced the recurrence of the breast cancer.

Table 2.4. Clinical results of cosmetic outcomes and tumour recurrence using the MB.

Reference #	# of patiens	Average follow-up (months)	Good/ excellent cosmetic results (%)	Skin distance (mm)	Skin dose/ fraction (cGy)	Tumour recurrence (%)
[19]	100	24	21-69	7-8		0
[22]	43	21	88	> 7		0
[23]	43	29	84	> 7		0
[24]	28	19	93	≥ 5		0
[25]	30	13	93	7-15	354-422	0
[26]	40	13	97	> 7		0
[27]	30	7	20-73	4-14	130-558	0
[28]	248	12	92	≥ 7		0.1
[29]	100	9.5	98	7-13		2
[21]	158	12	88	> 7		0
[30]	67	13	96	7-15	56-488	0

2.1.4.3 Long term follow-up data

There have been very few published data regarding the long term tumour control and cosmesis associated with the MammoSite brachytherapy. Chao et al. (2007) presented the results of eighty patients treated with the MammoSite applicator [31]. The study reported that 88.2% of patients were found to have good/excellent cosmetic results at 3-year follow-up. Ipsilateral breast-tumour recurrence occurred in two patients (2.5%) their ages were 41 and 51 years. Both recurrences occurred within 12 months after completion of the MammoSite treatment. The 3-year disease-free survival rate for all patients was 95.8%. At 24 months follow-up, the increased balloon-to-skin spacing ≥ 7 mm was associated with high occurrence of good-excellent cosmetic results. These observations highlight the importance of the distance from the balloon surface to skin to avoid large excessive dose to the skin. The study concluded that the 3-year follow-up results had demonstrated that the MammoSite treatment outcomes were similar to those observed with interstitial brachytherapy method at the same follow-up length.

Chen et al. (2007) reported 7.1% of treatment failures among 70 patients treated with the MammoSite technique at a median follow-up time of 26.1 months [32]. The tumour recurrence for one case was directly adjacent to surgical bed and three cases were at more than 2 cm away from the original surgical bed. Benitez et al. (2007) presented the results of

5.5-year follow-up of thirty–six patients treated with the MammoSite brachytherapy [33]. The cosmetic outcomes were good /excellent in 83.3% of the followed patients. The study observed no local recurrences at either the tumour bed or elsewhere in the breast for all 36 patients. The study concluded that the 5-year local recurrence using the MammoSite balloon in carefully selected patients were comparable to the 5-yaer data achieved with external beam irradiation and interstitial brachytherapy techniques.

The available 3-5 year results can serve as an indicator of the adequacy of the MammoSite treatment method in terms of tumour control in comparison with other accelerated partial breast irradiation techniques. However, further data is needed to document the long term efficacy of the MammoSite treatment modality.

2.1.4.4 MammoSite treatment complications

Limited information is available in the literature regarding the toxicities associated with the MammoSite treatment method. Richards et al. (2004) reported the acute toxicities of patients treated with the MammoSite device as the sole method of radiotherapy [34]. The median follow up was 11 months. No acute toxicities were reported during the 5 days of treatment. 25% of the patients developed bright erythema and patchy moist desquamation. 7% developed confluent moist desquamation within the first 4 weeks but healed by week 12. 16% of the treated patients developed infections.

Harper et al. (2005) assessed the acute complications of 37 patients on the day of the treatment completion and four weeks after the course of the treatment [27]. 93.3% of the patients were happy with the MammoSite therapy. 5.4% (2 patients) experienced Grade 2 toxicity. 2.7% (1 patient) experienced Grade 3 toxicity. 16.2% (6 patients) developed wound infections. 32.4% (12 patients) developed seromas.

Sadeghi et al. (2006) examined the dose delivered to the skin and the surrounding tissues around the MammoSite brachytherapy technique in 67 patients [30]. The study reported that 56% of the patients experienced no skin reaction at a median follow up of 13 months. 35% developed erythema but it disappeared over several weeks. 4 (6%) patients had dry desquamation and 2 (3%) patients experienced moist desquamation, and received skin dose greater than 4.10 Gy per fraction.

Agawal et al. (2005) assessed acute toxicities in 100 patients who were treated with the MammoSite brachytherapy device ([35]. Persistent seroma was observed in 26% of the patients with a follow up of 6 months. The study concluded that the development of seroma may be attributed to the delivery of high radiation doses to the surgical cavity margin. Evans et al. (2006) reported the risk of development of seroma in 38 patients after the use of MammoSite technique for accelerated partial breast irradiation [36]. Persistent seroma was seen in 68.4% of the patients with a follow up of more than 6 months. Of the patients with persistent seroma, 46% experienced some pain in the breast during the follow up period. However, only 19.2% of those patients had these symptoms persist at their last follow up (median of 15.8 months) examination. Overall, the results of the studies of the acute complications associated with the MammoSite method are encouraging but these observations need to be validated with more published clinical data.

2.1.4.5 Uncertainties in MammoSite brachytherapy

There are several uncertainties associated with the dose distribution from the MammoSite brachytherapy (MB). They include the concentration of the contrast medium inside the balloon, source positioning, and balloon deformation. These parameters need to be thoroughly investigated as they represent significant impact on the treatment efficacy.

Once the MammoSite balloon is placed into the cavity, it is inflated to a size that would fill the surgical cavity using saline and an amount of radiographic contrast. A computed tomography scans are obtained and the treatment plan is developed. At present, the commercially available brachytherapy treatment planning systems (e.g., Plato, Nucletron) perform dosimetry calculations according to the recommendations of the AAPM TG-43 protocol [37]. The dosimetry is based the assumption that the high dose rate brachytherapy source is located in water medium. Because the contrast medium contains elements with high atomic number (iodine with Z=53), the balloon is no longer equivalent to tissue or water. Thus, the treatment planning system does not accurately predict the effect of radiographic contrast medium inside balloon on the prescribed dose.

The MammoSite brachytherapy, as with any other radiotherapy technique, aims at delivering the prescribed dose to the treated volume while simultaneously avoiding complications to the adjacent normal tissues. Accurate source positioning at the balloon centre as well as minimal balloon deformation are important for desired dose delivery with the MammoSite applicator. Uncertainties in source position and a small or large deformation of the balloon shape (elliptical shape) may perturb the prescribed dose to the treated volume. For example, some regions of the planning target volume (PTV) can receive less than the prescribed dose. This could lead to a greater risk of tumour recurrence. Portions of the PTV will also receive more than the prescribed dose. This in turn may result in the exposure of critical organs (heart, lung and skin) to extra dose. Hence, it is useful to use the biological models to predict the effect of these particular uncertainties on the MammoSite treatment outcomes.

2.1.5 Combining MB and EBRT

For some patients, different radiation treatment modalities can be combined to prevent the risk of the probability of tumour recurrence. At our institution, patients with early stage breast cancer were treated with the combination of MammoSite brachytherapy and external beam radiotherapy. No studies have been undertaken to combine the dose distributions from both modalities. In this work, a technique is developed to combine the dose distribution from MammoSite brachytherapy and external beam radiotherapy techniques.

2.1.6 Conclusions

Previous investigators have demonstrated that device insertion into the patient and performance are easy and efficient. Coverage of the PTV varied according to the technique used and the definition of adequate coverage used. However, the presented studies show that the MB device produced better coverage of the PTV compared to IB implants. The coverage of the PTV was better with 3D-CRT, resulting however in a higher dose to normal breast tissue than the MammoSite brachytherapy technique.

It appears that two factors may limit the use of MammoSite brachytherapy device. The conformance of the balloon to the cavity is essential to assure appropriate dosimetry. Additionally, the distance between balloon and the skin has been reported to be the most important factor for achieving optimal cosmetic results. Cosmetic results were good-to-excellent in most of the patients with balloon-skin spacing of larger than or equal to 7 mm.

The endpoint of the MammoSite treatment technique as with any other radiotherapy modality is to achieve high tumour control probability and minimal normal tissue complications. Existing clinical findings have demonstrated highly acceptable outcomes with the MammoSite breast brachytherapy device regarding tumour control, acute complications and cosmetic results. The data coming from the presented clinical trials with an average follow up of 16 months have neither reported tumour recurrence nor normal tissue complications among the treated patients. The currently available long term data on the MB tumour control were comparable with other APBI techniques.

Part two: Monte Carlo technique

2.2.1 Introduction

In radiation dosimetry, Monte Carlo techniques simulate the radiation transport in a medium of any composition and state. In the past, Monte Carlo method had a limited application in radiotherapy due to its high demands for computing power. However, nowadays computing power is advancing and the Monte Carlo method is slowly making its way into radiation treatment planning systems. Monte Carlo simulation of radiation transport is generally considered to be the most accurate method for the calculation of dose distributions in radiation therapy [38, 39]. There are different Monte Carlo systems used for dose calculation in radiotherapy; they include EGSnrc [40, 41], MCNP [42, 43], PENELOPE [44], GEANT4 [45] and others. EGSnrc and PENELOPE simulate the coupled transport of photons and electrons, while MCNP and GEANT can also take into account other particles such as protons and neutrons. Generally, photon transport modelling is quite similar in all four systems, although different cross section data is used. All of these codes are written in the FORTRAN programming language, except GEANT4, which is written in C++.

This chapter presents the fundamentals to understanding the mechanism of the Monte Carlo method. It also describes the EGSnrc Monte Carlo code system. Furthermore, the chapter discusses the applications of Monte Carlo in the modelling of HDR brachytherapy sources and linear accelerators.

2.2.2 What is Monte Carlo?

The Monte Carlo method represents an attempt to model real processes through direct simulation of the essential dynamics of the system in question [46]. In this sense, the

Monte Carlo method is a solution to a macroscopic system through simulation of its microscopic interactions. A solution is determined by randomly sampling the microscopic interactions of the system until the result is obtained. Thus, the mechanism of executing a solution involves repetitive action or calculation. The fact that many microscopic interactions can be modelled mathematically makes it possible for the repetitive solution to be executed on a computer, using specific algorithms [46].

Monte Carlo techniques are used in a wide range of scientific applications. In case of radiation transport, they simulate the transport of ionizing radiation such as photons, electrons, protons and neutrons in any medium of any composition and state. Monte Carlo program, applied in the simulation of radiation transport, uses machine generated random numbers and the knowledge of the probability distributions governing the individual interactions of electrons and photons in matter to simulate the trajectory of individual particles [39]. The trajectory of the incident particle, and the other particles being created along its path, is referred to as particle history. As a large number of histories are simulated, results can be obtained about the average values of quantities of interest such as absorbed dose and energy fluence in a region of interest. However, a large number of histories are required to obtain a small uncertainty in the result.

In contrast to Monte Carlo methods, analytical methods for calculation of radiation transport within a medium are mathematically very complex and solutions require many approximations [47]. Furthermore, analytical solutions give only the final state of the particle with no information about its passage through the medium.

Figure 2.2 is an example of a shower of particles produced in a Monte Carlo simulation. An incident photon undergoes a Compton interaction with an electron at point A and the resultant scattered electron leaves the volume of interest. The scattered photon then sets off a pair production event at point B and the resultant positron annihilates with an electron at point C to produce two annihilation photons. All particles generated during this shower are tracked until their energy fall below a specified cut-off or until they leave the volume of interest.

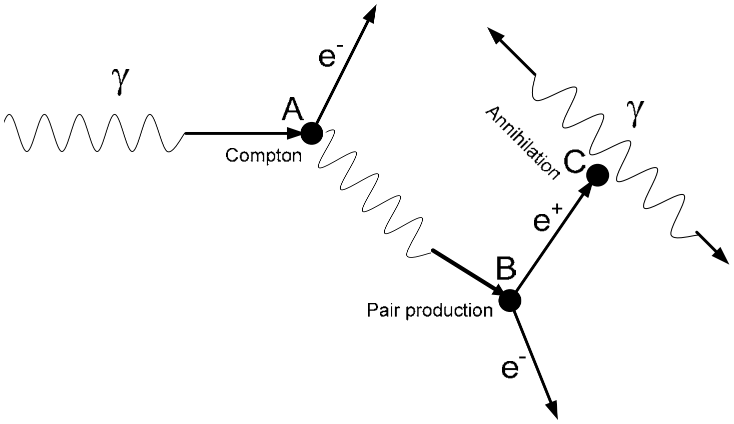

Figure 2.2. Schematic diagram illustrating a shower of particles simulated by Monte Carlo for radiation transport.

A Monte Carlo simulation code has four major components: (1) the cross-section data for all the process being considered in the simulation, (2) the algorithms used for particle transport which describe the interaction process, (3) specification of the geometry in which the particles being transported and (4) a method for analysing the quantities of interest obtained during the simulation.

2.2.3 Physics of Monte Carlo simulation process

The physics of electron and photon interactions in matter is known, but in general there is no analytical expression to describe particle transport within a medium. This is because the macroscopic distribution of the particles generally depends on the heterogeneity and medium geometry including the source as well as the nature of particle interactions. This renders the analytical solution only applicable to simple cases. In the following two sections, Monte Carlo simulation of the transport of photons and electrons through matter is briefly described.

2.2.3.1 Photon transport

Figure 2.3 presents the steps for a Monte Carlo simulation of photon transport. The process starts by initially placing the photon parameters on the stack. The stack is an array containing parameters of the particles awaiting transport including the energy, position and direction. A photon entering the transport routine is first tested to see if its energy is below the transport cut-off specified by the user. If it is below the cut-off, the history is then terminated. If the stack is empty then a new particle history is started. If the energy is above the cut-off then the next step is to choose the distance to the particle's next interaction. This distance is determined as follows [47, 48]:

$$x = -\frac{1}{\mu}\ln(R1) \ , \qquad (2.2.1)$$

where x is the distance, μ is the photon attenuation cross section and R1 is a random number between 0 and 1.

The photon is then transported to the point of interaction. If the photon has left the volume of interest then the history is terminated, otherwise, the next step is to sample to see which type of interaction occurs. Having done this, the energies and directions of the resulting particles can be determined. The resulting particles are put on the stack for transport. Then the whole process is repeated again until the stack is empty and all the incident particles are used.

2.2.3.2 Electron transport

Compared to a photon, an electron undergoes a large number of interactions during its history. In the Monte Carlo simulation of electron transport it is time-consuming to simulate each interaction on a step by step basis. This problem is made tractable by using the condensed history technique proposed by Berger [49], in which the path of an electron is broken into a series of straight steps for which the effects of individual interactions occurring during the step are grouped together. The condensed history technique divides the electron transport into two classes: Class I and Class II. Figure 2.4 is a schematic flowchart showing the essential differences between the different types of electron transport algorithms. EGS4 (Electron Gamma Shower 4) is a “Class II” algorithm which samples interactions discretely and correlates the energy loss to secondary particles with an equal loss of the energy of the primary electron.

The electron transport routine picks up the electron's initial parameters (energy, position, direction and geometry) and asks if the energy of this particle is less than the transport cutoff energy. If it is, the electron is discarded, otherwise the electron is transported and the distance the particle's next interaction is determined exactly as in the photon case. The multiple scattering step size is then selected and the particle is transported. After the transport, the scattering angle is determined and the electron's direction is adjusted. The energy loss is then calculated until the point of discrete interaction is reached. If the energy of the secondary particle, resulting from the interaction, exceeds the threshold for delta electrons or bremsstrahlung photons, then the energy and direction of the primary particle are adjusted and the process starts all over again.

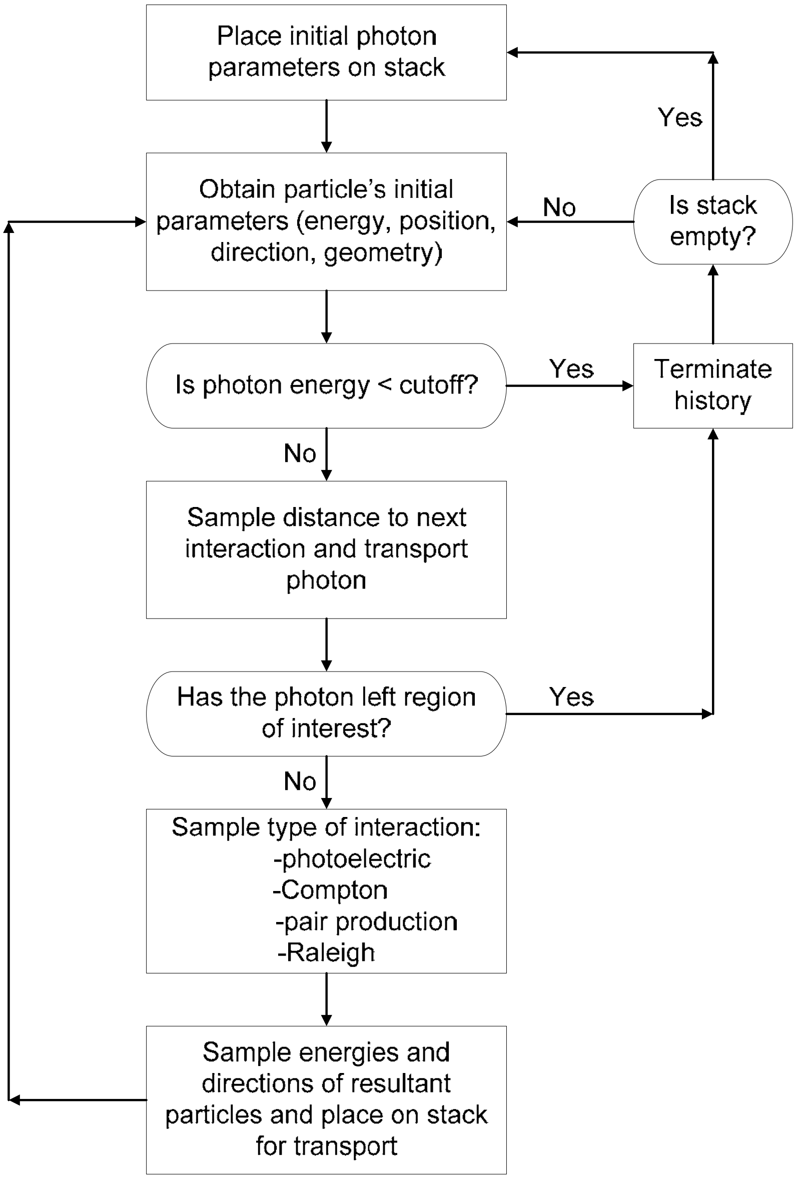

Figure 2.3. Flow chart showing steps involved in photon transport (reproduced from [47]).

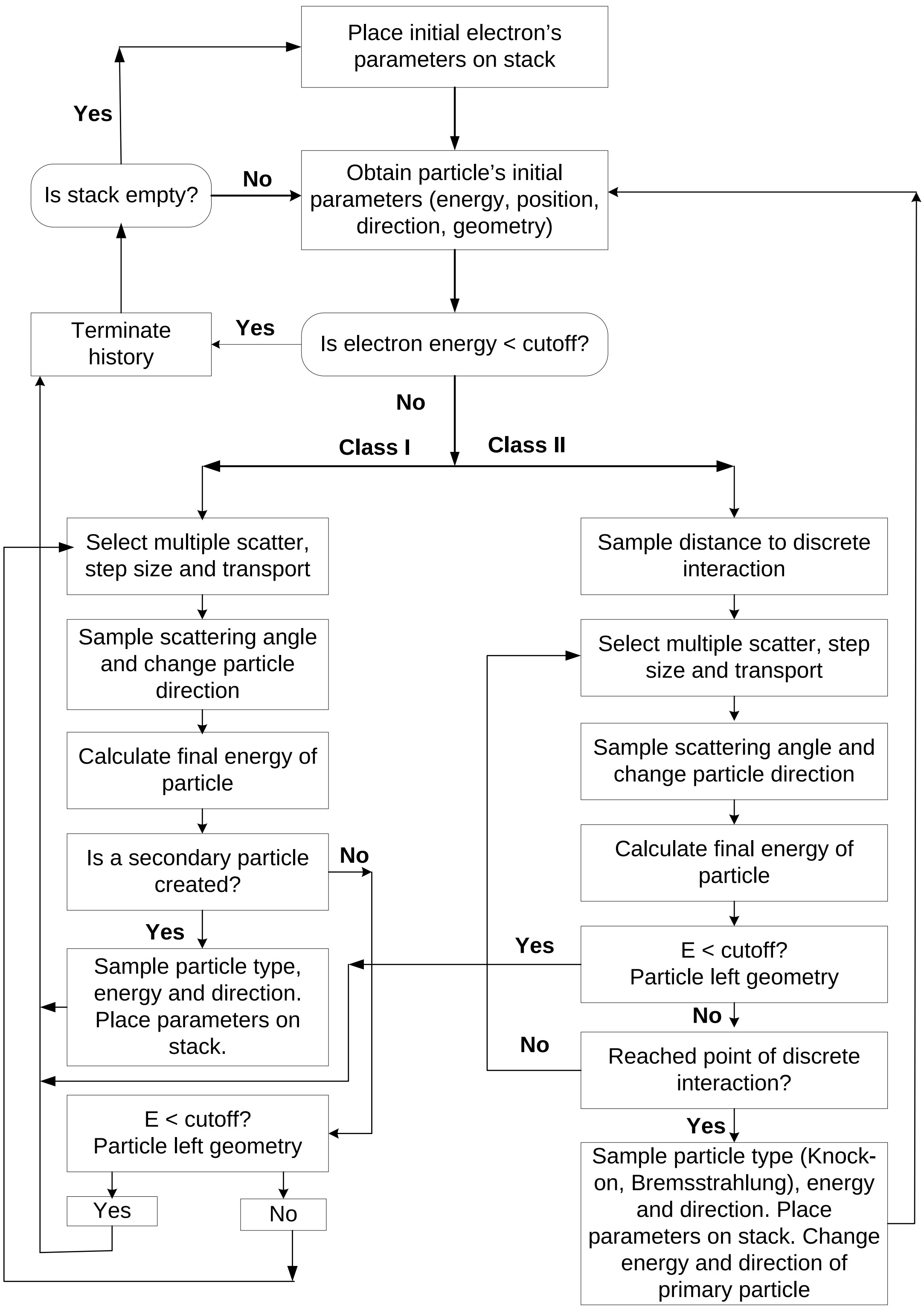

Figure 2.4. Flow chart illustrating involved in electron transport for class I and Class II Monte Carlo algorithms (reproduced from [47]).

2.2.4 EGSnrc Monte Carlo code

The EGSnrc is one of the most used Monte Carlo packages in radiation therapy. EGSnrc is a general purpose code for the Monte Carlo simulation of the coupled transport of electrons and photons for energies above a few KeV to several hundreds of GeV [40]. EGSnrc is a new version of EGS4 (Electron-Gamma-Shower 4) that has been developed by the National Research Council of Canada.

2.2.4.1 The EGSnrc user codes

The EGSnrc code includes many user codes for scoring different quantities in a specific geometry. These user codes include BEAMnrc, DOSXYZnrc, DOSRZnrc, CAVRZnrc, SPRRZnrc and FLURZnrc. The BEAMnrc user code simulates photon and electron beams produced by medical linear accelerators, x-ray tubes and cobalt-60 units. The DOSXYZnrc scores dose in rectilinear geometry. The user code DOSRZnrc scores the dose deposited in cylindrical geometry. CAVRZnrc calculates the dose to a cavity ionization chamber. SPRRZnrc calculates stopping power ratios in cylindrical geometry which are needed in primary standard and dosimetry protocols. The FLURZnrc user code is used for particle fluence and spectrum calculations in cylindrical phantoms.

2.2.4.1.1 BEAMnrc user code

In 1995 the BEAM/EGS4 Monte Carlo simulation code was released by Rogers et al [39] as part of the OMEGA (Ottawa Madison Electron Gamma Algorithm) project. The initial goal of the OMEGA project was to develop a Monte Carlo technique capable of simulating a full 3-dimensional electron treatment planning system. The rational was that analytical methods, using pencil beam algorithms, of calculating the dose in an electron beam suffered from various short comings which produced errors of 10% or more [50, 51]. Some of these problems may be removed using advanced analytic methods [52, 53], but at the expense of very considerable computational time. However, in the end, the Monte Carlo technique is capable of accurately computing the dose under almost all circumstances [47, 54]. Monte Carlo techniques are becoming widely used in radiotherapy applications because of the dramatic decrease in computing time due to improvements in computer hardware.

The BEAM user code has been designed to simulate photon and electron beams from any radiotherapy machine, including low-energy x-rays, ^{60}Co units and linear accelerators.

BEAM has now been upgraded to BEAMnrc [55]. The BEAMnrc user code allows for the construction of a user-specified accelerator head by defining its components (such as flattening filter, primary collimator, monitor chamber, mirror, and jaws) through the use of component modules (CMs) available within the code. The BEAMnrc program simulates the transport of electrons and photons starting from the stage they enter the treatment head until they exit the treatment head. The BEAMnrc user code, which is built on the EGSnrc Monte Carlo code system, produces as its output a phase-space file containing all parameters (particle types, direction, energy, *etc*.) of a large number of particles entering the linear accelerator.

Figure 2.5 presents a schematic of the overall steps required for an accelerator simulation using the BEAMnrc code. At “Specify Accelerator”, the user defines the CMs to use to model each individual part of the accelerator head. For example, the PYRAMIDS CM can be used to simulate a wedge. Once the accelerator is specified, it can then be built. The accelerator is built using the CMs which can be combined or modified to match the actual shape and composition of the real accelerator components. The dimensions, materials and positions of different accelerator components are based on the manufacturer’s specifications. The cross section tables, for the different materials that make up the component module, are stored in a PEGS4 (pre-processor for EGS4) data file. Once specified and built, the accelerator file must be compiled.

The user interacts with the BEAMnrc code through an input file. The input file contains all the parameters required for the Monte Carlo simulation. For example, the user chooses the type of incident source. If the accelerator is modelled from above the target then the incident source is an electron beam incident on the target. The BEAMnrc code has a large range of sources with varying geometrical and energy characteristics to choose from. In general, the input file includes all the parameters controlling the radiation transport modelling and the various reduction techniques (such as transport cutoff energies, range rejection, bremsstrahlung splitting and Russian roulette) to be used. The various reduction techniques will be explained in more details in chapter six. The next step is to run the simulation. The final stage of the BEAMnrc simulation is an output files which consist of phase-space, output listing and 3D graphics display files. The phase–space file is then processed using other EGSnrc user codes for analysis or dose calculation in a water phantom / patient simulation.

Figure 2.5. The steps involved in using the BEAMnrc system (adapted from [39]).

2.2.4.1.2 DOSXYZnrc user code

DOSXYZnrc is a new version of the DOSXYZ/EGS4-based user code and was made available by Kawrakow and Walters [56]. DOSXYZnrc is a Monte Carlo simulation EGSnrc-based user code for calculating dose distributions in three-dimensional phantoms. This user code simulates the transport of photons and electrons in a Cartesian volume and scores the energy deposition in the designed voxel. The DOSXYZnrc user code creates a rectangular phantom composed of user defined voxels and materials and calculates the average dose deposited in each voxels from the number of simulated particles. The shape and the size of the phantom are defined by X, Y and Z dimensions. The phantom material can either be set individually for each voxel or globally for the whole phantom. The uncertainty in the dose calculation is dependent on both the size of the voxel and of the number of histories in the simulation. The smaller the voxel size, the more particles are required to get statistically acceptable results. The number of particles is linearly proportional to the computing time.

DOSXYZnrc has a number of important and unique features such as dose component calculation, a wide variety of source configurations, CT dataset readings, phase-space redistribution, etc.

Figure 2.6 illustrates an example of the input and output data for a Monte Carlo simulation using DOSXYZnrc user code. The input file is created by the user, where different parameters are defined, such as the number, type and density of media. The cross section data for the different materials used in the EGSnrc simulation is stored in a PEGS4 (pre-processor for EGS4) file. The names of the PEGS4 cross-section data files are 700 icru and 521icru. The input file also includes phantom dimensions, number and size of the voxels as well as source geometry, the spectrum of the source and the number of particles to be simulated. In addition, the Monte Carlo transport parameters, such as global electron and photon cutoff energies and electron and photon transport algorithms are defined in the input file.

Once the input file is compiled, it is then executed to run the simulation. The execution stage requires the name of the input file (*.egsinp) and the PEGS4 cross section data file (700icru or 500icru). DOSXYZnrc simulation outputs different files, for example it produces *.3ddose file which contains a summary of the data in all regions and can be used by the STATDOSE [57] program to extract dose distribution profiles. The DOSXYZnrc simulation also outputs a listing file containing all information regarding the dimensions of the phantom, position of the source within the phantom (in case of brachytherapy applications) and energy bins read from the source spectrum. Furthermore, dose distribution results can be viewed graphically using the software DOSXYZ_SHOW [58] available with the EGSnrc system package. The visualization requires 3-D dose distribution (*.3ddose) file as well as the file containing the phantom material and geometry (*.egsphant). The other files generated by the DOSXYZnrc simulation include *.egserrors and *.egsdat.

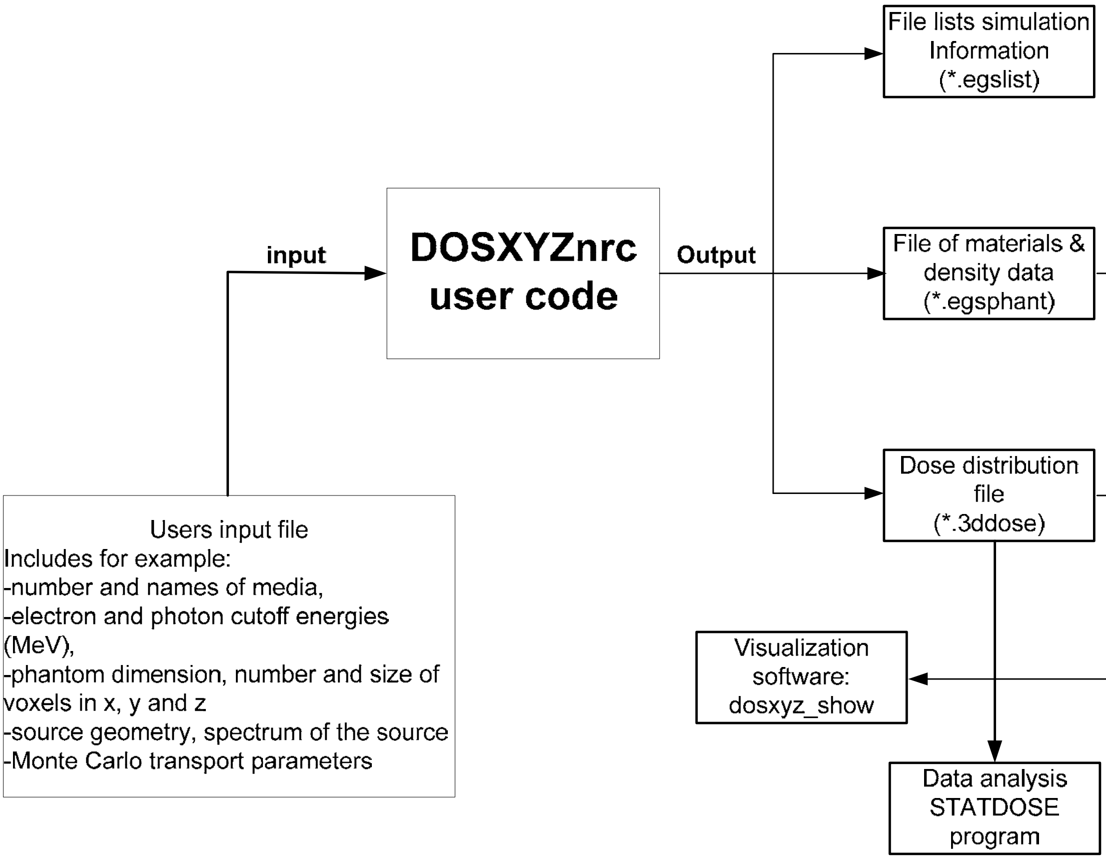

Figure 2.6. A schematic flowchart illustrating the steps for DOSXYZnrc simulation.

An important advantage of the DOSXYZnrc user code over the other EGSnrc Monte Carlo dose calculation user codes is that it is capable of carrying out the simulation using CT datasets. CT phantoms can be modelled in DOSXYZnrc by processing the CT data using the CTCREATE [56] program, available with the EGSnrc system package. This allows the simulation of dose distributions in phantoms derived from patient CT datasets.

Figure 2.7 is a flowchart for use of CT data with a DOSXYZnrc simulation. The CT data files are first transferred to the EGSnrc code and placed in the directory of CTCREATE user code. A user input file is created; it contains several records or parameters such as the name of the header file of the CT dataset. The code will read in all information that it requires from the header file before moving on to read in the entire binary data file (.img). Other records in the input file include CT volume in (X,Y,Z), voxel size, number of materials within the phantom, CT number and the lower and upper density of the material. The final step is to compile the input file; this will generate a CT phantom file (has an extension *.egsphant) which is readable by DOSXYZnrc.

In short, the input file for DOSXYZnrc simulation is different if the CT option is used. Some of the records in the DOSXYZnrc input file are no longer needed since the created

CT phantom contains the information of those records. However, the output of DOSXYZnrc simulation is similar to that shown in Figure 2.2.5.

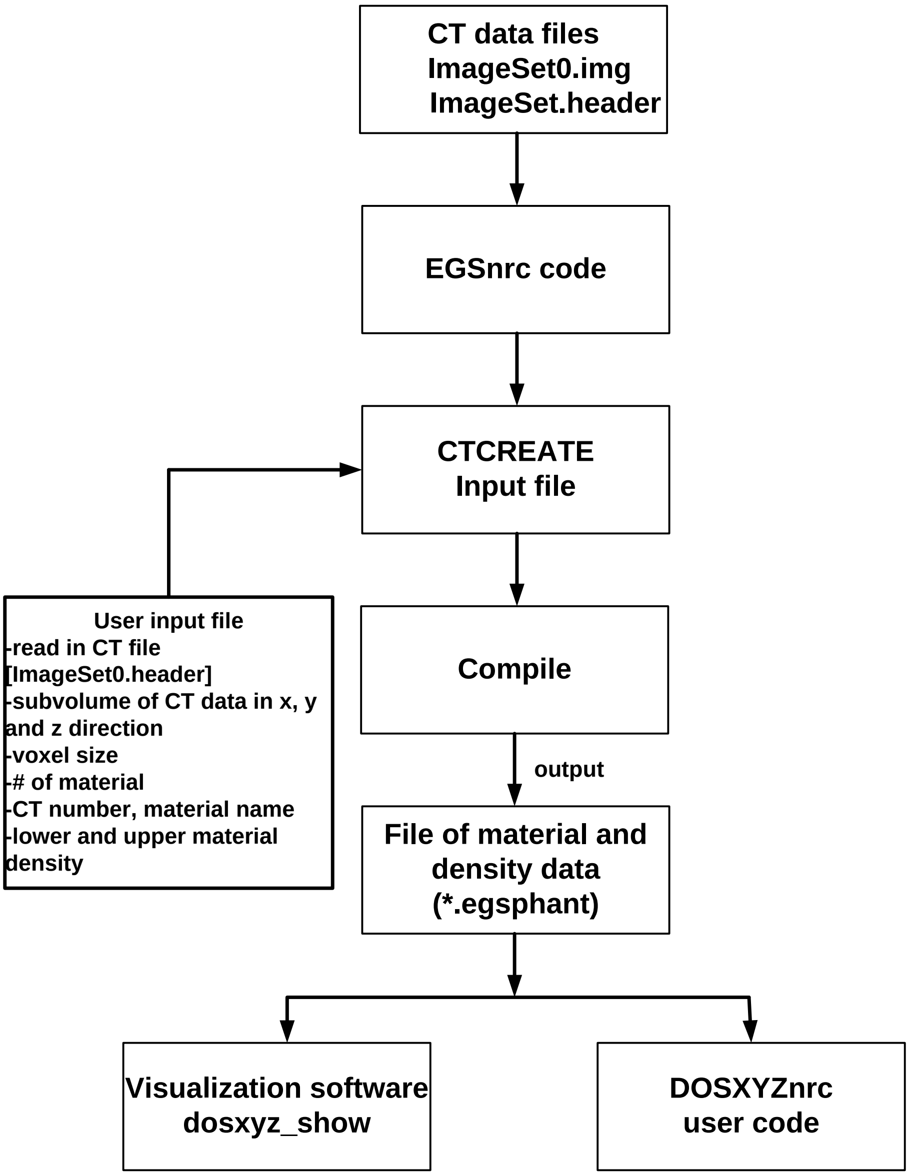

Figure 2.7. A flowchart for use of CT data with DOSXYZnrc.

2.2.5 Modelling of ^{192}Ir HDR brachytherapy source

High-dose-rate (HDR) brachytherapy is used for many types of cancers. ^{192}Ir is a commonly used source in HDR brachytherapy and the source is widely available commercially. The microSelectron remote afterloading HDR brachytherapy (Nucletron International, Veenendaal, The Netherlands) unit and its Plato brachytherapy treatment planning system are popular in brachytherapy applications. The microSelectron HDR unit is a brachytherapy device in which a high activity γ-ray source (^{192}Ir) is driven by a remote afterloader device inside a catheter to predefined positions within the patient. The dose calculation formalism used by most of the Plato brachytherapy planning system is based on the AAPM TG-43 algorithm [37]. The dose rate, $\dot{D}(r,\theta)$, at a point with coordinates (r,θ) from the centre of a source is calculated in the TG-43 model by

$$\dot{D}(r,\theta) = \Lambda S_k \frac{G(r,\theta)}{G(r_0,\theta_0)} F(r,\theta) g(r) \tag{2.2.2}$$

Where S_k is the air kerma strength (defined in units of cGy cm^2 h^{-1} or U), Λ is the dose rate constant (expressed in units of cGy h^{-1}U^{-1} or cm^{-2}), $G(r,\theta)$ is the geometry factor (defined in units of cm^{-2}), $G(r_0,\theta_0)$ is the reference point near the source where the source is normalized to unity, $F(r,\theta)$ is the anisotropy function (dimensionless) and $g(r)$ is the radial dose function (dimensionless). This formula is the basic equation of the AAPM TG 43 protocol. It considers the cylindrical symmetry of the source. Each factor or function used by the AAPM TG 43 protocol must be determined through dose measurements in a water equivalent phantom, except the geometry factor and the air kerma strength. The geometry factor is determined through arithmetic calculations and the air kerma strength is measured with an ionization chamber.

Williamson *et al* [59] used Monte Carlo photon-transport code (MCPT) to calculate complete two dimensional dose distributions from the microSelectron HDR source in water medium. The study provided relative and absolute dose-rate distributions at distances ranging from 0.25 to 5 cm at 35 polar angles. The study presented all dosimetric constants and functions for the microselectron HDR ^{192}Ir source, derived from Monte Carlo photon-transport calculations, in tabular form. The study highlighted the advantages of using Monte Carlo as a dosimetry tool in clinical brachytherapy. Unlike brachytherapy dose measurements, Monte Carlo is free from detector artefacts, such as sensitivity to positional error, volume averaging, energy dependence, and poor reproducibility of detector readings at large distances. However, the validity of Monte Carlo results depends highly on the accuracy of input data and parameters of the incident radiation beam. Also, in some cases, when modification of the Monte Carlo coded is required, an experienced user is needed to perform the simulation. In addition, a long simulation time is required to obtain results which can be compared with measurements.

Valicenti *et al* [60] measured both the transverse axis and two-dimensional polar dose profiles for an ^{192}Ir source with thermoluminescent dosimetry in a solid water phantom. The measured dose rates were normalized to measured air-Kerma strength. The study also used the Monte Carlo photon transport (MCPT) code to model the experimental phantom, source geometry and detector geometry. They found an agreement between Monte Carlo absolute dose rate calculations and measurements within 3%. This demonstrated that Monte Carlo simulation is an accurate and powerful tool for two-dimensional dosimetric characterization of high activity ^{192}Ir sources.

Borg *et al* [61] employed the EGS4 Monte Carlo code to calculate the photon spectra in both air and vacuum around four types of ^{192}Ir HDR sources, including the microSelectron HDR source. The air-Kerma strengths per unit activity were calculated based on the photon fluence around the HDR source using published mass energy-absorption coefficients. Furthermore, the study investigated the effect of bin size for scoring fluence. The contribution of low-energy photons to the air-Kerma strength was also studied for the encapsulated sources (the microSelectron HDR sources). It was found that a bin size of 5 keV was adequate for scoring fluence. The study also reported that eliminating photons with energy less than 60 keV decreases the air-Kerma strength by 0.2-0.3% and eliminating the photons with energy less than 130 keV results in air-Kerma strength being reduced by 1%. The major outcome of the study was that it provided reliable photon spectra data for different types of ^{192}Ir HDR sources.

Angelopoulos *et al* [62] used the Monte Carlo Particle Transport (MCPT) simulation code to derive all necessary dosimetric data for the Varian ^{192}Ir HDR source, following the formalism introduced by AAPM TG-43 [37]. The dosimetric data included dose rate constant, radial dose functions, geometry factors and dose anisotropy functions. The data were in agreement with similar studies [59].

Toye *et al* [63] provided complete dose distributions around a ^{192}Ir HDR source in water medium using the EGSnrc Monte Carlo code. The dose distribution was calculated using the DOSRZnrc user code which computes the dose in cylindrical geometry. The HDR source was modelled using the uniform isotropically radiating disk routine available with the DOSRZnrc user code. The total statistical uncertainty of the Monte Carlo simulation was 2.2%. Doses around the Nucletron ^{192}Ir HDR source were also measured for a range of radial distances from 5 to 30 mm within a 40 x 40 x 30 cm^3 water phantom, using a

MOSFET dosimetry system. In general, the measured dose at each radial distance from 5 mm to 30 mm was within 2-3% agreement with the EGSnrc simulations.

Papagiannis *et al* [64] employed Monte Carlo simulation to investigate differences in the dose rate distributions of the most commonly used ^{192}Ir sources in the centimetre as well as the millimetre distance range in water medium. The source designs including the old and new microSelectron, the old and new VariSource, the Buchler, the Best Medical ^{192}Ir seed and the AngioRad^{TM} ^{192}Ir wire source. The dosimetric differences were investigated following the formalism proposed by the AAPM TG-43 [37]. The study proposed a simple equation for accurate calculation of the dose rate constant of any ^{192}Ir source. It also found that radial dose functions of the sources did not depend significantly on source and encapsulation geometry and agreed within 2% with that of a point ^{192}Ir source.

Granero *et al* [65] used the GEANT4 Monte Carlo code to obtain dose rate distribution for the new ^{192}Ir HDR source, (type Ir2.A85-2) and ^{192}Ir pulsed dose rate (PDR), (type Ir2.A85-1) in water medium. In the Monte Carlo simulation the β spectrum of the ^{192}Ir source was not considered since its contribution to the dose rate distribution at a greater distance is negligible [66]. In general, the statistical uncertainty of Monte Carlo simulation was 1.1%. The study provided dosimetric parameters and dose rate tables for the new HDR and PDR sources. The study concluded that these dosimetric parameters can be used as input data as well as to verify the calculation of the treatment planning systems used in the HDR and PDR brachytherapy.

Since part of the current thesis is dealing with modelling of the MammoSite balloon on the basis of CT images, no studies have been performed to generate a model of ^{192}Ir source using DOSXYZnrc Monte Carol user code. This code has been chosen, in the current work, as it enables the simulation of the dose distributions using patient CT images.

2.2.6 Modelling of the linear accelerator

A Linear accelerator (linac) is a machine that produces beams of photons and electrons for radiotherapy treatment. The linac is routinely used by most radiotherapy centres around the world to treat cancer patients. The linac generates particles of energies in the megavoltage range depending on the specification of the machine. The photon beams have good penetration and exhibit skin sparing due to dose build-up whereas electron beams are used to treat superficial cancers and spare deeper normal structures due to rapid dose fall-off. Figure 2.8 shows a schematic diagram of a medical linear accelerator system modelled for a Monte Carlo simulation. The components in Figure 2.2.7 are usually the ones required in a Monte Carlo model. An accelerated primary electron beam hits a target, made of a high Z metal, in which the electrons will produce bremsstrahlung photons. The bremsstrahlung photons are then collimated by a primary collimator and the photon fluence is modified by a flattening filter to produce a flat dose distribution. The photon beam is finally shaped and modulated using components such as jaws, multi-leaf collimators and physical or dynamical wedges.

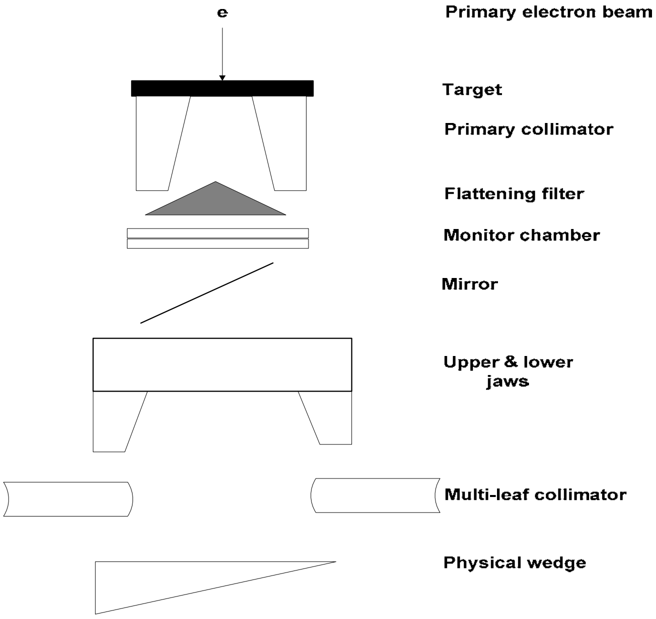

Figure 2.8. Schematic drawing of linear accelerator components modelled in a typical Monte Carlo simulation.

Mohan *et al* [67] employed EGS 3 Monte Carlo code to model a set of Varian linear accelerators producing photon beam energies of 4-25 MV. The model included a target, a primary collimator, a flattening filter and upper and lower jaws. Calculated photon spectra at 100 cm from the source were validated by comparing measured and calculated tissue maximum ratios (TMR) in water.

Kim *et al* [68] used the MCNPX Monte Carlo code to calculate the dosimetric characteristic of the photon beams from 6 MV Siemens MX2 and 10 MV Varian Clinac 2100C. The authors modelled the treatment head through the manufacturer specific geometry corresponding to the technical drawings of the two linacs. The accelerator components considered in the simulation consisted of the target, primary collimator, flattening filter, monitor chamber, mirror, upper jaws and lower jaws. The process of simulating the linac was similar to that employed by the BEAM user code. The study used the Monte Carlo simulation to calculate the energy spectra of the photon beam, percentage depth dose and dose profiles. The study compared Monte Carlo calculations with measured dose distributions for the two machines. The computed and measured depth dose (in water) curves agreed within 2% for all depths beyond the build-up region for both treatment machines. From comparison of the measurements, the study found that the MCNPX code is an effective tool for simulating clinical photon beams from a linear accelerator.

Sichani and Sohrabpour [69] used the Monte Carlo method to simulate the photon beam from a Theratron 780-C cobalt therapy unit. They used it to calculate the percentage depth dose and some radiation scatter factors for various field sizes. The calculations were carried out in a water phantom at a fixed source-surface distance of 80 cm. Their results were compared to other published data [70]. Excellent agreements were found and the differences with the measured values were of the order of or less than 1%.

Blazy *et al* [71] employed the Monte Carlo method to simulate the percent depth dose and dose profiles of a 12 MV photon beam. They used a heterogeneous phantom, which consisted of lung and bone heterogeneities. They found a good agreement between experimental measurements (obtained with small cylindrical ionization chamber) and Monte Carlo simulation for depth dose curves and dose profiles. The study found some discrepancies, near interfaces, between measurement and Monte Carlo. However, they believed that this discrepancy was not in the Monte Carlo code but due to the attenuation of the lower energy electrons by the wall of the ionization chamber.

Inserting a physical wedge in a photon beams alters the beam characteristics significantly. Not only is the dose distribution modified by attenuation and scatter from the wedge, but also the photon spectrum is affected. Monte Carlo can be used to model dynamic or physical wedges. When modelling a physical wedge, great care has to be taken that the model for the wedge is exact. Schach von Wittenau *et al* [72] used the BEAM [39] and DOSXYZ [73] Monte Carlo user codes to determine the fraction of energy exiting as bremsstrahlung photons from 1-5 cm thick iron and lead slabs. These slabs were used as simple models for wedges. The study found that wedge-generated bremsstrahlung photons carried about 20% of the outgoing energy in a 10 MV beam.

Shih *et al* [74] analysed the characteristics of dynamic wedges. The study compared dynamic wedges to physical wedges in terms of their differences in affecting beam spectra, energy fluence, angular distribution, contaminated electrons and dose distributions. The BEAM [39] Monte Carlo user code was used to simulate the exact geometry of a Varian 2100C 6 MV linac. The simulation was performed for dynamic and physical wedges with four different wedge angles (15^o, 30^o, 45^o, and 60^o) and different open fields. The user code DOSXYZ [75] was employed to calculate the 3-D dose distribution in a water phantom. The Monte Carlo results were first validated with measurements. The Monte Carlo results were found to agree within 2% with measurements performed in a water phantom. The Monte Carlo calculations revealed that the effects a dynamic wedge on beam spectral and angular distribution, as well as electron contamination were much less significant than those for a physical wedge. For the 6 MV photon beam, a 45^o physical wedge can result in 30% increase in mean photon energy due to the effect of beam hardening. It can also introduce 5% dose reduction in the build-up region due to the reduction of contaminated electrons by the physical wedge. Neither the increase in mean energy nor the reduction of the dose was found for the dynamic wedge. The study concluded that compared to a dynamic wedge; the physical wedge altered the photon-beam spectrum significantly.

Van der Zee *et al* [76] introduced a new component module in the BEAM code named WEDGE. The authors used this component to model the internal wedge in 6 MV and 10 MV photon beams of an Elekta SL linac. The study found that the presence of the wedge altered the primary and scattered photon components from the linac significantly: beam hardening of 0.3 MeV and 0.7 MeV was observed for the two components, respectively.

Verhaegen *et al* [77] used the BEAM Monte Carlo user code to model 6 MV and 10 MV dynamically wedged photon beam from a Varian 2100C linac. The study obtained excellent agreement between measured and calculated dose distributions.

Shih *et al* [78] used the BEAM code to calculate dosimetric characteristics of dynamic wedges for 6 MV and 18 MV photon beams generated by a Varian 2100C linac. The simulations were performed for dynamic wedges of wedge angles of 15^o, 30^o, 45^o, and 60^o, as well as open fields with different field sizes. The Monte Carlo calculated dose distributions were verified with the measurements in water. The Monte Carlo calculated percentage depth dose and beam profiles agreed with measurements within ± 2% or ± 2 mm in high dose gradient region. The dynamic wedge slightly altered energy spectra of photons and contaminating electrons. The slight changes had no significant effect on the percentage depth dose as compared to the open field. The Monte Carlo calculated dynamic wedge factors agreed with measurements to within ± 2%. The authors concluded that the Monte Carlo method provided more detailed beam characteristics for dynamic wedge fields than measurement methods. These beam characteristics included photon energy spectra, mean energy, spectra of contaminating electrons and effects of moving on off-axis beam quality. The study highlighted that these data are potentially important for treatment planning involving dynamic wedges.

A multi-leaf collimator (MLC) is a beam collimation device which consists of opposing pairs of motor driven leaves. The independent motion of leaves makes it possible to define irregular field shapes therefore allowing the radiation field shape to be conformed to the tumour. This has led to the replacement of conventional shield blocks with MLCs and, more recently, the application of MLCs to intensity modulated radiation therapy (IMRT). The MLC leaves can have very complex design for the leaf ends and the leaf edges which make them challenging to model in a linac.

De Vlamynck *et al* [79] used the BEAM code to simulate 6 MV photon beam from an Elekta SL25 linac equipped with MLC curved-leaf ends. The authors approximated the rounded shape of the MLC leaf-ends using a stack of MLC modules available in the BEAM code. The inter-leaf leakage was not modelled in the study. The study found a good agreement between the measurements and Monte Carlo calculations of depth dose profiles with deviations of less than 1%. It was also found that the calculated lateral dose profiles slightly exceeded the measured dose distributions near the high penumbra region for a 10 x 2 cm^2 field; this difference was attributed to the small size of the diamond detector. The simulations were also able to predict variations of output factors and ratios of output factors as a function of field width and field-offset.

Kim *et al* [80] modelled 6 MV and 18 MV photon beams from an 80-leaf Mark II MLC for the Varian 2100C linac and for 120-leaf Millennium MLC for the Varian 2100EX linac. The complex geometry of the MLC (including the rounded leaf ends, leaf edges, tongue-and-groove and offset notch, mounting slots and holes) was modelled using the MCNP4b Monte Carlo code. The study investigated the characteristics of radiation leakage through the MLC. Dose for 6 MV and 18 MV beams was calculated at 5 cm depth in a water phantom located at 95 cm SSD, and then normalized to the dose for an open field. They found that for the 80-leaf MLC at 6 MV, the average radiation leakage dose was of about 1.6%, 1.7%, 1.8% and 1.9% for 5 x 5, 10 x 10, 15 x 15 and 20 x 20 cm^2 field sizes, respectively. For the 120-leaf MLC at 6 MV, the average radiation leakage dose was 1.6%, 1.6%, 1.7% and 1.9% for the same field sizes. The measured and calculated leakage values for the 120-leaf MLC were in agreement to within 0.1% of the open field dose. The increased leakage with field size was attributed to MLC scatter radiation. It was also observed that the MLC attenuation significantly affected the photon spectrum, which resulted in an increase in percentage depth dose for 6 MV, however, little effect was observed for the 18 MV beam.

Kapur *et al* [81] introduced a new BEAM component module, called VARMLC that allows modelling the tongue-and-groove effect of some of the Varian MLCs. The leaves are modelled as diverging rectangular slabs with interlocking tongue and groove and either rounded or focused leaf ends. Heath *et al* [82] developed a new component module to fully model the geometry of the Varian Millennium 120-leaf collimator using the BEAMnrc Monte Carlo user code. the new module, a modification of the VARMLC component module [81], was named DYNVMLC. The model accounted for details such as the leaf driving screw hole, supporting railing groove and leaf tips for the Varian Millennium 120-leaf collimator. The study found that the simulated depth dose and off-axis profiles for a variety of MLC fields agreed to within 2% with ion chamber and diode measurements in a solid water phantom. Lydon [83] performed Monte Carlo simulation using the BEAMnrc user code for the simulation of Varian Mark II 2100C linear accelerator equipped with an 80 leaf MLC. Manufacturer specifications were used to set up the linear accelerator geometry using independent component modules supplied with the BEAMnrc code. The MLC was modelled using the VARMLC component module that allows the rounded leaf ends, tongue and groove and internal gap to be specified.

2.2.7 Conclusions

In summary, this Chapter has reviewed the basic principles of Monte Carlo dose calculation techniques as well as some literature related to modelling of HDR brachytherapy and linear accelerator. In this work, the EGSnrc Monte Carlo code will be employed to construct two separate models of the MammoSite brachytherapy and external beam radiotherapy treatment techniques. For the MB, a model will be generated for the

HDR microSelectron ^{192}Ir source while for EBRT a Monte Carlo model for a Varian 600C/D clinical linac is built. The models will be validated with measurement data for accuracy.

The Monte Carlo models will be used to simulate the individual dose distributions using patient CT images undergone early stage breast cancer treatment. The Monte Carlo computed dose distributions will be combined together to visualize the final dose matrix of both modalities. This is important, because clinically the two modalities use different dose calculations algorithm which make it impossible to combine the final dose distributions. An in-house Matlab code is developed to process the three-dimensional dose distributions obtained from Monte Carlo simulations.

Chapter 3

Modelling of high dose rate ^{192}Ir brachytherapy source

3.1 Introduction

Only a limited number of studies have performed Monte Carlo simulations for the MammoSite balloon [11, 12, 84, 85]. Cheng et al [84] calculated the dose distributions for the ^{192}Ir source with the user-code DOSRZnrc [86]. This code calculates the dose distribution in a cylindrical geometry. In their study, the cylindrical phantom was divided into small shells to represent the MammoSite balloon and the dose distribution was calculated with the ^{192}Ir source placed at the centre of the MammoSite balloon. The DOSRZnrc Monte Carlo code cannot be used to perform dose calculation using CT data of the MammoSite balloon. Since the current thesis is based on dose calculation using CT images of a patient with the MammoSite balloon inserted, the DOSXYZnrc [56] user code was used for dose calculations instead of the DOSRZnrc user code as patient CT data are in a Cartesian coordinate system. This chapter aims to generate a model of the Ir-192 brachytherapy source and investigates the effect of voxel size on dose calculation around the modelled ^{192}Ir source.

3.2 Materials and methods

3.2.1 Description of ^{192}Ir source

The microSelectron-HDR ^{192}Ir source (Nucletron International, Veenendaal, The Netherlands) is modelled in the current study. Figure 3.1 shows a schematic diagram of the geometry of this source. It consists of a cylindrical iridium core of 0.7 mm in diameter and 3.6 mm in length. The core is encapsulated by a stainless steel tube of 0.9 mm outer diameter and 4.5 mm in length. The encapsulated source is connected to a drive cable of 0.7 mm in diameter. The ^{192}Ir source emits a wide spectrum of γ-rays of relatively low energies, mostly in the range of 201-884 keV with an average value of 360 keV, and has a relatively high atomic number (Z = 77) [87]. Borg et al [61] calculated the photon spectrum around the microSelectron HDR ^{192}Ir source using the FLURZnrc user code. In their work the source was modelled as a cylindrical core volume with the photons being emitted from homogenously distributed points (using the uniform isotropically radiating cylinder source routine in the FLURZnrc user code). The γ-ray spectrum used in their study for the microSelectron-HDR ^{192}Ir consisted of 34 energy bins ranging from 0.060 to 0.885 MeV [61]. This spectrum is available within the EGSnrc Monte Carlo software, 'Ir192-microSelectron-spectrum', and has been used in the current study. Figure 3.2 shows the fluence spectrum for the microSelectron-HDR brachytherapy source [88]. The spectrum for the microSelectron-HDR source was calculated with both air and vacuum surrounding the source. There was no difference between the spectra calculated in air and in vacuum.

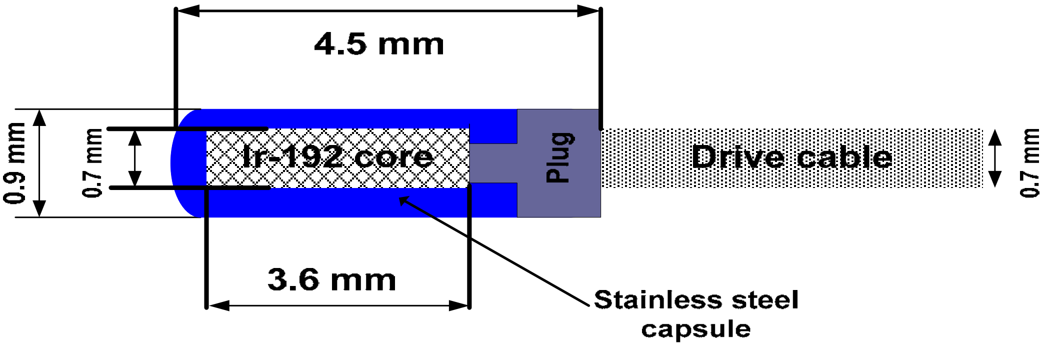

Figure 3.1. A schematic diagram of the Nucletron 'microSelectron' ^{192}Ir HDR source.

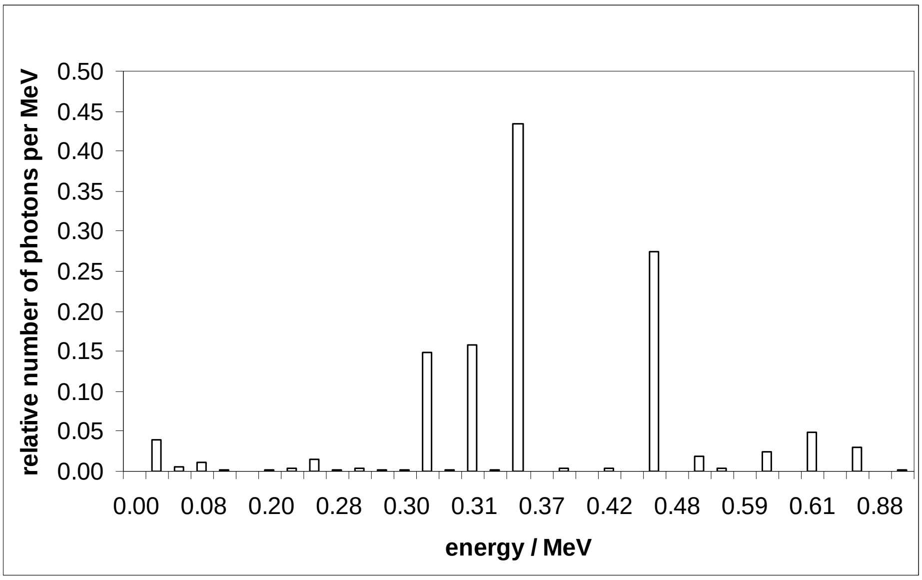

Figure 3.2. The fluence spectrum for the microSelectron-HDR brachytherapy source.

3.2.2 Source modelling

The DOSXYZnrc user code was described in detail in Chapter Two. It simulates the transport of photons and electrons in several media. Monte Carlo simulation with the DOSXYZnrc user code requires a user input file, containing user-specified parameters required for calculation such as the source type and its dimensions in Cartesian coordinates, energy cut-off values for the transported photons and electrons, and Monte Carlo transport parameters.

In this study, the cylindrical shape of the ^{192}Ir source was approximated in the Cartesian coordinate system using an isotropically uniform parallelepiped radiating source routine available within the DOSXYZnrc user code. This approximation is a reasonable one since the real ^{192}Ir source has small dimensions and may be considered as a point source as prescription distances are generally several centimetres away. The real dimensions of the real Ir^{192} were modelled. The absorption of radiation in the steel capsulation was included in the γ-ray spectrum.

Figure 3.3 shows a schematic projection of the real ^{192}Ir source, which is a cylinder of 0.7 mm in diameter (d) and 3.6 mm in length (z), and projection of 2 parallelepiped sources simulated in the Monte Carlo calculations, with dimensions indicated for source model 1 and source model 2. The parameters x, y and z represent the width, depth, and length of the modelled ^{192}Ir source respectively. Source model 1 was chosen so that the shape of the real ^{192}Ir source was enclosed in the parallelepiped source of dimensions (X ∗Y ∗ Z) of 0.7 x 0.7 x 3.6 mm^3. The values for X and Y were set to equal to the diameter of the real ^{192}Ir source, while Z was set to the length of the source.

For source model 2, the modelled source was enclosed in the real ^{192}Ir source. The dimensions of source model 2 were of 0.5 x 0.5 x 3.6 mm^3. The value for Z was set to the length of the real ^{192}Ir source, and the values of X and Y were calculated as follows:

$$d = \sqrt{X^2 + Y^2}\ , \qquad (3.1)$$

where d is the diameter of the real ^{192}Ir source. By setting X = Y

$$X = \frac{d}{\sqrt{2}}, \qquad (3.2)$$

The dimensions of the source model 3, which is not shown in Figure 3.3, were of 0.6 x 0.6 x 3.6 mm^3. The dimensions of the source model 3 were taken as the average dimensions of the source model 1 and the source model 2 as follows:

$$X = X\ (\text{source model 1}) + X\ (\text{source model 2}) / 2 \tag{3.3}$$

and the same equation was used for Y and Z dimensions.

An input and listing simulation file, for the Monte Carlo model of the ^{192}Ir source, is presented in Appendix A. Monte Carlo simulations were done for each source model to find out whether the approximation has any effect on dose calculations. The modelled ^{192}Ir source was placed at the centre of a water phantom with dimension of 25 cm x 25 cm x 18 cm as shown in Figure 3.4.

Up to 1x10^9 histories were simulated in order to get statistical uncertainties of less than 2%. This took about 32 hours of simulation time for each run. At the end of the simulation the STATDOSE [57] user code was used to extract dose distribution profiles and the dose decrease as a function of distance was plotted. Furthermore, an in-house developed Matlab (version 7.0.4, The Math Work, Inc.) code, see Appendix B, was used to extract 2D dose maps around the modelled ^{192}Ir sources.

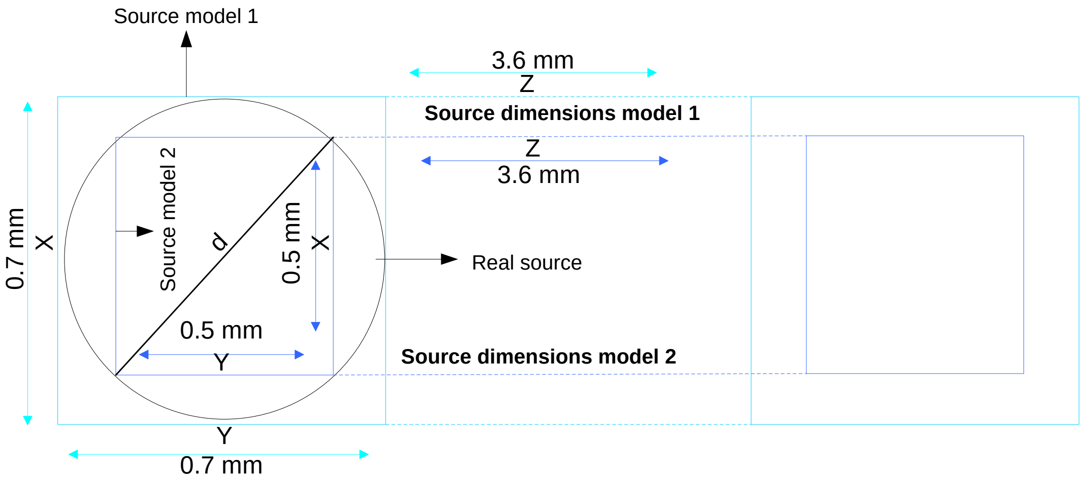

Figure 3.3. Schematic of the source geometry (not to scale) used in the Monte Carlo simulation. It is a representation of the cylindrical shape of ^{192}Ir source approximated in DOSXYZnrc code.

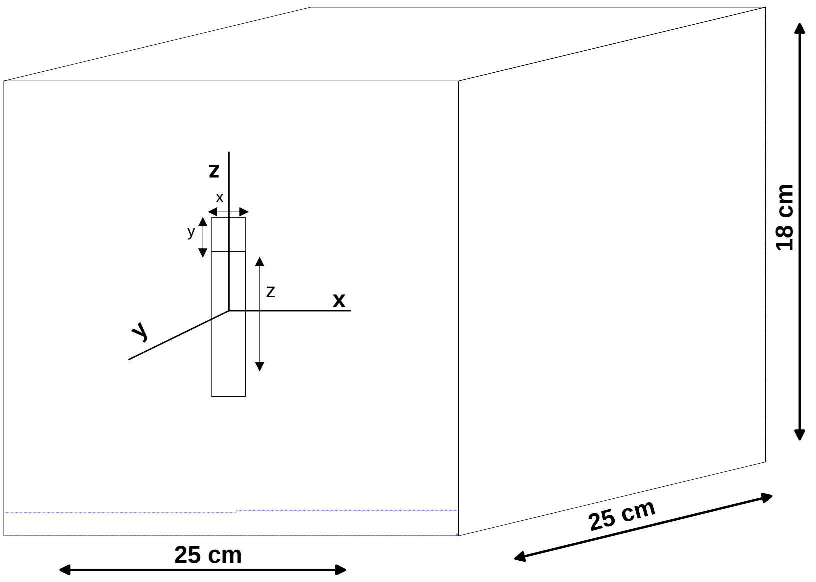

Figure 3.4. The modelled ^{192}Ir source placed at the middle of a cubic water phantom (phantom not to scale).

3.2.3 Voxel size effects

The effect of voxel size used in the Monte Carlo calculations on the accuracy of dose distribution around the modelled ^{192}Ir was investigated. This is particularly important in brachytherapy where dose distributions have steep dose gradients. The voxel size determines the average integral dose in the specified volume. The calculated dose in the voxel represents the dose at the middle point of the voxel. If the voxel size is too large it will be averaging the dose distribution from a large volume (in voxels) and losing detailed information about the dose gradient. The dose was calculated with different voxel sizes with the source positioned at the centre of 25 x 25 x 18 cm^3 water phantom. The dimensions of the voxels were cubes of 1, 1.5, 2, 3, 4 and 5 mm^3 volumes. Up to 10^9 incident particle histories were simulated for each run. The uncertainty (σ) in the Monte Carlo simulation is inversely proportional to the square root of the number of simulated particle (N) in the dose simulation:

$$\sigma = \frac{1}{\sqrt{N}}, \qquad (3.4)$$

Following the simulation, the 3D dose output files were processed using STATDOSE program and the impact of voxel size on the dose distribution around the brachytherapy source was investigated.

3.2.4 Importing of CT data to EGSnrc Monte Carlo code

As mentioned before, EGSnrc / DOSXYZnrc is capable of performing Monte Carlo simulations using patient CT images. However, the EGSnrc Monte Carlo code does not work with CT slices but with the volume of CT data. Therefore, each CT slice had to have the header stripped away and all image data were stacked together into one data file as required by EGSnrc code. This process was performed using the Pinnacle^3 treatment planning system. The CT dataset header file and the binary data file were then imported to the EGSnrc code.

An input file was created in the EGSnrc code to read the CT data header file. The input file also defined several variables such as the volume of the CT data, the density of the materials and others. The density of the MammoSite balloon was assigned a CT number of 2000 as calculated by the Pinnacle^3 treatment planning system. The input file was then compiled to generate a CT data volume readable for simulations using DOSXYZnrc.

3.2.5 Simulation of MammoSite brachytherapy treatment

The CT dataset, from the previous section, was used for dose calculations using DOSXYZnrc. Figure 3.5 summarizes the steps involved for Monte Carlo simulations. For the simulation of MammoSite treatment, the modelled ^{192}Ir source was placed at the centre of the balloon. The MammoSite balloon was 4 cm in diameter. The voxel size for the Monte Carlo dose simulation was a cube of 1.5 mm^3. The simulations were run with a number of particles that would result in a statistical error of less than 2% at 1 cm from the balloon surface; it needed up to 2×10^8 particles and a CPU running time of approximately 25 h. The 3D dose distribution data file, produced by the DOSXYZnrc simulation, was analysed using an in-house developed Matllab code (Appendix B).

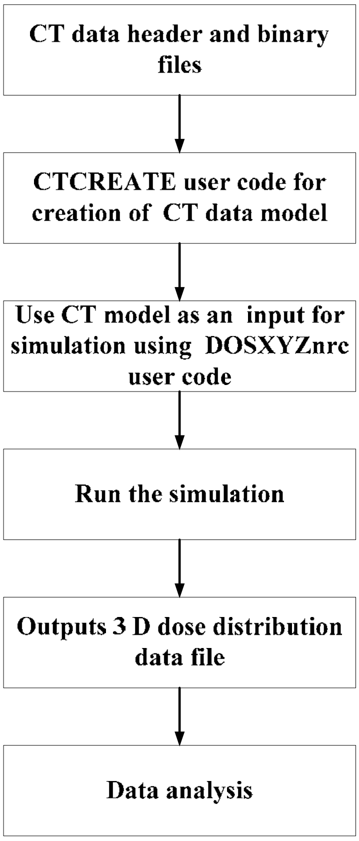

Figure 3.5. Steps involved for Monte Carlo dose calculation in the breast.

3.3 Results and discussions

3.3.1 Source modelling

The first set of simulations dealt with source geometry modelling. The ^{192}Ir source was modelled using DOSXYZnrc which calculates the dose in a rectilinear coordinate system. In the source modelling, the dose distributions for the three simulated source dimensions were calculated. The dose reading (dose / incident particles, Gy) at a point located 3 cm (corresponding to prescription distance) from the modelled source, with dimensions of 0.6 mm x 0.6 mm x 3.6 mm, was 1.72 x10 $^{-14}$. The dose readings were 1.69 x 10 $^{-14}$ and 1.69 x10 $^{-14}$ for the modelled sources with dimensions of 0.7 mm x 0.7 mm x 3.6 mm and 0.5 mm x 0.5 mm x 3.6 mm respectively. At this distance the statistical uncertainty associated with the Monte Carlo simulation was about 1.9% and increased slightly at other distances. The percentage difference in dose readings was 1.6%. The differences were smaller than the standard error (of ~ 2%) for each calculation at the given point. The dose reading from the modelled source, with dimension 0.6 x 0.6 x 3.6 mm^3, was used as a normalization point.

The dose fall-off profiles for the modelled parallelepiped ^{192}Ir sources, for the different dimensions, were in agreement at any distance from the source. The radial dose profile for the modelled ^{192}Ir source, with dimension of 0.6 mm x 0.6 mm x 3.6 mm, was extracted at 3 cm distance from the source and normalized to its maximum dose value. The radial dose profiles were also extracted for the modelled source 1 and the modelled source 2. In the source modelling, the dose distributions for the three simulated source dimensions were nearly identical as shown in Figure 3.6, for source dimensions slightly smaller and slightly larger than the diameter of the real ^{192}Ir source.

Since the difference between the volumes of the real ^{192}Ir source (0.0014 cm^3) and the simulated parallelepiped source model 3 (0.0013 cm^3) is the smallest, the real ^{192}Ir was approximated in the subsequent calculation as a parallelepiped source with dimensions of 0.6 x 0.6 x 3.6 mm^3. As shown in Figure 3.6, the differences in shape and volume between the real and simulated ^{192}Ir source will have no significant impact on the calculation of dose distribution in the breast from the MammoSite technique at prescription distances (~ 3-4 cm from the balloon centre). The Monte Carlo simulation of source modelling was validated with thermoluminescent dosimetry (TLD) measurements and the results of the two methods were in agreement. The results of Monte Carlo source modelling and TLD measurements will be discussed in more detail in Chapter Five. However, it is important to show an experimental validation of the Monte Carlo calculations here. Figure 3.7 presents a direct comparison of the TLD measured relative dose and the Monte Carlo computed dose as a function of distance, performed in breast tissue equivalent phantom, starting at 3 cm from the modelled ^{192}Ir source. The dose pattern shows a sharp fall off as a function of distance from the balloon surface. The measured and Monte Carlo calculated dose is in agreement within the measurement uncertainty and Monte Carlo statistical errors. The measurement uncertainty and Monte Carlo statistical error were 3% and 1.8% respectively.

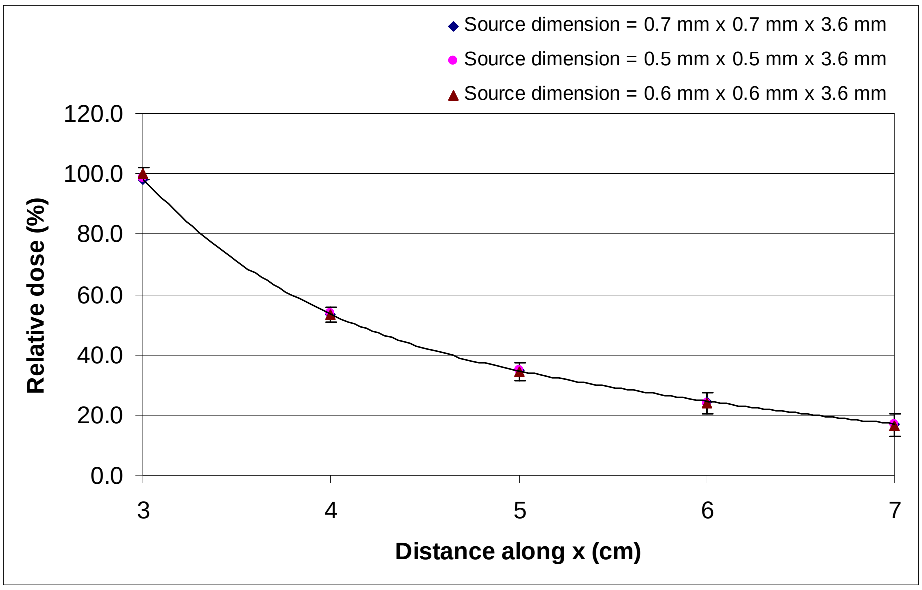

Figure 3.6. A comparison of the dose fall-off as a function of distance for the ^{192}Ir models with three different dimensions.

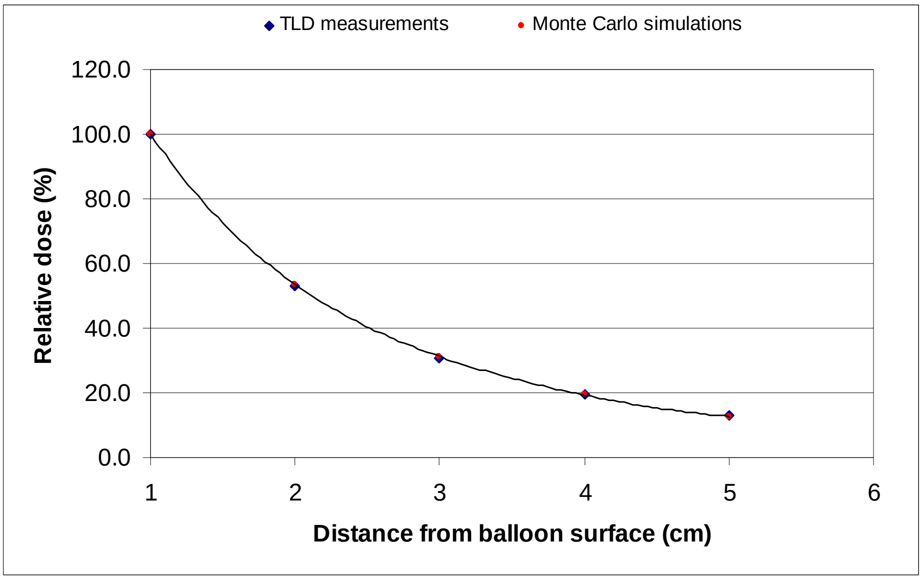

Figure 3.7. Comparison of the dose fall-off, for the modelled ^{192}Ir source, as a function of distance between the TLD measurements and Monte Carlo simulation. The uncertainties in Monte Carlo calculation and TLD measurements were 1.8% and 3% respectively.

Figure 3.8 shows the dose distribution around the modelled source, placed in a water phantom, with dimensions of 0.6 x 0.6 x 3.6 mm^3. The dose matrix was extracted at 3 cm from the source and normalized to its maximum dose point.

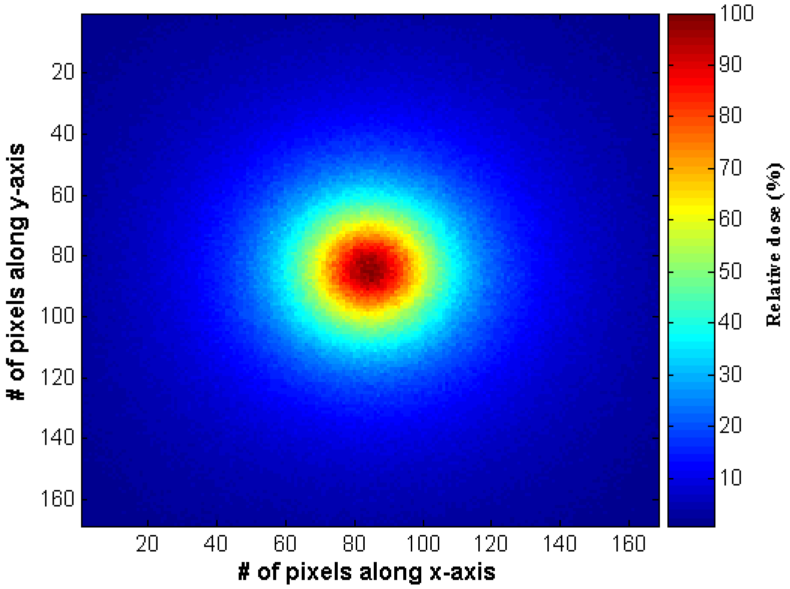

Figure 3.8. Two dimensional dose distribution around the modelled ^{192}Ir source with dimension 0.6 x 0.6 x 3.6 mm^3. The modelled source was placed at the centre of a water phantom.

3.3.2 Voxel size

The second set of simulations investigated the impact of voxel size on the averaging of the dose distribution. The dose profiles, at 3 cm away from the source centre for various voxel sizes are plotted in Figure 3.9. It can be seen that the dose scored in a voxel size of 1 mm^3 is similar to that scored in a voxel of size 1.5 mm^3. Furthermore, the voxel size of 1.5 mm^3 resulted in simulation time of 25% less than that of 1 mm^3 voxel size with the same statistical errors (~ 2%) at 3 cm from the source or more. As the voxel size is increased the simulation time is decreased as shown in Figure 3.10. However, increasing the voxel size produced an overestimate of the dose at 3 cm from the source centre as seen in Table 3.1. At this point the dose calculated with 2 mm^3 voxel was about 8% lower than the value calculated using voxels of 1 mm^3 and 1.5 mm^3. Figure 3.11 shows the effect of lower resolution voxel size on the dose distribution for the modelled ^{192}Ir source. It causes a loss of detailed information in the region of interest. As a result a voxel size of 1.5 mm^3 was chosen as suitable for performing Monte Carlo dose calculations for the MammoSite brachytherapy technique as reducing the voxel size further would not yield more information about the dose distribution and would only increase the simulation time.

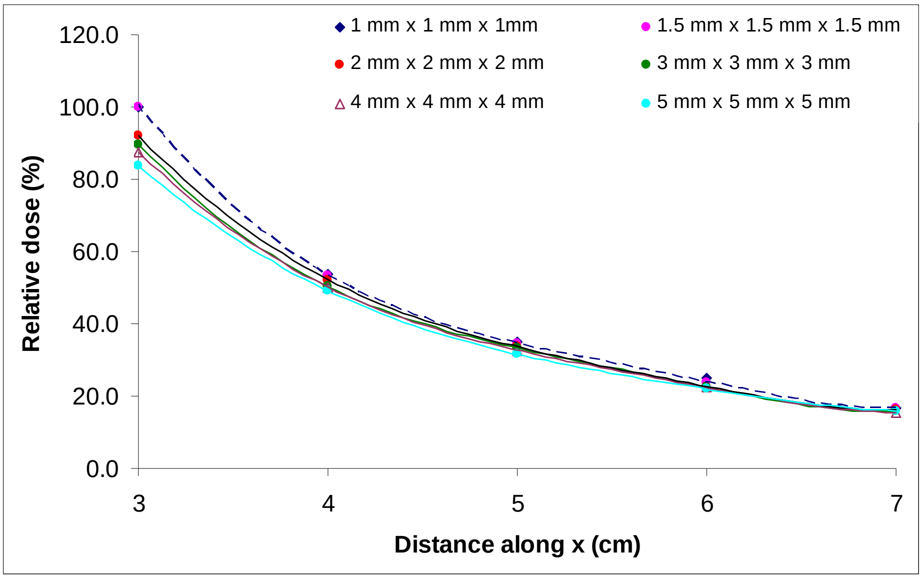

Figure 3.9. A plot of dose scored starting at 3 cm from the source with different voxel Sizes. The Monte Carlo statistical uncertainty was within 2%.

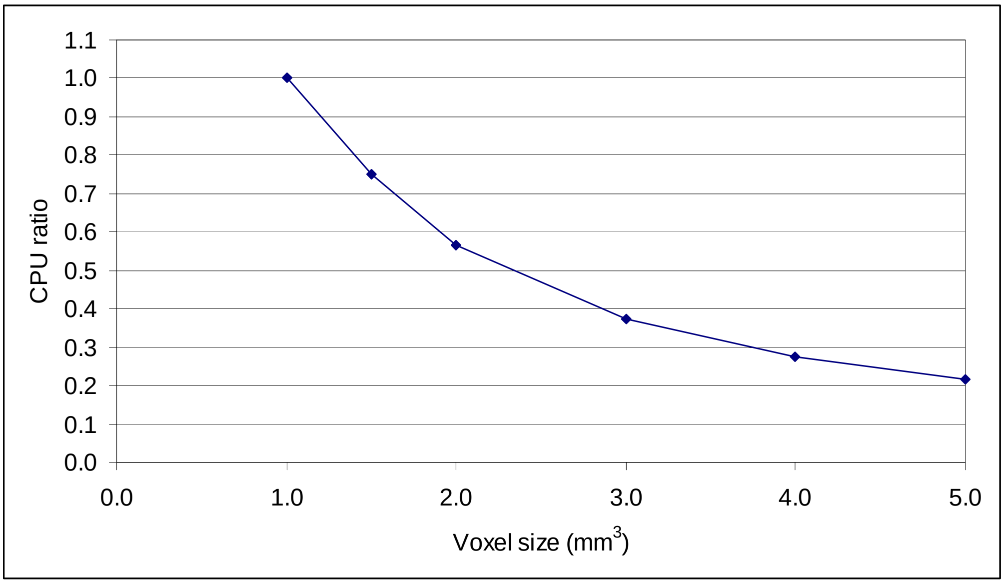

Figure 3.10. Voxel size and CPU ratio.

Table 3.1. Dose ratio for different centre voxel sizes at 3 cm from the source.

Voxel size (mm^3)	Dose ratio
1	1.0
1.5	1.0
2	0.92
3	0.90
4	0.88
5	0.84

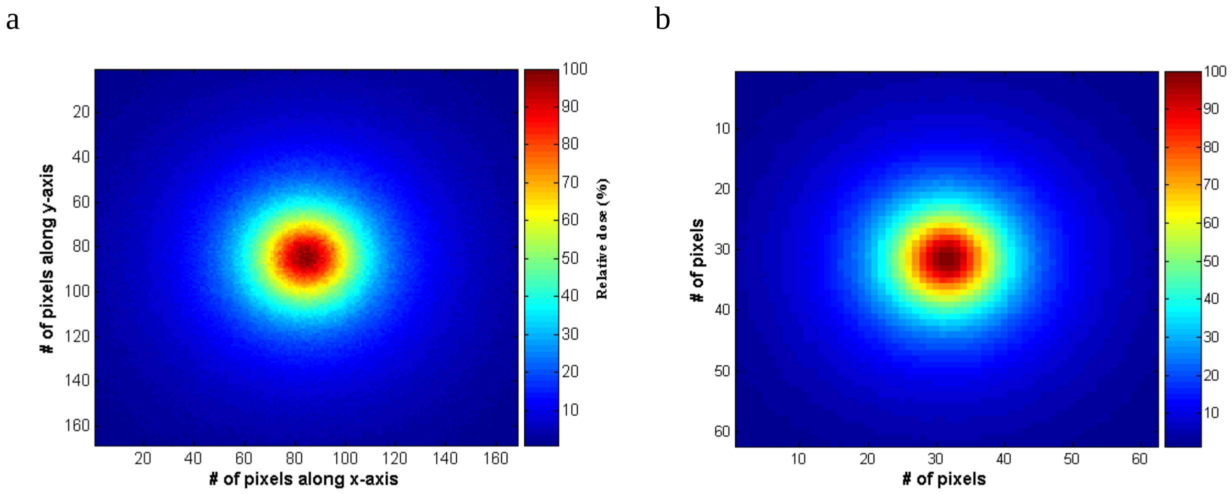

Figure 3.11. Dose distribution around the modelled ^{192}Ir source with voxel size of (a) 1.5 mm^3 and, (b) 4 mm^3. The voxel size effect is clearly visible.

3.3.3 Dose calculations in the breast

Figure 3.12 shows the 2D dose distribution at 1 cm from the balloon surface using a patient CT dataset. The dose matrix was normalized to its maximum point value. The dose outside of the breast was set to zero during the Monte Carlo simulation as it is not of importance in the current investigation.

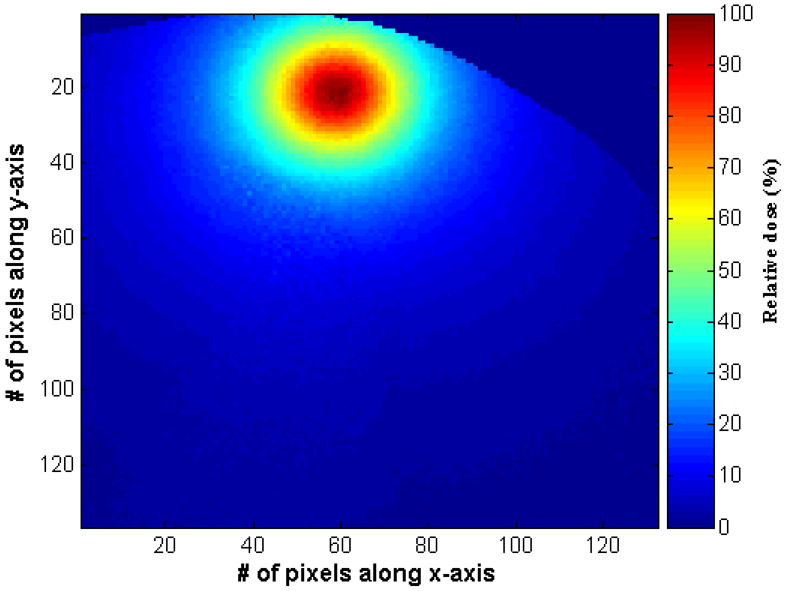

Figure 3.12. 2D dose distribution at 1 cm from the balloon surface.

3.4 Conclusions

The source modelling results revealed that the ^{192}Ir source can be approximated as a parallelepiped source in the DOSXYZnrc user code. The dose profiles of the three simulated sources were in agreement within the statistical uncertainty. The comparison was made at 3 cm from the source, as this distance is the region of interest when using the MammoSite brachytherapy technique for treatment of early stage breast cancer. On the basis of this study, the real ^{192}Ir source may be approximated in the DOSXYZnrc code as a parallelepiped source with dimension of 0.6 mm x 0.6 mm x 3.6 mm. It is expected that the differences in shape and volume between the real and modelled ^{192}Ir source have no significant impact on the calculation of dose distribution in the breast from the MammoSite technique as this is prescribed at larger distances from the source. The Monte Carlo model of the ^{192}Ir source was validated against measurements using TLDs. The results showed that an accurate Monte Carlo model has been constructed for the ^{192}Ir source.

To investigate the effect of voxel size on the accuracy of dose estimation, calculations were performed with six different voxel sizes. It is found that voxel sizes of greater than 1.5 mm^3 lead to overestimation of the dose by 8-16% at 3 cm from the source. To take advantage of the reduced calculation times a voxel size of 1.5 mm^3 was chosen instead of 1 mm^3. Based on this study, it is concluded that a voxel size of $\leq$ 1.5 mm may be used for Monte Carlo calculations to insure accurate dose distribution from MammoSite technique. CT data were successfully used as input in the EGSnrc Monte Carlo code and dose calculations were performed. Unlike the Plato brachytherapy treatment planning system this Monte Carlo model can accommodate dose inhomogeneities.

The ^{192}Ir source was accurately modelled using the EGSnrc Monte Carlo code. A CT data model was also created and used for dose calculations in the breast. The Monte Carlo model will be used (in Chapters 4 and 5) for investigating the impact of uncertainties associated with the MammoSite technique on the dose distribution in the breast. It will also be used for combining the dose distributions with an external beam radiotherapy model in Chapter 7.

Chapter 4

Uncertainties in source position and balloon deformation and their impact on NTCP and TCP

4.1 Introduction

In the MammoSite brachytherapy, the tumour bed volume is irradiated with high dose per fraction in a relatively small number of fractions. The MammoSite brachytherapy, as with any other radiotherapy technique, aims at delivering the prescribed dose to the treated volume while simultaneously avoiding complications to the adjacent normal tissues. Accurate source positioning at the balloon centre and minimal balloon deformation are important for desired dose delivery with the MammoSite applicator. Uncertainties in the source position and a small or large deformation of the balloon shape (elliptical shape) may perturb the prescribed dose to the treated volume. For example, if some regions of the planning target volume (PTV) receive less than the prescribed dose, it could lead to a greater risk of tumour recurrence. Portions of the PTV can also receive more than the prescribed dose. This in turn may result in the exposure of critical organs (heart, lung and skin) to extra dose. Hence, it is useful to use the biological models to predict the effect of these particular uncertainties on the MammoSite treatment outcomes, as well as to identify their acceptable limits.

In this chapter, the impact of balloon deformation and uncertainties in source position on the tumour control probability (TCP) and the normal tissue complication probability (NTCP) will be assessed. The effects on the treatment outcome will be assessed from (a) organ dose volume histograms (DVHs) obtained from the Plato brachytherapy planning system (Plato BPS v14.3.2, Nucletron B-V., Veenendaal, The Netherlands) and (b) EGSnrc Monte Carlo (MC) simulations based on actual patient CT images.

4.2 Materials and methods

4.2.1 Monte Carlo simulations

Patient CT dataset was imported into the EGSnrc Monte Carlo code and converted into patient geometry dataset using CTCREATE user code [38]. DOSXYZnrc user code was used for dose calculations using the converted CT dataset. In the simulation of MB treatment plan, the modelled ^{192}Ir source (discussed in chapter three) was first placed at the centre of the balloon with its axis aligned with the balloon axis. The photon emission from the modelled ^{192}Ir source was assumed to be isotropic. As mentioned in Chapter 3, the γ-ray spectrum for the ^{192}Ir was taken from a published report and consists of 34 energy bins ranging from 0.060 to 0.885 MeV [61].

In order to investigate the impact of source position and balloon deformation uncertainties, the source was then shifted up to 5 mm by a margin of 1 mm along the longitudinal axis to investigate sufficient range of positioning errors. The voxel size of the 3D scoring geometry was 1.5 mm x 1.5 mm x 1.5 mm. In each simulation, up to 2 x 10^8 incident particles were tracked resulting in an overall relative statistical uncertainty of less than 2% at the prescription point and CPU running time of approximately 25 h. At the end of the simulations, the computed 3D dose distributions were analysed using STATDOSE user code and in-house developed Matlab code.

4.2.2 DVH analysis

The CT images of a patient were also sent to the Plato brachytherapy planning system (Plato BPS v14.3.2) for the balloon position and shape verification, treatment planning and dose calculations. The balloon-cavity conformance, balloon symmetry and the distance from the surface of the balloon to the skin were measured and examined on the CT images. The planning target volume (PTV) was defined as the volume of tissue extending 10 mm from the balloon surface. The balloon was not considered to be part of the PTV. The minimum distance from the balloon surface to the skin on any CT slice was 7 mm. Critical organs and sensitive tissues, including lungs, heart and the normal breast tissue including skin, were also contoured.

The source used in this study was the ^{192}Ir source used with nucletron microSelectron-HDR (Nucletron International, Veenendaal, The Netherlands). It had a typical activity of approximately 10 Ci (370 GBq), and is attached to a computerized drive mechanism used to move the source to the predetermined dwell position within the applicator catheter. A treatment plan was developed with the source at the balloon centre and a dose of 3.4 Gy was prescribed to a 10 mm radial distance from the surface of the balloon (according to the departmental protocol). Figure 4.1 shows an example of the dose distribution for CT planning as calculated by Plato brachytherapy treatment planning system.

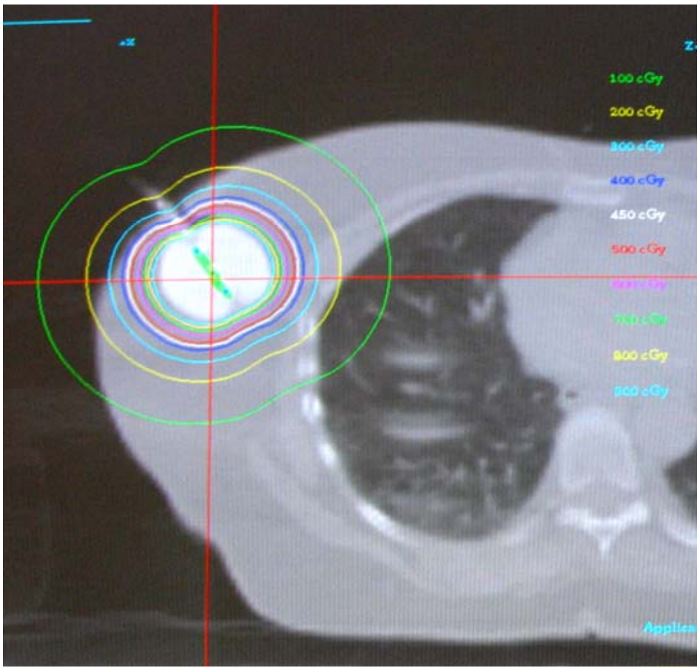

Figure 4.1. An example of dose distribution as calculated by Plato BPS (v 14.3.2, Nucletron). It is to be noted that Plato does not correct for inhomogeneities.

Dose volume histograms were generated for the PTV, lung, heart and ipsilateral breast (including skin). The current study considered that the MammoSite is delivered as monotherapy according to protocol of 10 fractions. As a result, the dose in each bin of the dose volume histogram was multiplied by 10 in this study, assuming for simplification that the geometry of the balloon and patient anatomy were consistent during the 10 fractions. The balloon was then deformed (adjusting the contours) by up to 4 mm in 1 mm steps and similarly 3.4 Gy was delivered at the prescription point. This deformation margin was chosen since typical treatment protocols allowed 4 mm balloon deformation [2]. Dose volume histograms were constructed for each treatment plan with balloon deformation. The average volumes of the lung, heart and breast were 1563 cm^3, 301 cm^3 and 560 cm^3 respectively. The DVHs were imported from the treatment planning system and used for NTCP and TCP calculations.

4.2.3 Physical dose conversions

The physical dose in each bin of the differential dose volume histogram, for the PTV and the normal tissues, was converted into biological effective dose. The biological effective dose based differential dose-volume histograms ($BE_{ff}D$-DVHs) were further converted into equivalent dose based differential dose volume histograms (D_{eq}-DVH). The equivalent dose is the dose that gives an effect equivalent to that of conventionally fractionated irradiation delivered in 2 Gy fractions [89]. The reason for this conversion is that the parameters of the NTCP models presented in the literature were derived from conventional external beam radiotherapy with the assumption that the dose per fraction is 2 Gy. Using this conversion, it is also possible to caculate NTCPs for different irradiation schemes. The equivalent dose was calculated for each bin of the differential dose volume histogram according to the following equation [89]:

$$D_{eq} = \frac{BE_{ff}D}{1 + \dfrac{d_{ref}}{\alpha / \beta}} \quad , \tag{4.1}$$

where d_{ref} = 2 Gy is the reference dose per fraction for conventionally fractionated external beam radiotherapy treatment schedule and α/β ratios (in units of Gy) are an indication of radiosensitivity of a given tumour or normal tissue due to changes in fractionation or dose rate. The values of α/β ratios are as shown in Table 4.1

4.2.3.1 Biological effective dose

The doses in the dose-volume histograms are the conventional (physical) doses which do not provide clinically easy to understand representation of the biological effect corresponding to the various fractionated radiotherapy modalities. Physical doses do not take into account the many factors influencing the effects of the dose on the tissue under consideration. Among these factors are the α/β ratios of the tissue, fraction size, treatment delivery time and etc. For this reason, the concept of biological effective dose ($BE_{ff}D$) was developed as it incorporates information about the factors related to the delivery of the treatment and tissue specific factors [90]. In the current work the physical dose in each bin of the differential DVHs of the irradiated critical organs, calculated by Plato TPS, was converted into a biological effective dose ($BE_{ff}D$) using the following equation [90]:

$$BE_{ff}D = TD \times RE \ , \tag{4.2}$$

where *TD* is the total physical dose in each bin of the differential DVH from ten fractions and *RE* is the relative effectiveness. The *RE* is a dose modifying factor that takes into account the radiobiological parameters (α/β ratio) and the type of radiation delivery mode (external beam therapy or brachytherapy). The *RE*, for high dose rate brachytherapy, for irradiated normal tissues was calculated using the following relation [90]:

$$RE = 1 + \frac{2R_0\lambda}{\mu-\lambda}\left(\frac{\beta}{\alpha}\right) \times [1-e^{-\lambda T}]^{-1} \times \left\{\frac{1}{2\lambda}[1-e^{-2\lambda T}] - \frac{1}{\mu+\lambda}[1-e^{\{-T(\mu+\lambda)\}}]\right\}, \qquad (4.3)$$

$$\mu = \frac{0.693}{T_{1/2}}, \qquad (4.4)$$

where

λ is the radioactive decay constant (= 0.004 h^{-1}),

$T_{1/2}$ is the half-life of sublethal damage (h)

R_0 is the initial dose rate (= 22.75 Gy h^{-1}),

μ is the sub-lethal damage repair constant (h^{-1}),

α / β are constants (Gy) biological parameters dependent on tissue type within the volume being treated.

T is the total treatment time (= 0.15 h),

The *RE* was calculated using published values of related parameters of critical tissues [91-94]. Table 4.1 summarizes the values of the parameters fitted Equation 4.3

Table 4.1. Parameters selected to calculate relative effectiveness.

Organ	Endpoint	α/β (Gy)	$T_{½}$ (hour)	μ (h^{-1})
Lung	Pericarditis	1	3	0.17
Heart	Pneumonitis	3	3	0.17
Skin	Desquamation	11	1.2	0.58
	Erythema	8	1.2	0.58
	Telangiectasia	2.8	3.5	0.20
	Fibrosis	1.7	4.4	0.16

4.2.4 NTCP calculations

The normal tissue complication probabilities were estimated using the Lyman and relative seriality models. NTCPs were calculated for the lung, the heart, and the normal breast tissue using the equivalent dose based differential DVHs (D_{eq}-DVHs).

4.2.4.1 The Lyman model

The Lyman [95] model is widely used in the calculation of normal tissue complication probability. This model is based on the error function for describing the dose-response relationship for normal tissues. The normal tissue complication probability for uniform dose (D) to a fraction (ν) of the organ is given by [95]:

$$NTCP = \frac{1}{\sqrt{2\pi}} \int_{-\infty}^{t} \exp\left(\frac{-x^2}{2}\right) dx \,, \tag{4.5}$$

$$t = \frac{D - TD_{50}(\nu)}{m \cdot TD_{50}(\nu)} \,, \tag{4.6}$$

$$TD_{50}(1) = TD_{50}(\nu) \times \nu^{n} \,, \tag{4.7}$$

$$\nu = \frac{V}{V_{ref}} \,, \tag{4.8}$$

where D is the uniform dose, $TD_{50}(1)$ is the tolerance dose for 50% complications following whole organ irradiation, $TD_{50}(\nu)$ is the 50% tolerance dose to the partial volume ν, V is the total volume of the organ, V_{ref} is the reference volume (usually the whole volume) where possible, otherwise it is arbitrary reference volume, m and n are fitting parameters that account for the volume effect. The parameters m and n are empirically obtained from normal tissue tolerance data. The parameter m is the slope of the dose response function at TD_{50} and is thus a measure of the dose sensitivity of the organ. The parameter n is a measure of the volume effect.

The above equations are only applicable in cases where partial or whole volume of the normal tissue receives uniform dose. However, this is seldom the case. If the dose distribution is not uniform, then the above equations do not apply. In order to account for dose inhomogeneities, a method developed by Kutcher and Burman [96] to calculate an effective volume V_{eff} was used in the current study. This method transforms, by a series of steps as shown in Figure 4.2, an original non-uniform cumulative dose-volume histogram to a uniform one which contains an effective volume (V_{eff}) and a dose equal to the maximum dose (D_{max}) delivered to the organ. This transformed histogram is assumed to have the same complication probability as the original histogram.

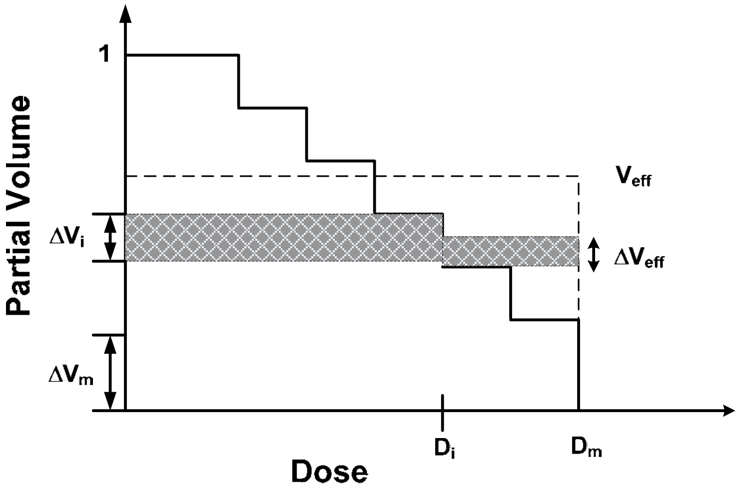

Figure 4.2. Step function representation of a dose volume histogram.

Each step of a histogram represented by a height ΔV_i and extension D_i ,in Figure 4.2, was assumed to satisfy a power law relationship so an effective volume $(\Delta V_{eff})_i$ for this step may be calculated using the following equation [96]:

$$(\Delta v_{eff})_i = \Delta V_i \left(\frac{D_i}{D_{\max}} \right)^{1/n} , \tag{4.9}$$

where n is a size (volume effect) parameter. The procedure, in equation 4.8, is repeated to every step of a cumulative DVH so that the effective volume for the entire DVH is given by [96]:

$$v_{eff} = \frac{1}{V_{ref}} \sum_i \Delta V_i \left(\frac{D_i}{D_{\max}} \right)^{1/n} , \tag{4.10}$$

where ΔV_i is the bin volume in the dose equivalent based differential DVH for a given irradiated normal tissue, V_{ref} is the reference volume (usually the whole volume), D_i is the equivalent dose which is given to the volume ΔV_i, and D_{max} is the maximum equivalent dose.

When the process of DVH reduction is completed, NTCP is calculated with the Lyman model using equation (4.5) and the equations following that as defined below:

$$NTCP = \frac{1}{\sqrt{2\pi}} \int_{-\infty}^{t} \exp\left(\frac{-x^2}{2} \right) dx, \tag{4.5}$$

$$t = \frac{D_{\max} - TD_{50}(v_{eff})}{m \cdot TD_{50}(v_{eff})}, \tag{4.11}$$

$$TD_{50}(v_{eff}) = TD_{50}(1) \times v_{eff}^{-n}, \tag{4.12}$$

The clinical endpoints examined in the current study are pericarditis, pneumonitis for the development of heart and lung complications respectively. The study also evaluated the cosmetic outcome of the MammoSite treatment, including fibrosis, telangiectasia, erythema and desquamation. The parameters used to calculate the NTCPs are listed in Table 4.2 [97-101].

Table 4.2. Summary of parameters used to calculate NTCP.

Organ	Endpoint	m	n	D_{50} (Gy)
Heart	Pericarditis	0.1	0.35	52.3
Lung	Pneumonitis	0.3	1	30.5
skin	Fibrosis	0.27	0.78	60
	Desquamation	0.27	0.78	55
	Telangiectasia	0.27	0.78	55
	Erythema	0.27	0.78	55

4.2.4.2 The relative seriality model

This model, proposed by Källman et al [102], is based on the Poisson model of cell survival to evaluate non-uniform irradiation of organs at risk from fractionated radiotherapy. Unlike Lyman-Kutcher model, this model also accounts for the structural architecture of functional subunits (FSUs) of the organ through the relative seriality parameter s. Organs consist of parallel and serial structures of FSUs. The response of the irradiated volume to radiation damage depends upon the structure of the organ. Parallel organs have a strong dependence on the volume irradiated considering the organ can maintain most of its function even when a large portion of its subunits are damaged. A parallel organ, such as lung and liver, has a relative seriality parameter s close to zero ($s \approx 0$). On the other hand, organs with serial organization have small dependency on the volume irradiated since every subunit can be vital for the organ function. A serial organ, such as bone marrow, has an *s* value close to 1 ($s \approx 1$).

According to the relative seriality model the NTCP, for inhomogeneous dose distribution, is defined as:

$$NTCP = \left\{ 1 - \prod_{i=1}^{M} \left[1 - \left(\frac{1}{1 + \left(D_{50} / D_i \right)^k} \right)^s \right]^{\Delta v_i} \right\}^{1/s}, \qquad (4.13)$$

where *M* is the number of sub-volumes in the equivalent dose based differential DVH. D_{50} is uniform dose that produces 50% probability complication rate and *k* is the slope of the response curve at D_{50} which is related to the parameter m through the relation ($k = 1.6 / m$) [102]. D_i is the equivalent dose, Δv_i ($= \Delta V_i / V_{ref}$) is the fractional irradiated sub-volume of an organ and *s* is the relative seriality parameter describing the structure of the organs. In the current study, the heart was considered to be a serial structure while the normal breast and the lung were modelled as parallel organs with *s* values equal to 1, 0.12 and 0.006 respectively [97, 99, 102]. The parameters for D_{50} were those listed in Table 4.2.

4.2.5 TCP calculations

The success of any radiotherapy modality depends on its ability to kill cells which compose the tumour [103]. The probability that no malignant cells are left in the tumour volume after irradiation is known as the tumour control probability (TCP). This probability is used to estimate the expected outcome of a given radiation treatment schedule. The literature provides various models for the TCP calculation, where the most commonly used is the Poisson model, which is based on the linear quadratic (LQ) formalism. In the current work, the tumour control probability was calculated for each balloon deformation treatment plan. The DVHs for the planning target volume were used to calculate the TCP. To compute the TCP, we employed the commonly used ‘Poisson model’, which is defined as follows [104]:

$$TCP = e^{-k \cdot S}, \qquad (4.14)$$

where k is the cell number of tumour clonogens and S is the surviving fraction. The linear quadratic is used to describe the cell killing by ionizing radiation [105]. Several investigators have extended the LQ model to include the effects of dose rate, repair of sublethal damage and clonogen proliferation [90, 106-108]. In LQ model, the surviving fraction S of cells irradiated to a total dose D within an effective treatment T is given by the following relation [90, 106-108]:

$$S = e^{-\{\alpha D(1+Gd/\alpha/\beta)\}-\gamma T}, \tag{4.15}$$

$$(BE_{ff}D)_i = D_i[1+Gd_i/\alpha/\beta], \tag{4.16}$$

where α and β are radiobiological parameters, d is the dose per fraction, G is the dose protraction factor which accounts for both the dose rate and repair of sublethal damage, γ is the effective tumour-cell repopulation rate [$\gamma = \ln(2)/T_d$ and T_d is the tumour-cell doubling time]. The surviving fraction was calculated for each bin of the $\mathrm{BE_{ff}D}$ based differential DVH using equations (4.15 and 4.16). The total physical dose D_i, corresponding to 10 treatment fractions in each sub-volume, was calculated by multiplying the dose d_i in each bin of the DVH for the PTV by a factor of ten.

For the MammoSite HDR brachytherapy, each fraction is delivered with approximately constant dose rate within short time, the protraction factor G in equation (4.15) was calculated by the following formula [93, 106]:

$$G = \frac{2}{n\mu T_f}\left[1-\frac{1}{\mu T_f}(1-e^{-\mu T_f})\right], \tag{4.17}$$

Here, n is the number of dose fractions, μ (= $\ln(2)/T_{½} = 0.69\ \mathrm{h}^{-1}$) is the repair rate of tumour cells and T_f is the dose delivery time (h). The values of the parameters used to calculate S and TCP for the MammoSite treatment are listed in Table 4.3 [109-112].

Table 4.3. Parameters selected to calculate TCP for MammoSite treatment plans.

Parameter	Value
k	200
α (Gy^{-1})	0.3
β (Gy^{-2})	0.03
T_d (day)	15
$T_{½}$ (h)	1

4.3 Results and discussion

4.3.1 Monte Carlo calculations

The impact of the source position on the dose distribution of the MammoSite was investigated using patient CT images. Uncertainty in the source position had a significant impact on the MammoSite treatment dose. A 1 mm deviation in the source location resulted in portions of the treated volume at the prescription distance (i.e. 1 cm from the balloon surface) receiving less than the prescribed dose by 7%. It also lead to other regions of the PTV receiving about 9% higher dose. A 2 mm source deviation resulted in portions of the treated volume receiving about 14% less than the prescribed dose whereas other regions of the treated volume received about 19% higher dose at the prescription point. This could expose the skin tissue to excessive dose especially in cases where the balloon-skin distance is at minimum. The distance from the balloon surface to the skin must be at least 5 mm to avoid significant skin toxicities.

The 2D dose distribution for the MammoSite plan with the source at the balloon centre is shown in Figure 4.3. The 2D dose matrix with the source at the centre of the balloon was subtracted from the 2D dose matrix with the source shifted by 4 mm, is shown in Figure 4.4. Our MammoSite treatment protocol allows for 4 mm balloon deformation. However, this study found that 4 mm balloon deformation produced about 40% extra dose to some portions of the PTV. This could lead to an excessive dose to the skin especially in cases where the balloon-skin distance is short. A 4 mm balloon deformation also resulted in underdosing of some portions of the target volume by 40%; this would have an impact on the treatment outcome particularly the tumour control.

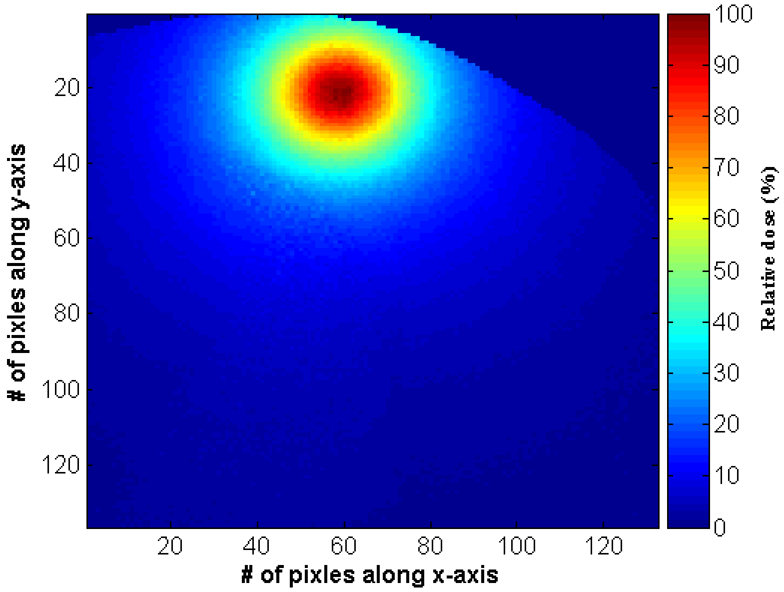

Figure 4.3. Dose distributions obtained for the ^{129}Ir source at the balloon centre.

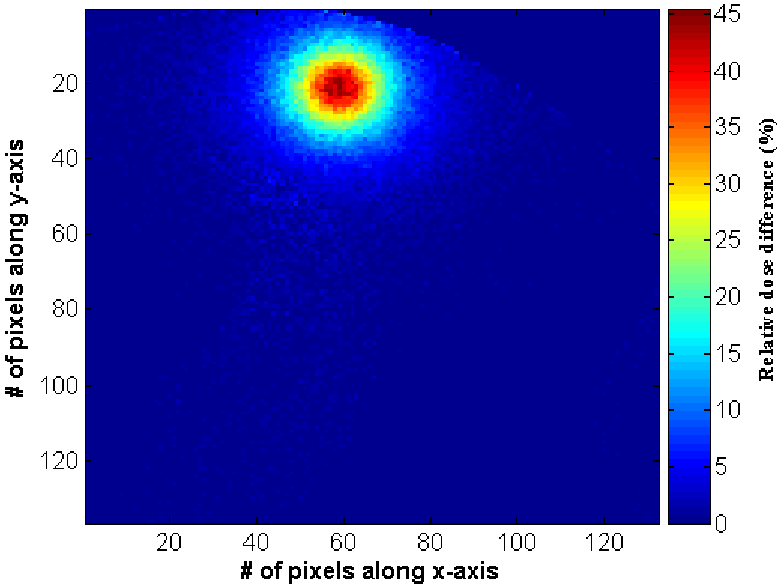

Figure 4.4. Dose difference map between dose distribution produced by the source positioned in the middle of the balloon and the source shifted by 4 mm.

Figure 4.5 illustrates the effect of the uncertainty in source position on the treatment dose at the prescription point. For each source shift, the dose was normalized to the reference plan with the source at the balloon centre. The zero shift point represents the dose calculated for the ^{192}Ir source situated in the centre of the balloon.

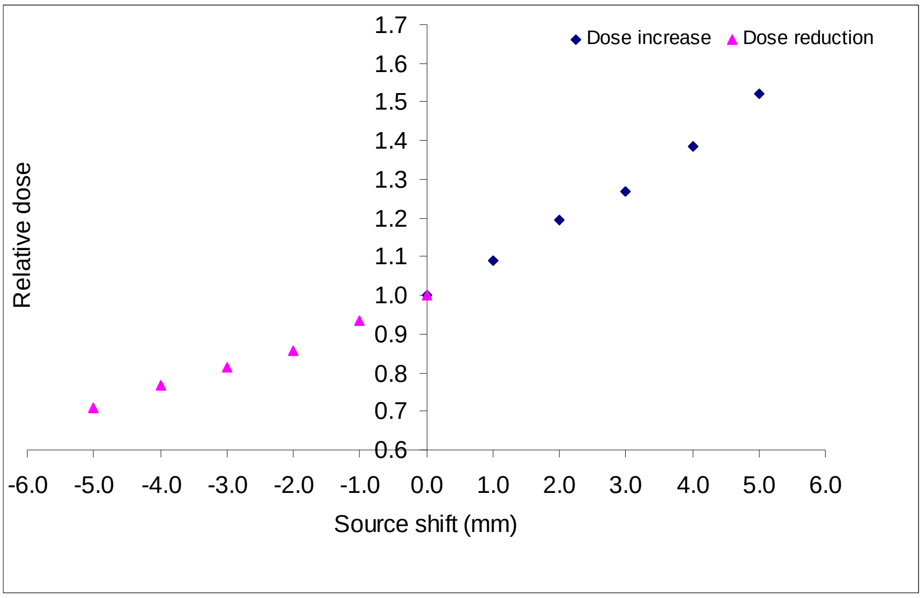

Figure 4.5. Source deviation produces (a) an increase in the dose in regions of the PTV and (b) reduction of the dose in other portions of the PTV in a plane 1.0 cm from the balloon surface. The uncertainty in Monte Carlo calculation was within 1.8%.

4.3.2 NTCP analysis

By applying the concepts of biological effective dose and relative effectiveness factor, the corresponding equivalent dose values, D_{eq}, were calculated for each bin of the differential DVHs of the critical organs. The first sets of calculations were done with the ^{192}Ir source placed at the centre of the balloon. Figure 4.6 shows the D_{eq} based differential dose volume histogram of the right lung. It is seen that only small portion of the lung volume would receive a dose of less than 10 Gy. Figure 4.7 shows the D_{eq} based differential dose volume histogram of the left lung. The left lung receives smaller dose value. Figure 4.8 shows the irradiated volume of the heart from the MammoSite treatment. Small portions of the heart would receive minimum dose. The D_{eq} based differential DVHs were then used for the calculations of the normal tissue complication probability.

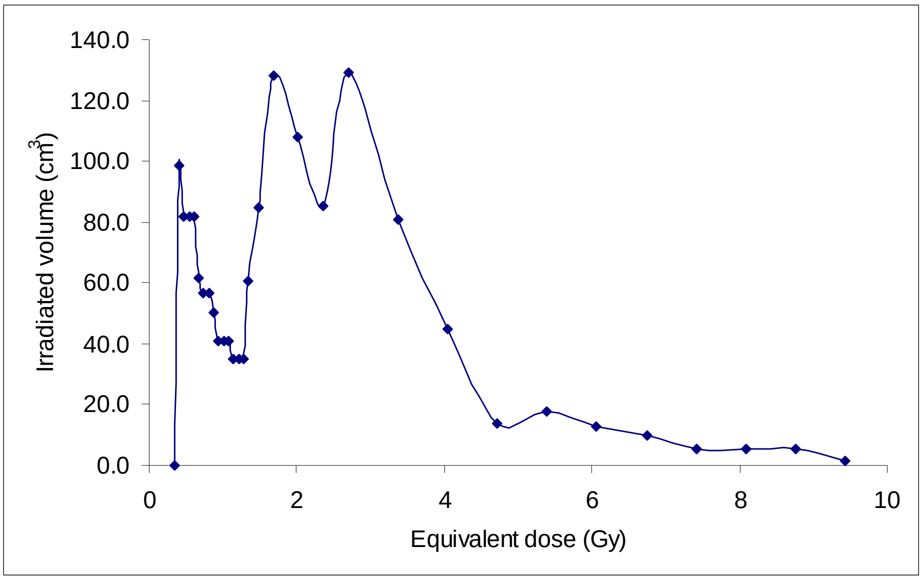

Figure 4.6. Differential equivalent dose based DVH of the right lung from MammoSite treatment plan with the ^{192}Ir source at the centre of the balloon, as calculated by Plato BPS (v 14.3.2, Nucletron).

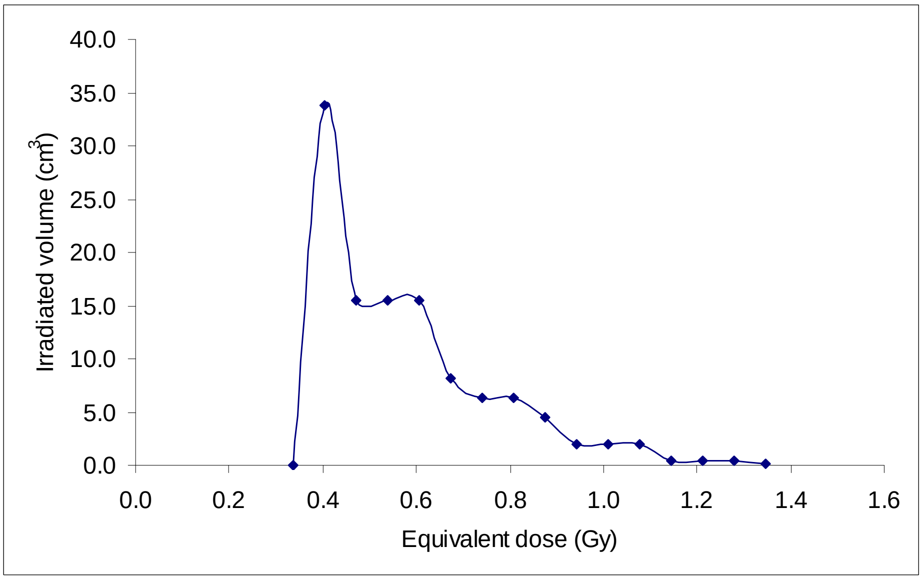

Figure 4.7. Differential equivalent dose based DVH of the left lung from MammoSite treatment plan with the ^{192}Ir source at the centre of the balloon, as calculated by Plato BPS (v 14.3.2, Nucletron).

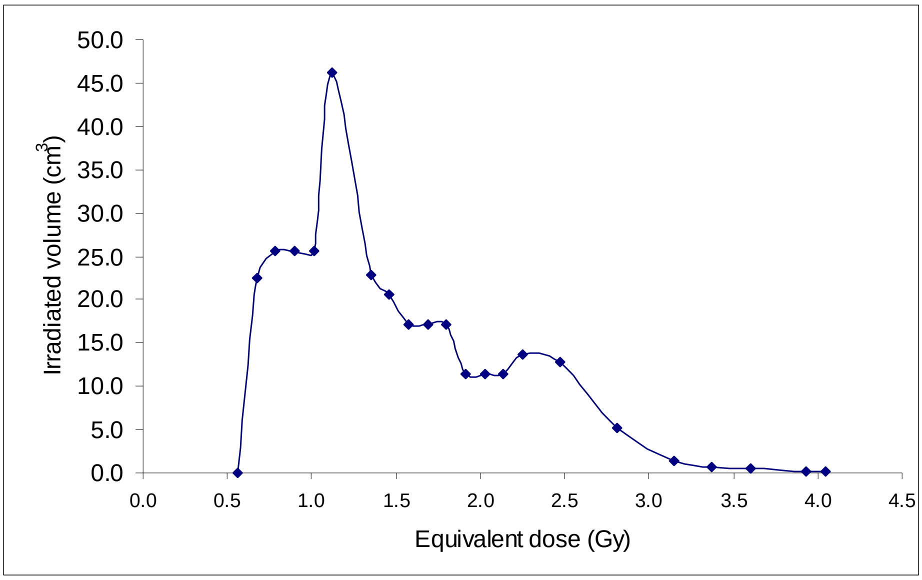

Figure 4.8. Differential equivalent dose based DVH of the heart from MammoSite treatment plan with the ^{192}Ir source at the centre of the balloon, as calculated by Plato BPS (v 14.3.2, Nucletron).

NTCPs for normal tissues were first calculated using Kutcher and Burman effective volume reduction scheme applied to the Lyman model and published tolerance parameters. The results of the Lyman model predicted no heart complications regardless of balloon deformation. The NTCP value for the lung, using the Lyman model, was low for balloon deformation treatment plans up to 4 mm as illustrated in Table 4.4. Both models were in agreement and predicted very little or no complications.

Table 4.4. Calculated NTCP values for the right lung with the Lyman model.

Balloon deformation (mm)	NTCP %
0	0.080 ± 0.003
1	0.084 ± 0.003
2	0.084 ± 0.003
3	0.084 ± 0.003
4	0.087 ± 0.003

The impact of balloon deformation on the probability of causing complications to the normal skin tissues depends on the location of the source inside the balloon and the volume receiving the dose. Skin complications are generally classified as early or late effects. Early skin effects include erythema and desquamation and they appear within a few weeks after treatment. Late skin complications include fibrosis and telangiectasia and they appear months or years following the treatment completion. By using the NTCP models, it is possible to predict these effects following the MammoSite treatment. These complications were assessed using DVHs generated from different MammoSite treatment balloon deformation plans.

The values of the parameters in Table 4.2 were fitted into the Lyman-Kutcher and relative seriality models. The NTCP was estimated to be 0.1%, 0.1%, 1.2% and 3.5% for skin complications including desquamation, erythema, telangiectasia and fibrosis respectively for the source positioned at balloon centre. A 4 mm balloon deformation caused nearly 0.6% increase in the NTCP for developing of tissue fibrosis. The NTCP for causing skin complications from the two models are listed in Tables 4.5 and 4.6.

Table 4.5. NTCP values for development of various skin complications using the Lyman model.

Balloon deformation (mm)	Fibrosis	Desquamation	Erythema	Telangiectasia
0	3.5	0.10	0.10	1.2 ± 0.5%
1	3.6	0.10	0.10	1.2 ± 0.5%
2	3.6	0.1	0.14	1.2 ± 0.5%
3	3.9	0.11	0.15	1.3 ± 0.5%
4	4.1	0.11	0.20	1.4 ± 0.5%

Table 4.6. NTCP values for tissue fibrosis with the relative seriality model.

Balloon deformation (mm)	NTCP %
0	1.8 ± 0.5%
1	1.9 ± 0.5%
2	2.1 ± 0.5%
3	2.3 ± 0.5%
4	2.6 ± 0.5%

4.3.3 TCP analysis

MammoSite treatment protocols prescribe the dose to a distance of 1.0 cm from the balloon surface of the spherical shape of the balloon with the source placed at the balloon centre. Under these conditions, any deformation in the balloon, the dose homogeneity in the PTV would be affected. This variation may have an impact on the TCP value. For example regions of the PTV will receive less than the prescribed dose. Also some portions of the PTV will receive more than the prescribed dose. The standard MammoSite plan, with the source accurately at the balloon centre, gave a TCP of 99%. The TCP results for various balloon deformations are illustrated in Figure 4.9. The study found that 1 mm, 2 mm, 3 mm and 4 mm balloon deformation reduced the TCP by 4%, 8%, 15% and 24% respectively.

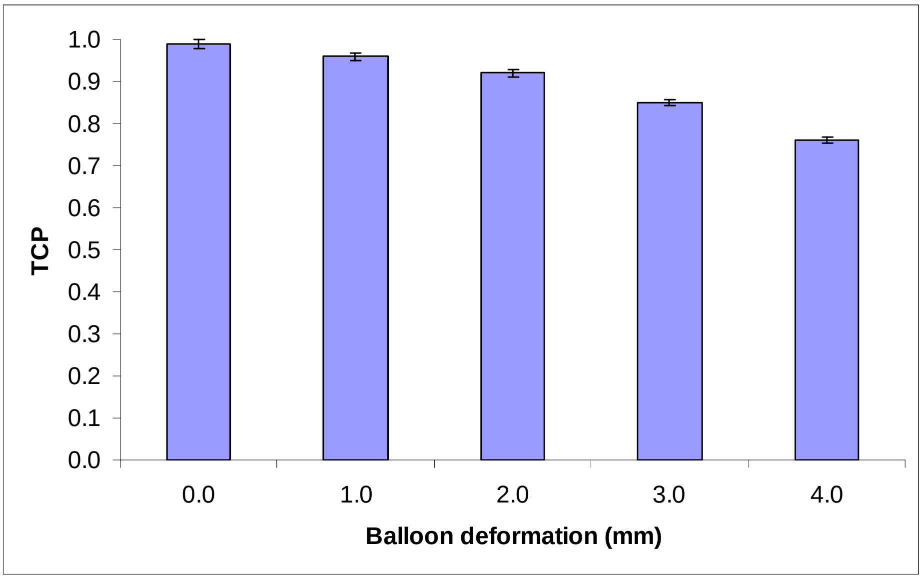

Figure 4.9. The impact of the balloon deformation on TCP.

The size of the PTV was also affected due to the shape of the isodose distribution, see Table 4.7. The original PTV was 104.5 cc whereas 1 mm and 2 mm balloon deformation reduced the PTV by factors of 0.97 and 0.93 respectively. A 3 mm and 4 mm balloon deformation significantly reduced the PTV to be 91 cc and 85.1 cc respectively. The balloon deformation affected the percentage of the PTV volume that receives 100% of the prescription dose (%$V_{100\%}$).

Table 4.7. Variation in the PTV and dose due to balloon deformation.

Balloon deformation (mm)	PTV (cc)	% $V_{100\%}$	TCP (%)
0	104.5	90.2	99
1	101.5	87.4	96
2	97.3	83.7	92
3	90.9	78.8	85
4	85.1	74.2	76

This study was done for one patient only; the results may change for different patients where the balloon position is different relative to the normal tissues.

4.4 Conclusions

The MammoSite technique treats only a portion of the breast for relatively small number of fractions with a high dose per fraction. This method requires higher accuracy of source position and symmetrical balloon shape. The spherical dose distribution within the surrounding tissue of the MammoSite technique is to ensure that the PTV receives the prescribed dose while protecting the normal healthy organs from excessive or unnecessary dose. Perturbations in source location would have an impact on the probability of causing complications to the normal breast tissues including the skin depending on the location of the source inside the balloon and the volume receiving the dose.

The Lyman and relative seriality models were employed to estimate the normal tissues complications associated with the MammoSite dose distributions. The NTCP calculations are based on heart, lung and normal breast tissue including skin DVHs which were generated by the brachtherapy treatment planning system. This study gives low probabilities for developing heart and lung complications. Based on this study, the examined NTCP models and particularly the Lyman model in the case of breast radiotherapy are useful in predicting complication risks to the heart, lung and skin following MammoSite brachytherapy.

Monte Carlo calculations using EGSnrc showed that a high deviation in the source position would lead at the greatest risk of reducing the dose to regions of the PTV. A deviation of the source by 1 mm caused approximately 7% dose reduction in the treated target volume at 1 cm from the balloon surface whereas 2 mm source deviation caused about 14% dose reduction at the same point. A 4 mm source deviation produced underdosing of some portions of the PTV by 40% leading to poor treatment outcomes. Furthermore, 4 mm uncertainty in source deviation leads to overdosing of regions of the PTV by about 40%. This results to an excessive dose to the skin and increases the probability of skin complications.

This study has demonstrated the importance of keeping the spherical shape of the balloon and accurate placement of the brachytherapy source at the balloon centre. Balloon deformation and incorrect source position had significant effect on the prescribed dose within the treated volume. A 4 mm balloon deformation resulted in reduction of the tumour control probability by 24%. The discussed case represents the extreme case. Over the course of treatment, the uncertainties in the balloon deformation and source position can average out to some extent and reduce the overall impact.

In summary, source position is an important issue in the MammoSite procedure irrespective of the balloon-skin distance. The current study suggests that the MammoSite treatment protocols should allow for a balloon deformation by ≤ 2 mm and a maximum source deviation of ≤ 1 mm.

Chapter 5

Uncertainty in contrast concentration inside the MammoSite balloon: Monte Carlo simulations and thermoluminescent dosimetry measurements

5. Introduction

During treatment the MammoSite balloon is placed into the tumour resection cavity and inflated with a mixture of saline and radiographic contrast agent to a size that fills the cavity. A high dose rate ^{192}Ir source is driven in to the balloon centre using a remote afterloader to deliver the prescribed dose at a plane 1 cm away from the balloon surface. Chapter four dealt with source position and balloon deformation uncertainties. This chapter investigates the impact of the concentration of the contrast medium inside the balloon on the dose distribution. This parameter also needs to be investigated as it may have an impact on the treatment efficacy.

In order to enhance image quality and balloon visibility for treatment planning procedures contrast medium is used inside the balloon [10, 14, 18]. Contrast materials typically contain elements with high atomic number (for example, iodine with Z = 53), so the balloon content can no longer be considered tissue or water equivalent. Most of the currently available treatment planning systems for brachytherapy estimate the dose in a patient using the pre-calculated dose matrices derived from the ^{192}Ir source positioned in a water phantom [37] and do not take variations in attenuation into due to inhomogeneities account. The radiographic contrast medium in the balloon represents an uncertainty parameter that alters the dose distributions calculated by the treatment planning system.

Several numbers of studies investigated the dose perturbation extent from the contrast medium within the balloon using Monte Carlo simulations and measurements [11, 12, 84, 113]. Cheng et al [84] performed Monte Carlo simulations for the MammoSite balloon using DOSRZnrc user code. as mentioned in Chapter 3, the DOSRZnrc [86] calculates the dose distribution in a cylindrical geometry. In DOSRZnrc code, the cylindrical phantom was divided into small shells to represent the MammoSite balloon and the dose distribution was calculated with the ^{192}Ir source placed at the centre of the MammoSite balloon. However, the DOSRZnrc Monte Carlo code can not be used to perform dose calculation using patient CT dataset containing the MammoSite balloon. The published experimental measurements were also performed with the MammoSite balloon in a water tank and dose measurements were carried out with the use of an ion-chamber [12]. The size of the chamber would lead to averaging of the dose gradient and the water tank would not represent patient geometry.

The purpose of the current work is to investigate the extent of the dose perturbation for various concentrations of the contrast medium in a MammoSite balloon using Monte Carlo simulations and thermoluminescent dosimetry. This Chapter is divided into two parts. In part one, the Monte Carlo simulation was performed using computed tomography (CT) images of the MammoSite balloon placed in a designed breast tissue equivalent phantom. In part two, the breast phantom was used for thermoluminescent dosimetry measurements. In the current study, the thermoluminescent dosimeters (TLDs) had small thickness (0.38 mm) reducing the effect of averaging of the dose around the source and the measurements were carried out with the use of tissue equivalent breast phantom which resembled patient geometry and provided realistic scatter conditions.

Part one: Monte Carlo simulations

5.1.1. Introduction

In this part, the Monte Carlo simulations, done for investigating the impact of various contrast concentrations inside the MammoSite balloon in the dose distribution in the breast, are discussed. When the balloon is filled with saline only, it is difficult to visualize it and make a treatment plan. It is therefore necessary to add contrast medium inside the MammoSite balloon. Figure 5.1 shows the importance of adding contrast solution inside the balloon as it helps visualizing the balloon and hence contour the planning target volume. The MammoSite balloon, filled with saline only, combination of saline and various contrast concentrations, was placed inside a designed tissue equivalent breast phantom that was attached to a Rando$^{®}$ anthropomorphic phantom. The breast phantom was then scanned and the CT images were imported the EGSnrc Monte Carlo system code.

In the Monte Carlo simulation, the modelled ^{192}Ir source was placed at the centre of the MammoSite balloon. The DOSXYZnrc was used to calculate the dose distribution using the CT dataset of the breast phantom.

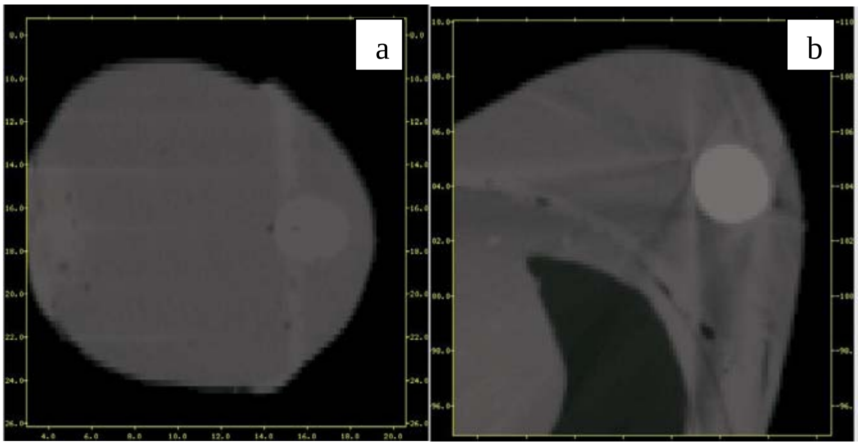

Figure 5.1. Balloon inside a phantom filled with (a) saline only, (b) saline and contrast.

5.1.2 Materials and methods

5.1.2.1 Design of tissue equivalent breast phantom

In the current study, a breast phantom was constructed in-house from near tissue equivalent materials (50% paraffin, 50% bees wax, and relative density of 0.926) and was used for investigation of perturbation effects of different contrast concentrations in the MammoSite balloon on the dose distribution in the breast. The relative density of phantom material was of similar density to the breast tissue (the relative density of the breast is 0.987). A schematics of the breast phantom is shown in Figure 5.2. The phantom should simulate same scatter geometry as used in MammoSite treatment. The phantom was split into two halves along the central axis to allow for placement of the MammoSite balloon and thermoluminescent dosimeters (TLDs). Holes were drilled in the breast phantom to hold the TLDs at different distances from the balloon surface. The TLDs provided experimental measurement of the dose at various depths from the balloon surface along the radial axis. The TLD measurements will be discussed in detail in part two of the current chapter.

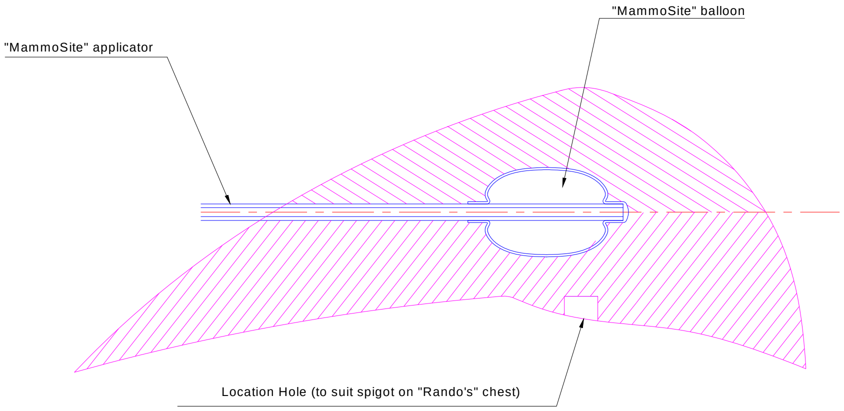

Figure 5.2. Diagram of the breast phantom design.

5.1.2.2 Contrast medium within the MammoSite balloon

In all investigations, a clinical MammoSite balloon of 4 cm in diameter was used. The MammoSite balloon was placed into the designed breast phantom and first filled with saline only to the desired volume and the two halves of the phantom were joined together. The breast phantom was then attached to the Rando® anthropomorphic phantom as shown in Figure 5.3. Computed tomography images of the breast phantom were then obtained from a CT scanner (Philips Medical Systems Ltd, Stevenage, UK) using axial slices of 3 mm thickness, see Figure 5.4.

The saline in the balloon was then replaced with an equal volume of a 100% contrast solution and a CT scan was acquired. The contrast medium used in this investigation is Ultravist 370 (Bayer Health Care Pharmaceutical Inc., Germany) which is a water-soluble radiopaque medium. It has a molecular composition of $C_{18}H_{24}I_3N_3O_8$ and a molecular weight of 790.91 of which 48.13% iodine content by weight and density of 1.409 g cm^{-3}. The filling and scanning process was repeated for the balloon filled with saline and 50% of radiographic contrast concentration and for the balloon filled with saline and 15% radiographic contrast concentration. The CT datasets were used in Monte Carlo simulations. The contrast solutions were carefully prepared and kept in a dark environment to avoid re-crystallization.

Figure 5.3. The inflated balloon placed inside a designed breast tissue equivalent phantom which is attached to the Rando® anthropomorphic phantom.

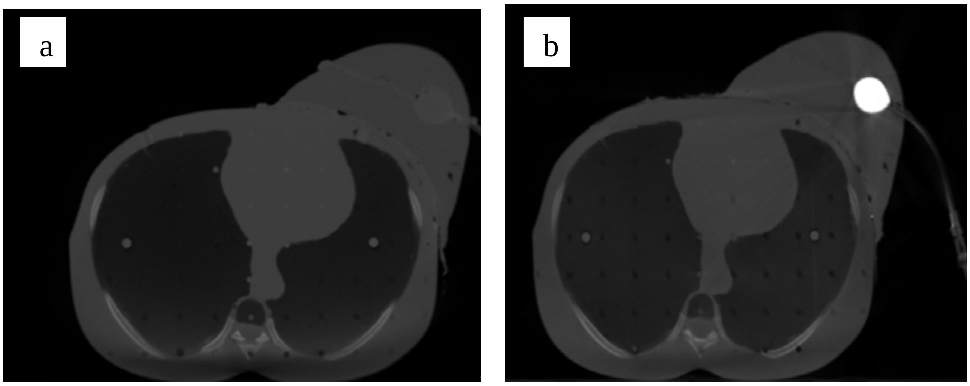

Figure 5.4. CT images of the breast phantom obtained from CT scanner (a) saline only, (b) contrast only.

5.1.2.3 Monte Carlo simulation

The CT images of the designed breast phantom, with the MammoSite balloon inside the phantom as described in section 5.1.2.2, were imported to EGSnrc Monte Carlo code, for conversion into a readable format required by DOSXYZnrc for dose calculation. The CT slices were converted into a specific format ,*.egsphant, using CTCREATE user code [38]. This code reads in a CT datasets and assigns a material density to each volume element (voxel). The CT phantom created by the CTCREATE code contains information such as tissue materials, CT number, upper and lower density, the dimensions of the CT phantom (X, Y, Z), voxel sizes and Monte Carlo transport parameters.

The following materials were used: air, lung, breast tissue, saline (water) and various contrast concentrations. The air, lung, water, and breast tissue materials were modelled according to the ICRU Report 44 [114]. The radiographic contrast was modelled by specifying the percentage weight of each component and the physical density of the contrast as shown in Table 5.1. The material data were modelled using the EGSnrc Monte Carlo user code EGS-GUI [115].

Table 5.1. Compositions and densities of the simulated contrast solutions.

% contrast	% carbon	% hydrogen	% iodine	% nitrogen	% oxygen	Density (g/cc)
15	4.16	9.97	7.22	0.80	77.92	1.06
50	13.66	7.12	24.06	2.66	52.49	1.20
100	27.31	3.06	48.13	5.31	16.18	1.41

In the Monte Carlo simulations, electrons and photons were tracked until their energies reach the predefined cut-off values ECUT and PCUT, respectively. These Monte Carlo parameters were set to AE = ECUT = 0.521 MeV, AP = PCUT = 0.06 MeV. In each simulation, the modelled ^{192}Ir source was placed at the centre of the MammoSite balloon (4 cm in diameter) with its axis aligned with the balloon axis. The voxel size of the 3-dimensional scoring geometry was 1.5 mm^3. Up to 4 x 10^7 particles were tracked for each simulation resulting in statistical uncertainty of 1.8-2% at 1.0 cm from the balloon surface. This resulted in a CPU running time between 85-119 hours for the different runs. At the end of the simulation runs, the EGSnrc user code STATDOSE [57] was used to extract the dose distributions in the CT datasets at various distances from the balloon surface. To determine the extent of dose perturbation for different contrast concentrations (0%, 100%, 50%, 15% by volume) the dose was normalized to that with the MammoSite balloon filled with saline only.

5.1.3 Results

DOSXYZnrc simulations produce a 3D dose distribution output files. These data files were used for investigation of the impact of the presence of various contrast concentrations inside the balloon on the dose distribution at the prescription point. The dose was normalized to the dose at 1 cm from the balloon surface (the prescription point). Figure 5.1.5 compares the relative dose as a function of distance between the MammoSite balloon filled with saline only and that filled with contrast only. In clinical situation, the balloon is never filled with 100% contrast concentrations, it is used here for the purpose of illustrating how the 100% contrast could cause reduction in the prescribed dose. As seen on Figure 5.5 the 100% contrast caused 10% reduction at the prescription point as compared with the balloon filled with saline.

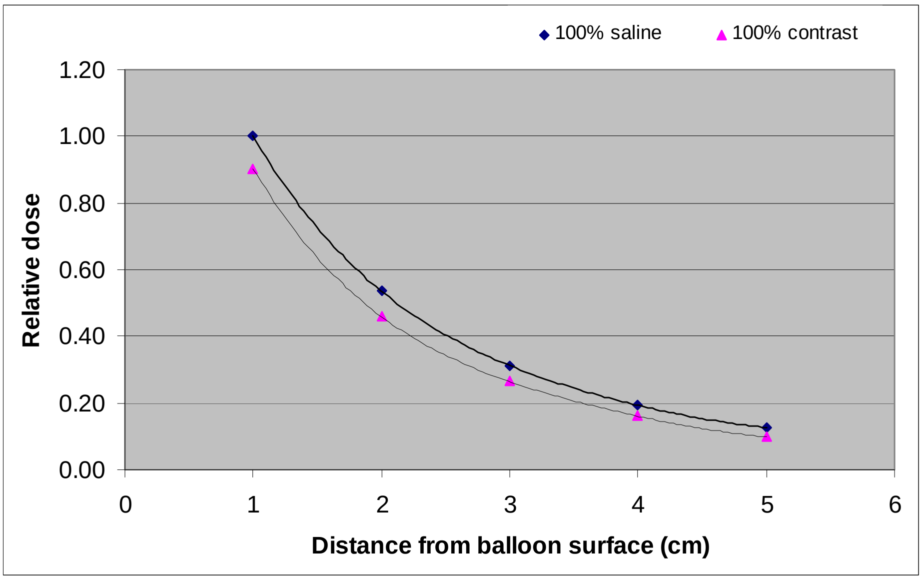

Figure 5.5. Comparison of the dose fall-off as a function of distance for the MammoSite balloon filled with saline only to that filled with contrast only, starting at 1 cm from balloon surface. The uncertainty in Monte Carlo calculation was within 1.8% at 1 cm from the balloon surface and slightly more than 2% else where.

Figure 5.6 compares the relative dose as a function of distance from the balloon surface for balloon filled with saline only and that filled with 50% saline and 50% contrast. The 50% contrast concentration inside the balloon caused about 5% dose reduction at the prescription point.

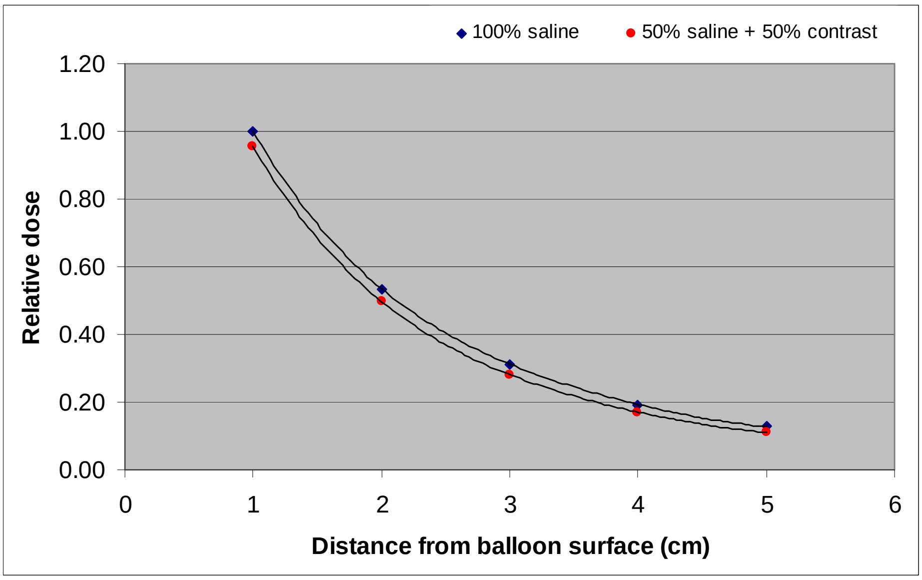

Figure 5.6. Comparison of the dose fall-off as a function of distance between the MammoSite balloon filled with saline only to that filled with 50% saline plus 50% contrast, starting at 1 cm from the balloon surface. The uncertainty in Monte Carlo calculation was within 1.8% at 1 cm from the balloon surface and slightly more than 2% else where.

Figure 5.7 compares the relative dose as a function of distance from the balloon surface for balloon filled with saline only and that filled with 85% saline and 15% contrast. It can be seen that the 15% contrast concentration inside the balloon caused about 2% dose reduction at the prescription point.

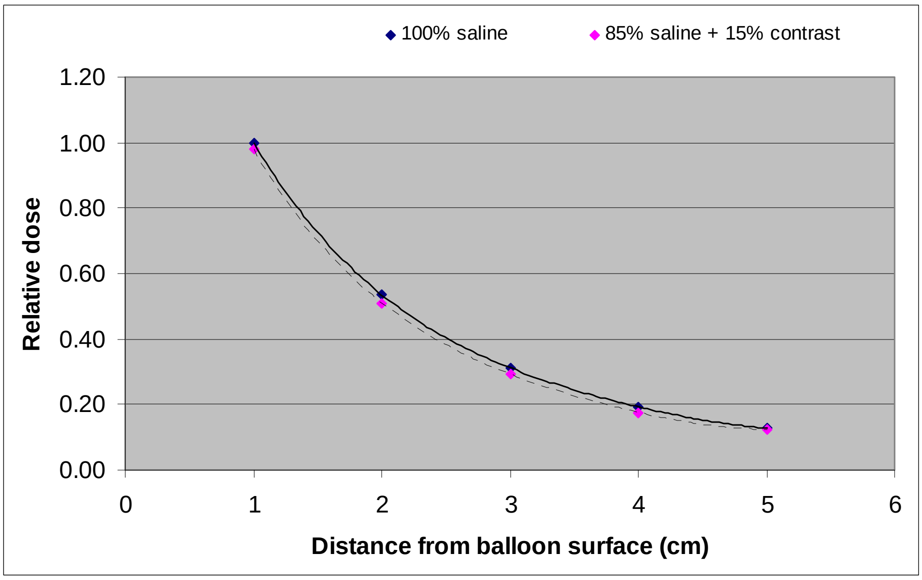

Figure 5.7. Comparison of the dose fall-off as a function of distance between the MammoSite balloon filled with saline only to that filled with 85% saline plus 15% contrast, starting at 1 cm from the balloon surface. The uncertainty in Monte Carlo calculation was within 1.8% at 1 cm from the balloon surface and slightly more than 2% else where.

A Matlab (version 7.0, The Math Works, Inc.) in house code was used to extract 2D dose distributions matrices from the Monte Carlo 3D dose distribution output files. The 2D dose distribution for the balloon filled with saline was extracted at a plane 1 cm from the balloon surface. Similarly, 2D dose matrix was extracted for the balloon filled with contrast only at the same plane. The dose distribution was scaled to the same point. Figure 5.8 shows 2D dose matrix at 1.0 cm plane from the surface of the balloon. The contrast inside the balloon resulted in 10% dose reduction at 1 cm (prescription point) from the balloon surface.

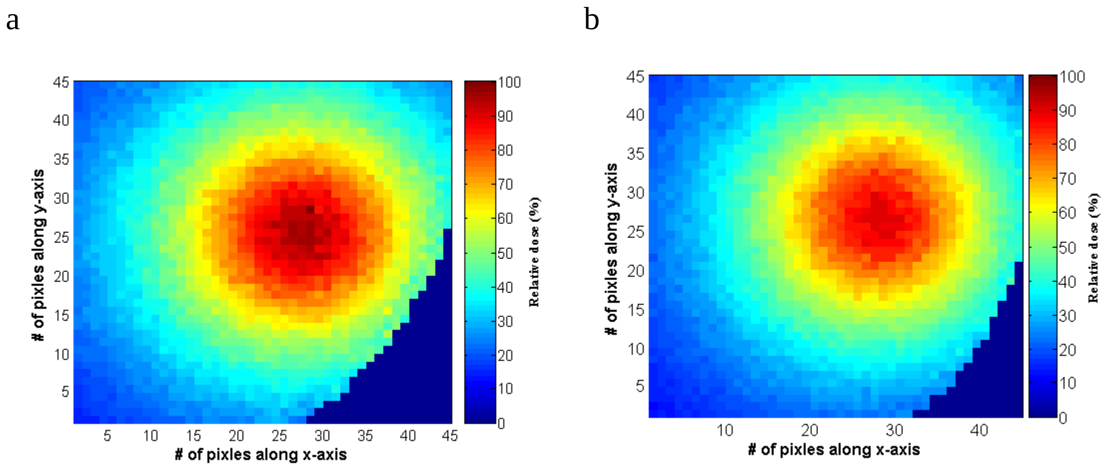

Figure 5.8. Monte Carlo 2 D dose distribution for balloon filled with (a) saline only and (b) contrast only.

5.1.4 Discussion & conclusion

The radiation dose in the breast treatment is affected by the amount of contrast medium in the MammoSite balloon. The EGSnrc Monte Carlo code was used to investigate this impact at various distances from the balloon surface using CT images of breast phantom that resembles patient geometry. The Monte Carlo simulation was performed for clinical balloon of 4 cm diameter and contrast concentrations of 0%, 15%, 50% and 100% by volume. For the MammoSite brachytherapy, other uncertainty including the source positioning and balloon deformation, discussed in chapter four, contribute to the dose reduction at the prescription point. The contrast concentration is also a contributing factor to the overall uncertainty in the MammoSite bracytherapy method. This uncertainty would have a significant effect on the prescribed dose especially for larger surgical cavities.

The results of the current investigation were compared with other studies. Kassas et al [11] reported 2.4% dose reduction at 1 cm from the balloon, 4 cm diameter, due to 15% contrast concentration in the balloon relative to saline. Kirk et al [12] reported a dose reduction factor of 0.954 and 0.919 at the prescription point for contrast concentrations of 50% and 100% respectively. Our results showed that 100%, 50% and 15% contrast concentrations reduced the dose at the prescription point by 10%, 5% and 2% respectively relative to the dose calculated with the balloon filled with saline (water) only. As opposed to other studies our Monte Carlo results will be validated with measurements performed with TLDs in a breast phantom.

In conclusion, the contrast medium inside the MammoSite balloon caused reduction on the dose distributions at the prescription point. The amount of dose reduction depended on the concentration of contrast inside the balloon. The dose perturbation was larger for higher contrast concentration.

Part two: Thermoluminescent dosimetry measurements

5.2.1 Introduction

This section describes in details the experimental measurements carried out with thermoluminescent dosimeters to quantify the dose reduction in the breast resulting from the contrast medium inside the MammoSite balloon. In the current study, the thermoluminescent dosimeters (TLDs-100 chips) of small thickness (0.38 mm) were used to reduce the effect of averaging of the dose along the dose gradient. The measurements were performed in a tissue equivalent breast phantom resembles patient geometry and providing realistic scatter conditions.

5.2.1.1 TLD theory

The principles of thermoluminescent dosimetry have been described extensively in the literature. Thermoluminescence (TL) is the emission of light during heating of a crystal sample, previously excited by radiation. The TL material absorbs energy during exposure to ionizing radiation and stores this energy until heated. In the TL material the electrons occupy the valence bands, which are separated from the conduction band by the forbidden band, see figure 5.9. When ionizing radiation is absorbed in such a crystal, electrons are transferred from the valence band to the conduction band. These free electrons diffuse through the crystal until they reach traps in the crystal. Electrons can be released from these traps by heating. When the material is heated the electron obtains enough energy to get out of the trap and return to the ground state with the emission of light. The phenomenon is called thermoluminescence [116]. The emitted light in the thermoluminescence process as a function of temperature is called the glow curve. It consists from several peaks corresponding to different trapped energy levels.

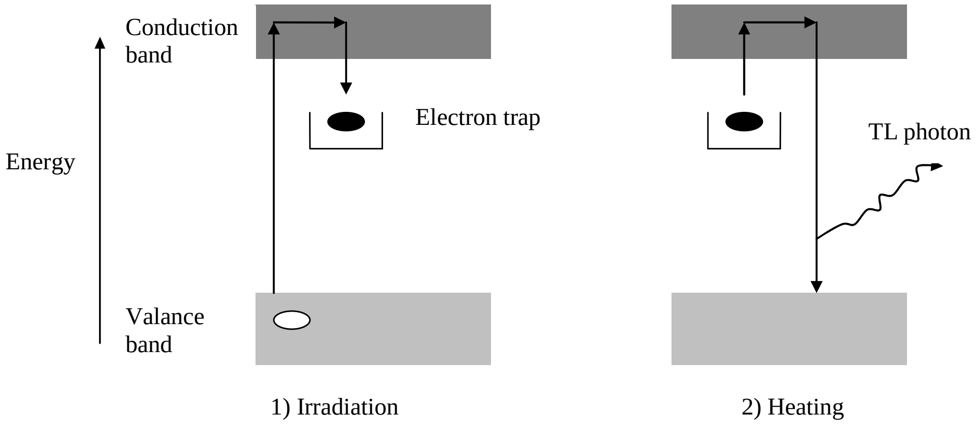

Figure 5.9. Energy level diagram of the TLD process.

5.2.2 Materials and methods

5.2.2.1 Dose measurements using TLDs

TLD-100 chips were used to measure the dose fall-off at various distances from the balloon surface for several contrast concentrations within the MammoSite balloon. The measurements were carried out in the breast phantom described in part one. Before using the TLDs for dose measurements, their individual sensitivity correction factors were determined by giving them a uniform dose from a linear accelerator available at our radiotherapy facility. TLD measurements are discussed in more detail in the following sections.

5.2.2.2 LiF TLD

The current investigation of the extent of the dose perturbation for various concentrations of the contrast medium in a MammoSite balloon was performed using LiF:Mg,Ti TLD-100 chips (Krakow, Poland). These TLDs are composed of lithium fluoride (LiF) doped with magnesium (Mg) and titanium (Ti). They have several useful properties such as their effective atomic number ($Z_{eff,\ LiF}$) is equal to 8.2, which is close to the effective atomic number of soft tissue ($Z_{eff,\ tissue}$) of 7.4. This makes this type of TLD suitable for clinical radiotherapy as it is nearly tissue equivalent. It is also insensitive to light and the thermal fading is small (<5% in 1 year) and dose rate independent. The dimensions of the TLD-100 chips were approximately 3.2 mm x 3.2 mm x 0.38 mm. The small thickness of the TLDs allows for high dose resolution measurements in the direction of rapid dose gradient typical for brachytherapy dose distributions.

5.2.2.3 TLD Annealing Cycle

In the current study 50 TLD chips were each labelled on one side with identification number for sorting purposes. They were kept in an aluminium tray that was used for annealing them in the TLD annealing oven (Victoreen, USA). The TL dosimeters were carefully handled with vacuum tweezers to avoid contamination and scratching the surface of the chips. All TLD-100 chips were annealed in the TLD annealing oven before irradiation. The annealing was performed to erase any previous irradiation effects and to achieve reproducible results [117]. In this work, th the following procedure was used. TLDs were annealed at 400 ^{0}C for 1 hour and then they were cooled between aluminium blocks for 2 hours, then annealed for 20 hours at 80 ^{0}C and cooled between aluminium blocks. This annealing procedure was done before each irradiation. Figure 5.10 shows the annealing oven and aluminium blocks which were used for storing and cooling of the TLDs.

Figure 5.10. Oven and aluminium blocks that were used for annealing and cooling of TLDs respectively.

5.2.2.4 Description of the TLD reader

The dose stored in the thermoluminescent material was measured using a TLD reader, see Figure 5.11. The reader is a PC-driven instrument and capable of reading one TL chip per loading. The arrangement for measuring the thermoluminescence output is shown schematically in Figure 5.12. During the reading cycle, the TLD chip was positioned onto a reading tray. Using a computer program interfaced with the TLD reader, each TLD was heated from 50 ^{0}C to 300 ^{0}C under nitrogen gas. While the crystal was being heated from 50 ^{0}C to 300 ^{0}C, a photomultiplier tube (PMT) inside the TLD reader recorded the current versus temperature. This produced a glow curve. After the temperature range was swept, the program automatically integrated the glow curve to obtain the total charge acquired throughout the selected temperature range.

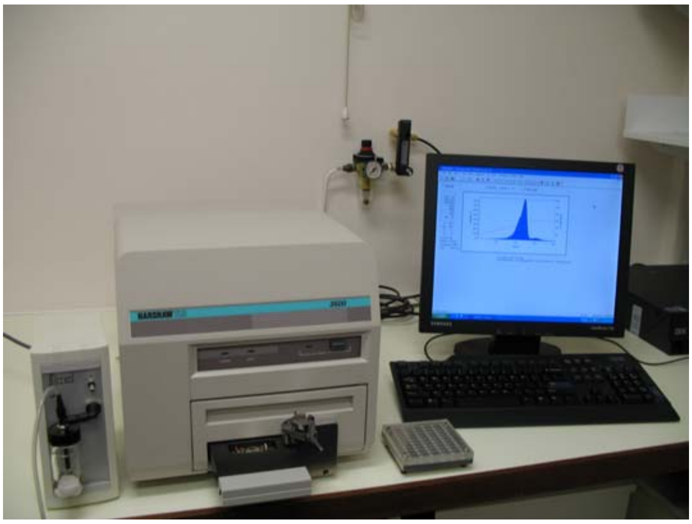

Figure 5.11. Harshaw 3500 (Harshaw / Bicron, USA) automatic TLD reader.

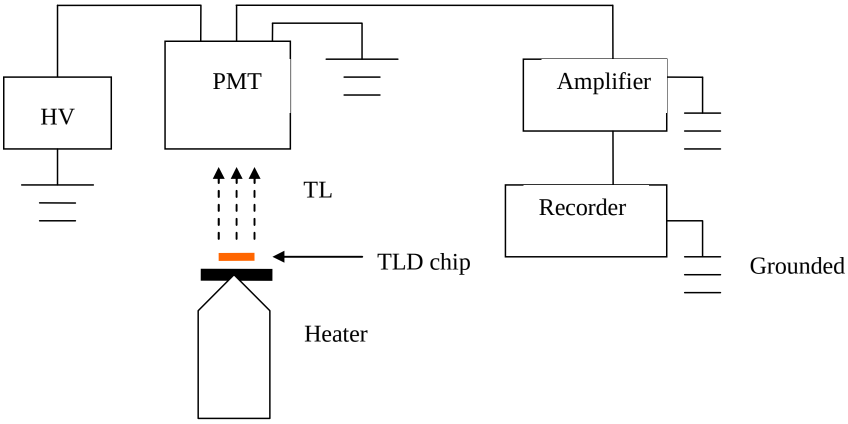

Figure 5.12. Schematic diagram of a TLD reader.

5.2.2.5 Determination of sensitivity correction factor

The sensitivity correction factor (SCF) compensates for the variation in sensitivity among the TLDs irradiated to the same dose. This factor accounts for the variation in the amount of active material in each LiF TLD chip. It also takes into consideration the small difference, between the physical sizes of the TLDs chips. In order to account for individual response differences of each TLD, their individual sensitivity correction factors had to be measured first. The experimental procedure for measuring the SCF for each TLD is described below.

The TL dosimeters were exposed lying on the surface of a 25.5 x 25.5 cm, and a 1 cm thick solid water phantom with holes cut in to fit a single TLD chip each. The holes were assigned identification numbers for sorting purposes. A build up layer of solid water of 1.3 cm thickness was used to place the chips at depth of maximum dose for a 6 MV photon beam. Approximately 11 cm plastic material was used underneath the TLDs to provide backscatter. All TLDs were irradiated to a uniform dose of 1 Gy using a 6 MV photon beam from a Varian iX linear accelerator. This dose was given at a depth of maximum dose (1.3 cm) using a 10 cm x 10 cm field size at a source-to-surface distance (SSD) of 100 cm. Figure 5.13 shows the corresponding experimental setup.

Figure 5.13. Experimental setup for the measurement of the sensitivity correction factor of the LiF TLD-100 chips.

The TLDs were read after a 24 hour waiting period. This waiting time assured that any residual TL from the short half-life peaks would have no significant contribution to the signal [118, 119]. The TLD signal was read out in a Harshaw Model 3500 Automatic TL reader. The TL reader was operated using a voltage of 897/899 V to its photomultiplier tube and temperature between 50^0C to 300^0C at a constant heating rate of 10^0C.s^{-1}. Nitrogen gas flow was used in the reader during the TL readouts. The purpose of the nitrogen gas is to eliminate unwanted oxygen induced TL signals [120]. When reading the TLDs, it is important to place the dosimeters on the heating planchet with the side facing the radiation beam towards the photomultiplier tube. This is to obtain a reproducible reading setup. When a TLD chip is read, a total charge, in micro-coulomb (μC) or nano-coulomb (nC), is measured by the photomultiplier tube. During every reading cycle, several un-irradiated chips were used for background subtraction. After readout, all TLD chips were again subjected to the above annealing procedure. The whole set of the chips underwent three cycles of annealing, irradiation and readout. The TLD readings were transferred to an Excel spreadsheet for subsequent analysis.

To determine the sensitivity correction factor for a TLD chip, an average readout, *AVRi*, was calculated from the readings, *TLDn(Ri)*, corrected for background of all the TLD chips after each irradiation, *i*. A mean readout, *MR*, was obtained from the three average readouts (after three irradiation cycles of all TLDs). A normalized readout, *MNRn*, for a TLD chip for each irradiation was obtained using the average readout for the whole batch, *AVRi*, for a given irradiation, *i*, and the mean readout determined from all irradiations and all TLDs. Table 5.2 presents a clarification of the determination of SCF.

Table 5.2. An illustration of TLD irradiation readout for obtaining SCF of a TLD chip.

TLD #	**1st Irradiation readout**	**Normalized readout**	**2nd Irradiation readout**	**Normalized readout**	**3rd Irradiation readout**	**Normalized readout**	**Mean of normalized readout**
TLD1	TLD1 (R1)	TLD1 (NR1)	TLD1 (R2)	TLD1 (NR2)	TLD1 (R3)	TLD1 (NR3)	MNR1
TLD2	TLD2 (R1)	TLD2 (NR1)	TLD2 (R2)	TLD2 (NR2)	TLD2 (R3)	TLD2 (NR3)	MNR2
TLD3	TLD3 (R1)	TLD3 (NR1)	TLD3 (R2)	TLD3 (NR2)	TLD3 (R3)	TLD3 (NR3)	MNR3
TLD4	TLD4 (R1)	TLD4 (NR1)	TLD4 (R2)	TLD4 (NR2)	TLD4 (R3)	TLD4 (NR3)	MNR4
….	….	….	….	….	….	….	….
….	….	….	….	….	….	….	….
TLDn	TLDn (R1)	TLDn(NR1)	TLDn (R2)	TLDn(NR2)	TLDn (R3)	TLDn(NR3)	MNRn
AVRi	AVR1		AVR2		AVR3		
Mean Readout	**MR = (AVR1+AVR2+AVR3)/3**						

Table 5.2 is explained further. The average readout of all TLDs after first irradiation, *AVR1*, is expressed as follows:

$$\mathrm{AVR1} = [\mathrm{TLD1(R1)} + \mathrm{TLD2(R1)} + \ldots .. + \mathrm{TLDn(R1)}]/n \qquad (5.1)$$

Where *n* is equal to 50 TLDs.

The mean readout, *MR*, for the 50 TLDs after three irradiation cycles is determined as follows:

$$\mathrm{MR} = (\mathrm{AVR1} + \mathrm{AVR2} + \mathrm{AVR3})/3 \qquad (5.2)$$

The normalized readout for one TLDn, *MNRn*, for a single irradiation cycle, *i*, is calculated as follows:

$$\text{MNRn} = (\text{TLDn(Ri)/AVRi}) \text{ x MR} \tag{5.3}$$

An average normalized readout, MNRn, is then calculated from normalized readouts for three irradiation cycles and for each TLD chip as follows:

$$\text{MNRn} = (\text{TLDn(NR1)} + \text{TLDn(R2)} + \text{TLDn(R3)/3} \tag{5.4}$$

Finally a sensitivity correction factor for TLDn can be determined as follows:

$$\text{SCF (TLDn)} = \text{Mean readout /MNRn} \tag{5.5}$$

The detailed calculations of the SCF for each TLD chip are presented in Appendix C.

5.2.2.6 Dose linearity range for TLD chips

The dose response linearity of TLD-100 chips was investigated by exposing the TL detectors to different doses from 0.01 to 10 Gy. For each dose, three TLDs were irradiated in the solid water phantom described previously (Section 5.2.2.5). The TLDs were irradiated with a 6 MV x-ray beam from Varian iX linear accelerator at maximum depth for a 10 x 10 cm^2 field size at 100 cm SSD.

After irradiation, the TLD chips were read the following day. Each reading was corrected for sensitivity and for background. The TL readout of each detector was calculated, with correction for R_{BKG}, SCF, and BCF, as follows:

$$TL_i = (R_i - R_{BKG}) \cdot SCF_i \cdot BCF\,, \tag{5.6}$$

where BCF is the batch correction factor which accounts for the change of the readout of each TLD chip due to changes in its characteristic due to processing, irradiation, reading and annealing. It is obtained using the following relation:

$$BCF = \frac{\bar{R}_{normalized}}{\bar{R}_{measured}}, \tag{5.7}$$

From the previous section, the mean reading of 5 TLD chips, randomly selected, was taken. The SCF for these chips was calculated as explained before. The mean reading of these detectors is the normalized readout ($\bar{R}_{normalized}$). During the measurement of the dose linearity response of the TLD chips, the randomly selected TLD chips were irradiated again to the same dose and under same conditions as in the previous section. The TL reading of these chips was corrected for sensitivity (SCF) and for background (R_{BKG}). The mean reading of these dosimeters is called ($\bar{R}_{measured}$). The ratio of mean readings for these TLDs is called the batch correction factor (BCF) as given in Equation 5.7.

5.2.2.7 MammoSite experimental study

The experimental measurements were carried out using in-house breast equivalent tissue phantom (described in part one, Section 5.1.2.1). The MammoSite balloon was first filled with saline only to the desired volume and the two halves of the phantom were joined together as discussed in part one (section 5.1.2.2 and shown in Figure 5.3). Computed tomography images of the breast phantom were then obtained from a CT scanner (Philips Medical Systems Ltd, Stevenage, UK) using axial slices of 3-mm thickness. For high dose rate (HDR) MammoSite brachytherapy treatment planning, the CT images were transferred via network to the Plato brachytherapy treatment planning system (Plato BPS v14.3.2, Nucletron B-V., Veenendaal, The Netherlands).

To measure the effect on dose distribution in the presence of contrast medium inside the MammoSite balloon, the balloon was first filled with saline only and the TLD chips were placed in the breast phantom at distances from the balloon surface from 1 cm to 5 cm in 1 cm steps as shown in Figure 5.14. The detectors were positioned in a direction perpendicular to the catheter to avoid averaging of the dose along the gradient. The MammoSite treatment plan, which contains the source position and the dwell time information, was sent to the treatment control unit (for the Nucletron microSelectron HDR afterloder) to be delivered. The HDR source was sent to the balloon centre to deliver the prescribed dose. The MammoSite treatment consisted of prescribing 3.4 Gy at 1 cm from the surface of the balloon. The HDR source had an activity of approximately 10 Ci (370

GBq) during this study. Figure 5.15 shows the experimental setup for TLD irradiation in the breast phantom.

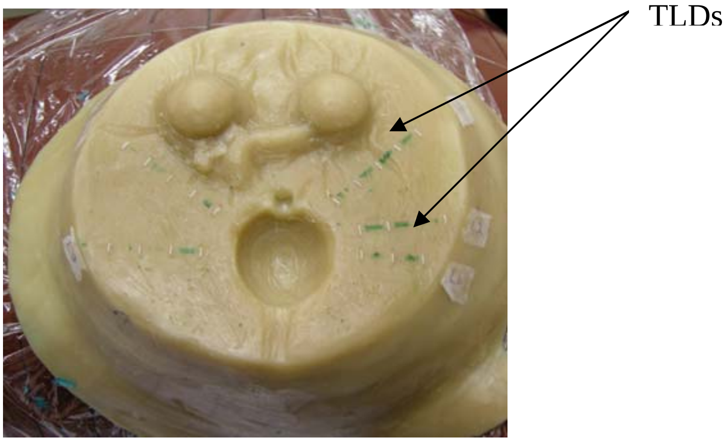

Figure 5.14. positions of TLDs at various distances from the balloon surface.

Following irradiation, the TLD chips were first thoroughly cleaned to remove any residual grease from dosimeters surfaces. The TLD chips were then read according to the procedure explained previously. They were then annealed and reused again. The TLD measurement procedure was repeated for balloon filled with contrast only, 50% saline plus 50% contrast concentration, and 85% saline plus 15% contrast concentration. For each measurement, several TLD chips were set aside without any radiation and used for background subtraction. The TL readout of each detector was calculated using equation 5.6.

The batch correction factor for HDR exposure was determined in a similar manner as explained previously (Section 5.2.2.6) by exposing a randomly selected TLDs to HDR ^{192}Ir source instead of 6 MV x-rays. 5 TLD chips were positioned at the centre of the well chamber and the HDR source was driven at the centre of the well chamber to deliver a dose of 5 Gy. This was relative calibration only against known dose. Figure 5.16 is a representation of the experimental setup for exposing the TLDs to HDR source. In Figure 5.16, the TLDs are not seen because they were placed within an insert for HDR source. Equation 5.7 was used to calculate the BCF.

Figure 5.15. Experimental setup for dose measurements in the breast phantom using TLD chips.

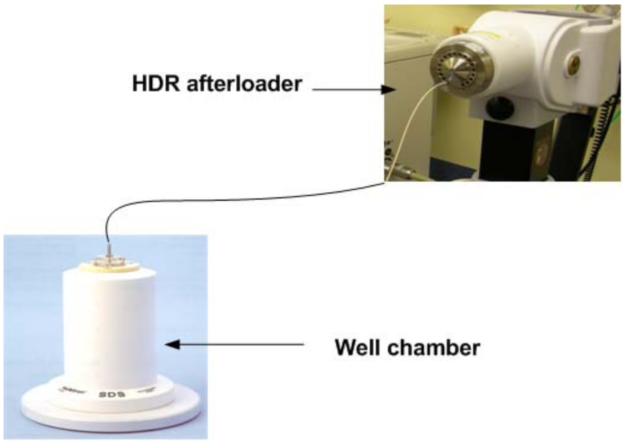

Figure 5.16. Experimental measurement setup for irradiating the TLDs to HDR source.

5.2.2.8 Dose reduction factor

The readouts of the TLDs were used to caculate the dose reduction factor (DRF) resulting from the presence of contrast solution in the MammoSite balloon. The DRF is defined as the dose with the contrast in the balloon to the dose with saline only. It is calculated using the following relation:

$$DRF = \frac{D(E,d,x,C)}{D(E,d,x,0)}, \tag{5.8}$$

where D is the dose expressed as a function of photon energy (E), the diameter of the balloon (d), the distance from the balloon surface (x), and concentration of the contrast media (C). The impact on dose reduction on the Tumour control probability (TCP) was then investigated.

5.2.3 Results

5.2.3.1 TLD reading period

Figure 5.17 shows the contribution of the first two peaks to the TL signal, the detectors were read immediately after irradiation. Figure 5.18 shows the contribution of peak two to the TL signal, the detectors were read about 1.5 hours after irradiation. Figure 5.91 represents the glow curve read at least 24 h waiting period, showing that the first two peaks are no longer contributing to the TL signal.

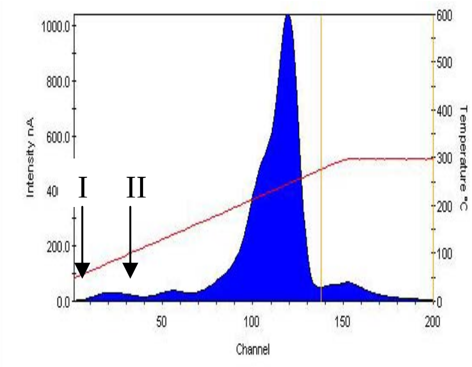

Figure 5.17. Glow curve for LiF TLD-100 chips (the TLDs were read immediately after irradiation).

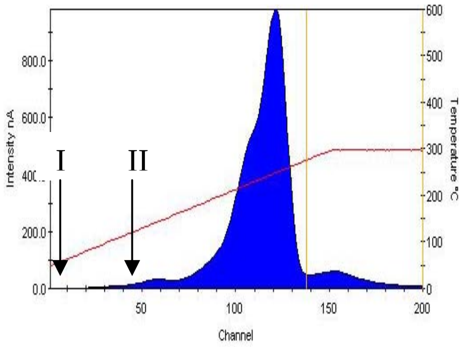

Figure 5.18. Glow curve for LiF TLD-100 chips (read 1.5 hour after irradiation).

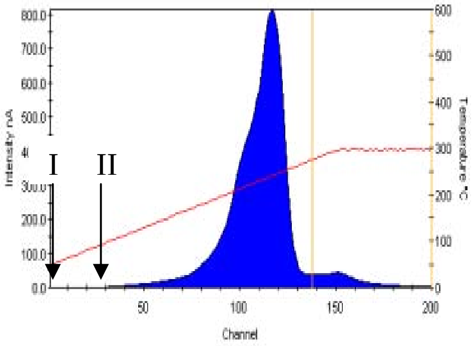

Figure 5.19. Glow curve for LiF TLD-100 chips (read at least 24 h after irradiation)

5.2.3.2 TLD calibration

The individual SCFs of each TLD-100 chip were determined. It was found that the maximum SCF is 1.06, the minimum SCF is 0.96, and the mean value is 1.001 with standard deviation of 1.3%. The SCF for each TLD-100 chip is tabulated in Table 5.3. Figure 5.20 shows that the dose response curve for TLD-100 chips is linear up to 6 Gy. The mean relative deviation over the measurement was 1.9% with a range of 1.1-2.6%.

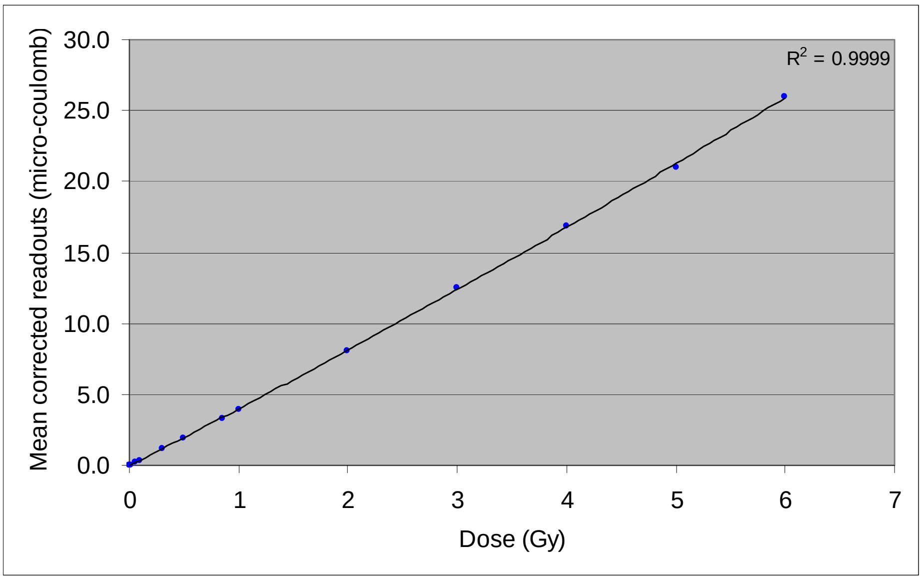

Figure 5.20. Dose response curve for TLD-100 chips (2% relative deviation).

Table 5.3. Sensitivity correction factor for each TLD-100 chip used in the current study.

TLD #	SCF	TLD #	SCF	TLD #	SCF	TLD #	SCF	TLD #	SCF
1	1.01	11	1.01	21	0.99	31	1.02	41	0.98
2	0.96	12	0.98	22	0.99	32	1.01	42	0.98
3	1.02	13	0.99	23	1.00	33	1.03	43	0.99
4	1.06	14	0.99	24	1.00	34	1.01	44	1.04
5	1.01	15	0.97	25	1.04	35	0.96	45	0.99
6	0.98	16	1.01	26	0.98	36	1.01	46	0.98
7	0.99	17	1.01	27	1.06	37	0.98	47	1.02
8	1.01	18	0.96	28	1.02	38	1.02	48	0.99
9	0.97	19	0.99	29	1.02	39	1.02	49	1.029
10	0.98	20	1.00	30	0.97	40	0.98	50	1.014

5.2.3.3 Phantom measurements using TLDs

Figure 5.21 presents the dose fall as a function of distance starting at 1 cm from the balloon surface. To measure the extent of dose perturbation for various contrast concentration in the MammoSite balloon, the dose was normalized to that with the balloon filled with saline only. Figure 5.21 also shows TLD measurement results of the relative dose as a function of distance for the balloon filled with contrast only. The balloon filled with 100% contrast medium resulted in up to 10% dose reduction at the prescription point due to attenuation of the radiation. Figure 5.22 shows TLD measurements results of the relative dose as a function of distance for the balloon filled with saline only and that filled with 50% saline plus 50% contrast concentration. The variation of dose with distance from the balloon surface, for the saline-filled balloon with 50% contrast concentration, resulted in approximately 5% reduction in the dose at the prescription point. Figure 5.23 also shows results of the relative dose as a function of distance for the balloon filled with 85% saline plus 15% contrast concentration. A 15% contrast concentration produced around 2% dose reduction at the same distance compared to saline solution. The percentage difference in the dose reduction increased with increasing contrast concentration. The difference between the saline curve from other curves indicates the dosimetric effects due to attenuation by contrast medium.

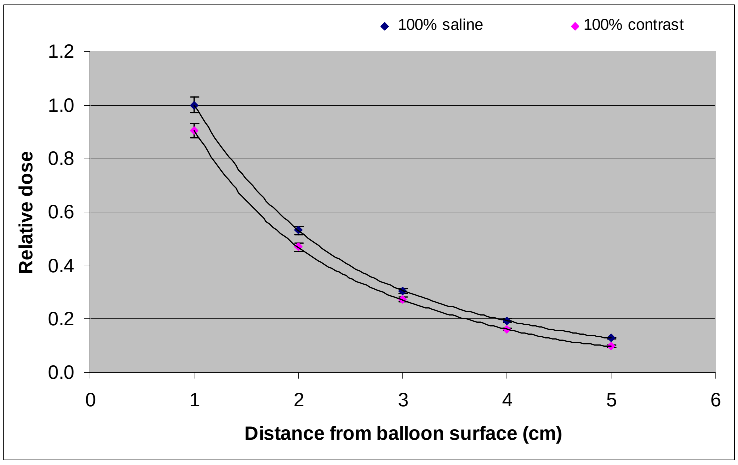

Figure 5.21. TLD measurements results of dose fall-off as a function of distance for balloon filled with saline only and filled with contrast only. The measurement uncertainty with TLDs was within 3% or less.

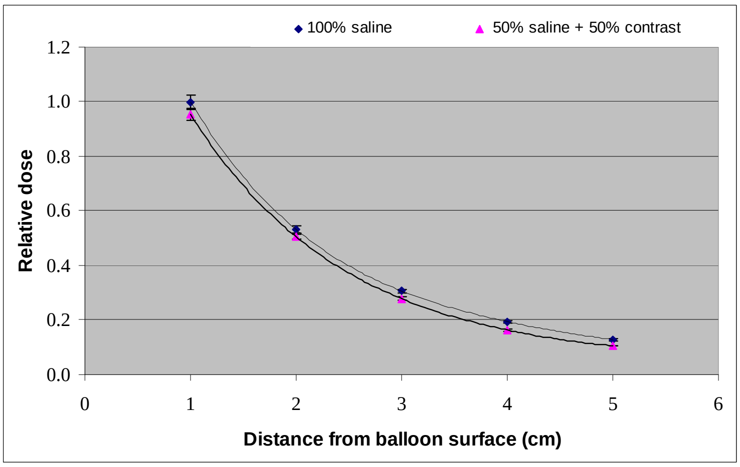

Figure 5.22. TLD measurements results of dose fall-off as a function of distance for balloon filled with saline only and filled with 50% saline plus 50% contrast concentration. The measurement uncertainty with TLDs was within 3% or less.

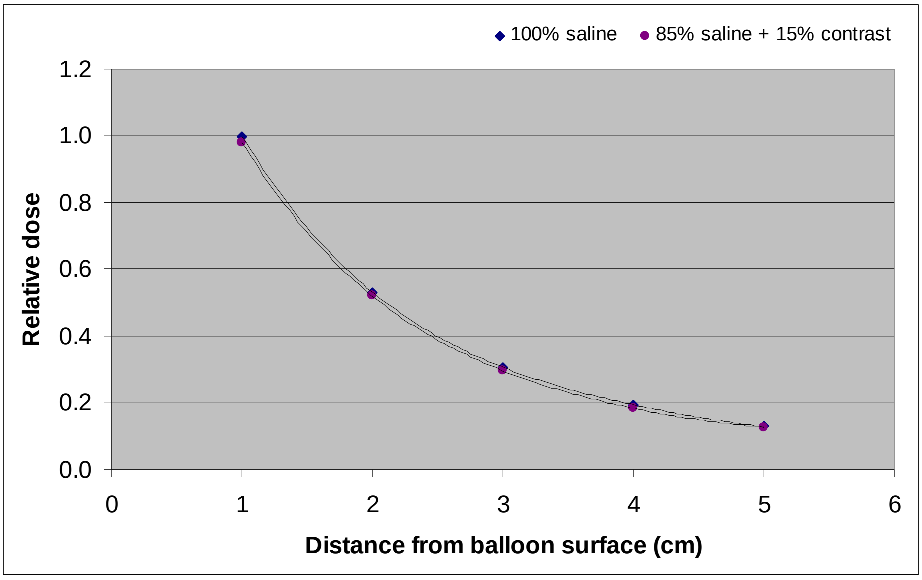

Figure 5.23. TLD measurements results of dose fall-off as a function of distance for balloon filled with saline only and filled with 85% saline plus 15% contrast concentration. The measurement uncertainty with TLDs was within 3% or less.

5.2.3.4 Comparison between simulations and measurements

Figure 5.24 shows a direct comparison of the TLD measured relative dose and the Monte Carlo computed relative dose as a function of distance starting at 1 cm from the balloon surface, for balloons filled with saline and different contrast concentrations. The dose pattern shows a sharp fall off as a function of distance from the balloon surface. The measured and Monte Carlo calculated doses are in agreement within the measurement uncertainty and Monte Carlo statistical errors.

5.2.3.5 Dose reduction factor

The dose reduction factors were calculated, for the MammoSite balloon with 4 cm in diameter, using Monte Carlo simulation and TLD measurements. The dose reduction factor value as a function of various contrast concentration levels is shown in Figure 5.25. The DRF is larger for higher contrast concentrations. The DRF values at 1 cm from the balloon surface are shown in Table 5.4.

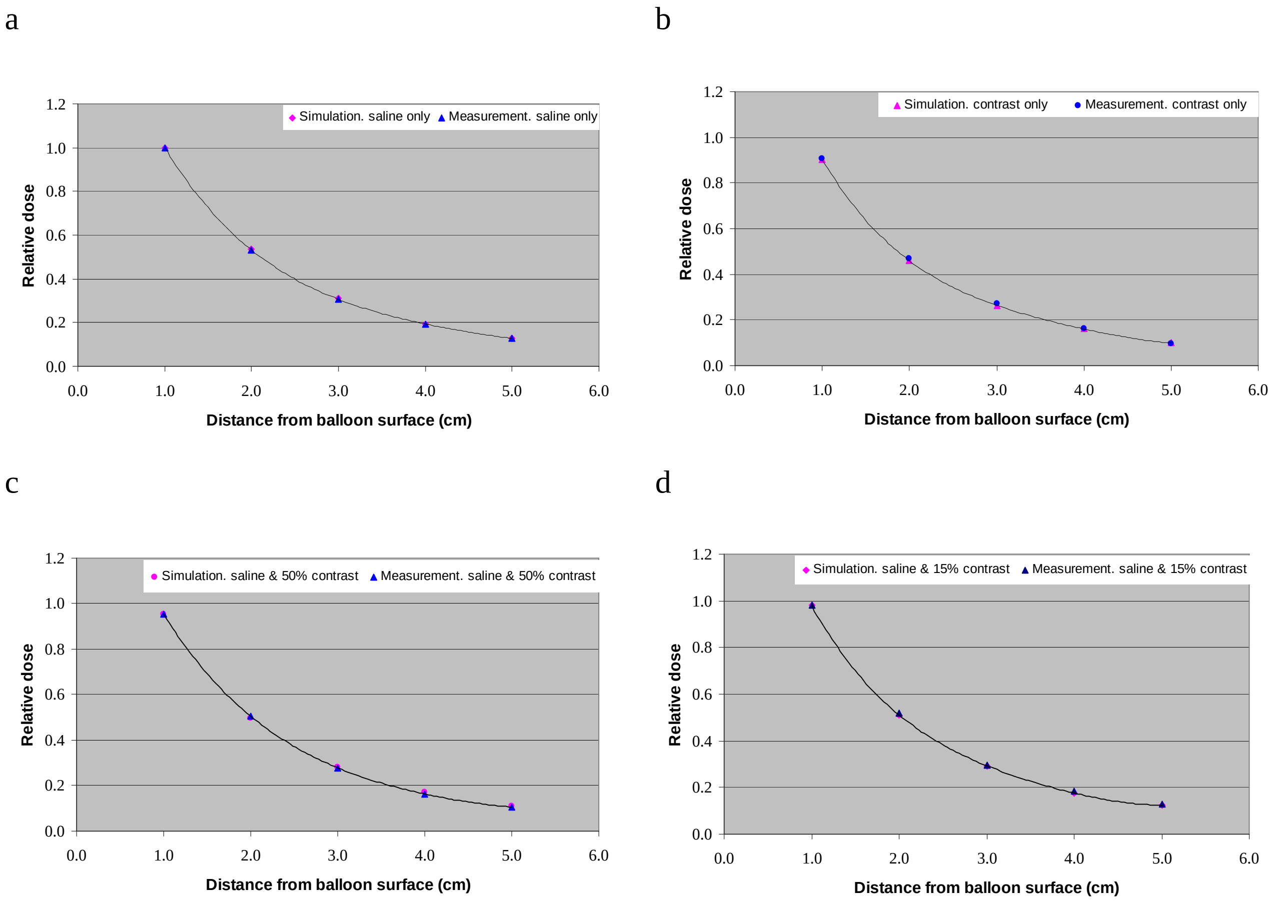

Figure 5.24. Comparison of Monte Carlo simulation and TLDs measurements showing the variation of dose as function of distance starting at 1 cm from the balloon surface for a balloon filled (a) with saline only, (b) with 100% contrast concentration only, (c) with saline with the addition of 50% contrast concentration and (d) with saline with the addition of 15% contrast concentration. The uncertainties in Monte Carlo calculation and TLD measurements were 1.8% and 3% respectively.

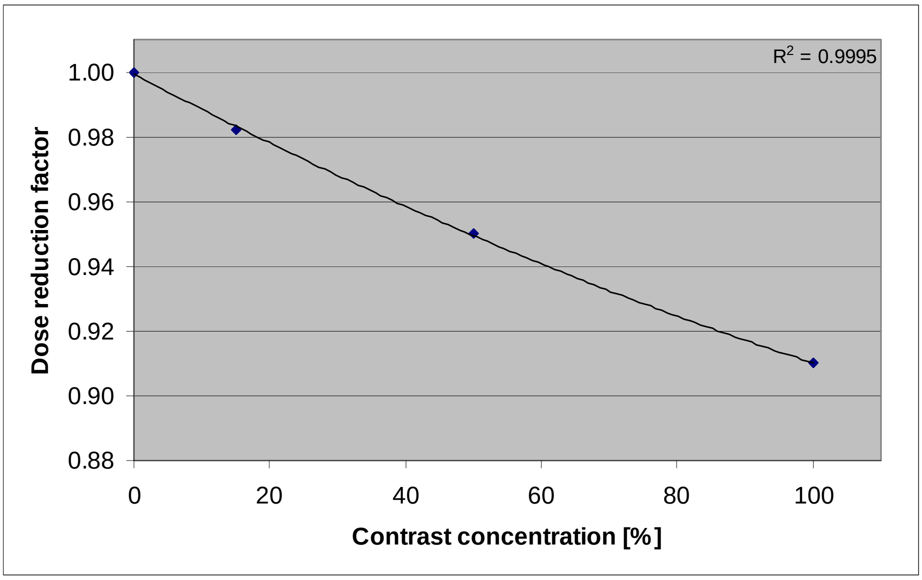

Figure 5.25. Dose reduction factor (at 1 cm from balloon surface) attributable to attenuation from various contrast concentrations in the MammoSite balloon. The relative uncertainty in the DRF is 1.8%.

Table 5.4. The dose reduction factor values at 1 cm from the balloon surface, for balloon filled with saline and / or various contrast concentrations. The relative uncertainty is 1.8%.

Contrast concentration (%)	Monte Carlo DRF	TLD measurements DRF	DRF (average)
0	1	1	1
15	0.980	0.982	0.98
50	0.954	0.952	0.95
100	0.903	0.905	0.90

5.2.3.6 Tumour control probability results

The American Association of Physicists in Medicine (AAPM) Task Group 40 recommendation for intracavitary brachytherapy allows for ± 15% in the delivery of the prescribed dose contributing from all possible sources of uncertainties [121]. The DVHs (from chapter four) and Monte Carlo simulations were used to estimate the combined impact of uncertainties in MammoSite brachytherapy on the tumour control probability (TCP). The TCP was calculated using the Poisson model [104] which was discussed in chapter four (Section 4.2.5) of this thesis. The TCP results for the combined MammoSite uncertainties are summarised in Table 5.5.

The TCP, with the source at the balloon centre, spherical balloon shape and 15% contrast concentration inside the balloon, was about 99%. The TCP, with 1 mm balloon deformation and 15% contrast concentration inside the balloon, was about 96%. The TCP, with 2 mm balloon deformation and 15% contrast concentration inside the balloon, was reduced by 6%. The TCP, with 4 mm balloon deformation and 15% contrast concentration inside the balloon, was reduced by 26%. The TCP, with the source at the balloon centre, spherical balloon shape and 50% contrast concentration inside the balloon, was about 98%. The TCP, with 4 mm balloon deformation and 50% contrast concentration inside the balloon, was reduced by more than 30%.

A 15% contrast concentration and 1 mm balloon deformation caused a reduction in the TCP by 3% whereas 50% contrast concentration and 1 mm balloon deformation caused reduction in the TCP by 4%. This reduction was still within the TCP gradient region as shown in Figure 5.26. However, near the TCP gradient region, the amount of contrast in the balloon had a significant impact on the treatment effectiveness; it reduced the TCP by 10%.

This study suggests that the combined uncertainties in MammoSite treatments should be kept within 2 mm balloon deformation and 15% contrast concentration.

Table 5.5. TCP resulting from the combined uncertainties encountered in the MammoSite technique. The error in the TCP calculation is ± 3%

Balloon deformation (mm)	Contrast concentration %	TCP %
0	15	99
0	50	98
1	15	96
1	50	95
2	15	94
2	50	90
4	15	74
4	50	70

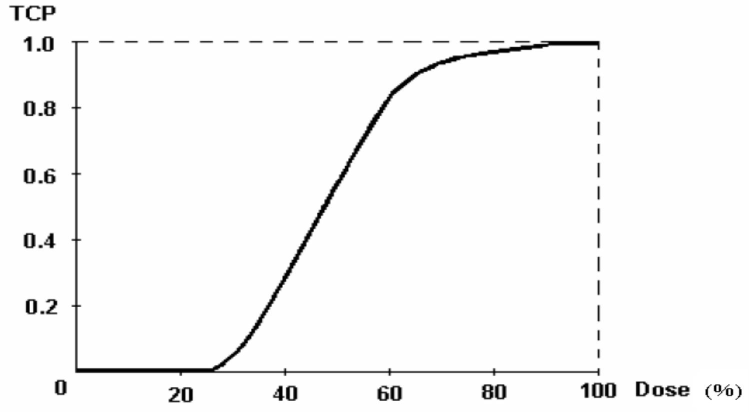

Figure 5.26. TCP curve. It illustrates the impact of combined uncertainties away and near the TCP gradient region.

5.2.4 Discussion & conclusion

This section presented a comprehensive study, investigating the impact of the contrast medium inside the MammoSite balloon on the dose distribution, performed on a humanoid phantom with small thickness TLD chips, as opposed to other studies carried out in a water tank with a large ion chamber. In addition, the Monte Carlo simulations were based on CT data which resembled patient geometry as opposed to other studies where the Monte Carlo calculations were performed in a water phantom. The measured and Monte Carlo computed relative doses were in excellent agreement all within the measurement uncertainty and Monte Carlo statistical errors.

The dose reduction resulting from the use of high atomic number contrast (Iodine) can cause considerable uncertainty in the MammoSite dose. As shown by Monte Carlo simulations and TLD measurements, the contrast medium inside the MammoSite balloon resulted in a reduction of dose at the prescription point. The magnitude of dose reduction depends on the concentration of contrast. The dose perturbation is larger for higher contrast concentration. A 15% contrast concentration caused 2% dose reduction at 1 cm from the balloon surface while a 100% contrast concentration produced 10% dose reduction at the same point.

Based on the current investigation, we suggest that the amount of radiographic contrast used during MammoSite breast brachytherapy should be minimized (15%) to avoid potential significant reduction in the delivered dose.

In conclusion, the combined uncertainties associated with the MammoSite brachytherapy technique, to the value of a 2 mm balloon deformation and 15% contrast concentration, have accepted impact on the tumour control probability. As a result treatment protocols should be used that accept only 2 mm balloon deformation and contrast concentration values below 15%.

Chapter 6

Monte Carlo simulation of linear accelerator treatment head

6.1 Introduction

Radiation therapy is the medical use of ionizing radiation for the treatment of patients with cancer. Radiation therapy may be delivered alone or in combination with other treatment techniques such as surgery and chemotherapy. External beam radiation therapy is delivered with a machine that is used to produce high energy x-rays. The linear accelerator (linac) is the most common type of treatment machine that is used for external radiation delivery. Primary electrons are accelerated within the waveguide of the linac to high energies (up to 25 MeV), after which they hit a metal target composed of material with a high atomic number where they produce bremsstrahlung. A variety of filters and collimating devices are used to shape the final photon beam. Monte Carlo calculation is the most accurate method to calculate dose distributions in patients treated with radiation [39, 47, 54]. A prerequisite for such calculations is to have an accurate model of the linear accelerator.

At our institution, patient with early stage breast cancer are treated with external beam radiotherapy technique (EBRT). The EBRT treatment is commonly delivered using 6 MV photon beams, including asymmetric fields, physical wedges and multi-leaf collimators (MLCs). It is therefore necessary to establish an accurate Monte Carlo model of the linac. This is done by modelling the treatment head including open field, blocked (asymmetric) field, physical wedges with different angles and MLC field. This chapter presents a development of a Monte Carlo model of Varian 600 C/D (Varian Oncology Systems, Palo Alto, CA) with 6 MV x-ray beam energy available at the Royal Adelaide Hospital. The Monte Carlo model was validated against measurements.

As introduced in Chapter 2 (Section 2.4.1.1), the BEAMnrc [39, 55] code is a specialised Monte Carlo user code for the modelling of linear accelerators. The treatment head of the linear accelerator was modelled in this work using a number of component modules (CMs) available within the BEAMnrc. The dimensions, materials and positions of the different accelerator components used in this study are based on the manufacturer’s specifications.

The linear accelerator components considered in simulations consist of the target, the primary collimator, the flattening filter, the monitor chamber, the mirror, the secondary collimator, the multi-leaf collimator and physical wedges.

The Monte Carlo simulations were performed at 100 cm SSD for square fields, blocked (asymmetric) field, MLC shaped square fields and square fields with four different wedge angles (15^0, 30^0, 45^0, and 60^0). The output of a BEAMnrc simulation is in the form of phase space data files. These files contain information about the particles crossing the linac components. For model verification purposes, the DOSXYZnrc was subsequently used for dose distribution calculations from the phase-space files generated by BEAMnrc in a rectangular water phantom. Dose distribution curves obtained from the linac models were compared against measured dose profiles to validate the models. The Monte Carlo model constructed in this chapter is to be used for the simulation of a patient, undergone EBRT treatment for early stage breast cancer, treatment plan in Chapter Seven.

6.2 Methods and materials

6.2.1 Monte Carlo simulation

Monte Carlo simulations track the interactions of an incident particle through the linear accelerator and take into account the statistical probability cross-sections for each material. For a linac, electrons are incident on a tungsten target producing bremsstrahlung photons which are collimated and shaped by the linac head component modules. In the current study, the Monte Carlo simulation was performed using the EGSnrc system code running in Linux. The process of calculating the dose distribution in this work was divided into two steps. First, the BEAMnrc user code was employed to transport the x-rays and electrons from the target to a predefined scoring plane where photons were written to a phase space file. The phase space file was generated in air at a plane 100 cm away from the target. The phase space file was used as input for the second step in which particles were transported through a 30 x 30 x 30 cm^3 water phantom. The water phantom was divided into voxels and the dose distributions were computed using the DOSXYZnrc user code.

6.2.2 Linear accelerator model

A model of the Varian 600 C/D linear accelerator (Varian Oncology Systems, Palo Alto, CA) was built using the BEAMnrc [55] user code. The basic model of the Linac had previously been generated [122] and has been expanded for blocked, multi-leaf collimators (MLC) and wedged fields in the current work. In the modelling process, the information about the materials, positions, shapes and dimensions of the different accelerator components were based on the manufacturer's specifications (Varian Oncology System, Monte Carlo project 1996). The linac model consisted of the target, the primary collimator, the flattening filter, the monitor chamber, the mirror, upper and lower jaws, multi-leaf collimators (MLCs) and physical wedges. Table 6.1 presents the component modules used in modelling of the Varian 600 C/D linear accelerator treatment head.

Table 6.1. Description of the CMs which were used in modelling of the linac head in BEAMnrc code.

Component module	Distance from target to isocentre (cm)	Material and physical density	Accelerator element
SALBS	0.0	Tungsten (W), 19.30 g/cm^3 Copper (Cu), 8.93 g/cm^3	A model of the x-ray target
FLATFILT	2.1	Tungsten (W), 19.30 g/cm^3 Copper (Cu), 8.93 g/cm^3	A model of 2 components: the primary collimator and the flatting filter. The flattening filter is surrounded by the primary collimator
CHAMBER	11.31	Outer plate made of steel, 8.06 g/cm^3, and inner plate made of copper Upper & lower cavity made of Mica, 2.90 g/cm^3	A model of monitor ion chamber
MIRROR	16.85	Mylar, 1.38 g/cm^3	A model of the light field mirror
JAWS	Upper (Y)– jaws, 28 Lower (X)–jaws, 36.7	Tungsten (W), 19.30 g/cm^3	A model of secondary collimator jaws
VARMLC	47.83	Tungsten (W), 19.30 g/cm^3	A model of multi-leaf collimators
SLABS	57.29	POLYSTY, 0.93 g/cm^3	A model of 0.3 cm thick plate before the wedge
PYRAMIDS	57.6	15^0 wedge, steel, 8.06 g/cm^3 30^0 wedge, steel, 8.06 g/cm^3 45^0 wedge, lead, 11.34 g/cm^3 60^0 wedge, lead, 11.34 g/cm^3	A model for wedges with different angles
SLABS		Air, 1.2048 x 10^{-3} g/cm^3	A model of additional air region extending to a width that the phase space file is scored at 100 cm from the source.

The steps illustrated in Figure 2.4 (Chapter 2) were followed to construct a linear accelerator model using the BEAMnrc. The incident electron beam was modelled using source routine number 19 (see Figure 6.2) available within the BEAMnrc [55]. Source 19 describes an electron beam entering the centre of the x-ray target at 90^o and having Gaussian distribution. The spectrum of the incident electron beam is 5.9 ± 0.1 MeV. A phase space file was generated for each linac model assuming a 6 MeV incident electron beam having a Gaussian radial distribution with a full-width-at-half-maximum (FWHM) of 0.13 cm. Figure 6.1 presents the simulated geometry of the linac model.

Target

The target in the linear accelerator is made of tungsten and copper. This is where most of the bremsstrahlung photons are produced.

Primary collimator

The primary collimator is made of tungsten. It has a conical opening with a 14^{o} angle from the isocentre line.

Flattening filter

The flattening filter is made of copper and has a cone shape. The flattening filter is positioned inside the opening of the primary collimator (see Figure 6.1) for a 6 MV Varian 600 C/D linac.

Monitor chamber

The outer and the inner plates are made of steel and copper respectively. Upper and cavity are made of Mica.

Mirror

The mirror is made of Mylar at an angle of 35^{0}.

Secondary collimator

The secondary collimator jaws are made of tungsten.

Multi-leaf collimator

The Varian 600 C/D is equipped with a multi-leaf collimator (MLC) consisting of 40 leaves on each side. The projected thickness of each leave is 1 cm at 100 cm from the focal point.

Physical wedge

The physical wedges are usually mounted externally on the treatment head of the machines. A physical wedge is usually made of high density materials, such as lead or steel.

Air

The air gap is between the accelerator and the water phantom.

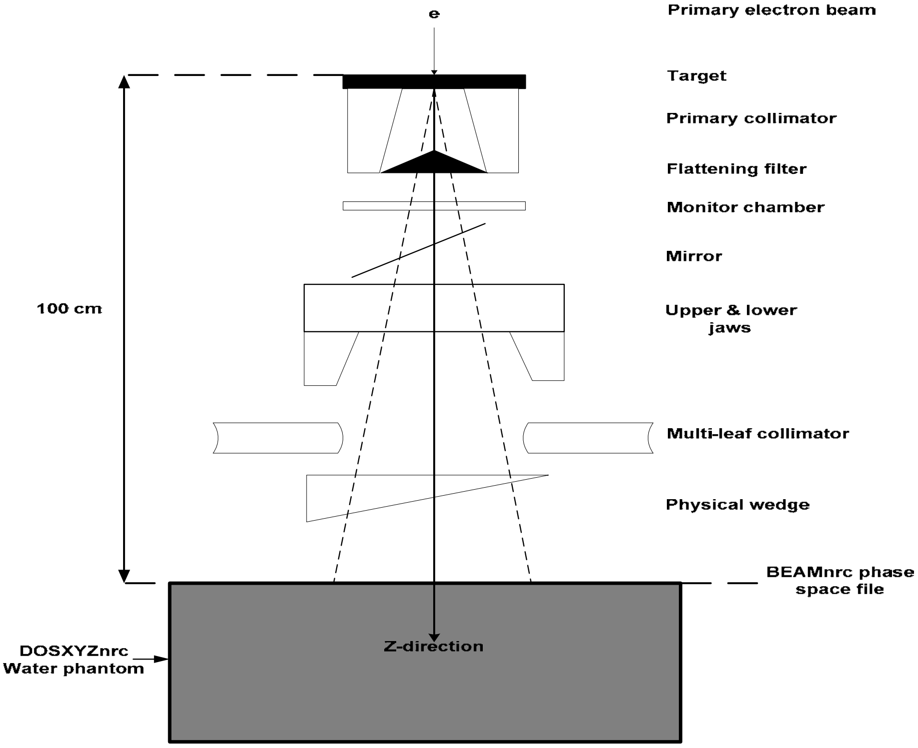

Figure 6.1. Schematic representation of simulated geometry of Varian 600 C/D linac head used in this study.

NOTE:
This figure is included on page 100
of the print copy of the thesis held in
the University of Adelaide Library.

Figure 6.2. The geometry of a parallel circular beam (ISOURC = 19) with 2D Gaussian distribution (curtesy [55]).

6.2.3 BEAMnrc models

6.2.3.1 Open field

Open field size (10 x 10 cm^2) was simulated with the jaws defining the field in the linac model. Figure 6.3 illustrates the linac model for 10 x 10 cm^2 field size. An example input file for the BEAMnrc code is given in the Appendix A. A total of 6 x 10^7 incident histories on the target were simulated. The phase space data file was scored at a distance of 100 cm SSD from target.

6.2.3.2 Asymmetric (half-blocked) field

The asymmetric field was modelled by blocking the field using one of the lower jaws to simulate 0 x 10 cm field size. 10^8 particles were simulated and the phase space data file was scored at 100 cm SSD from the target.

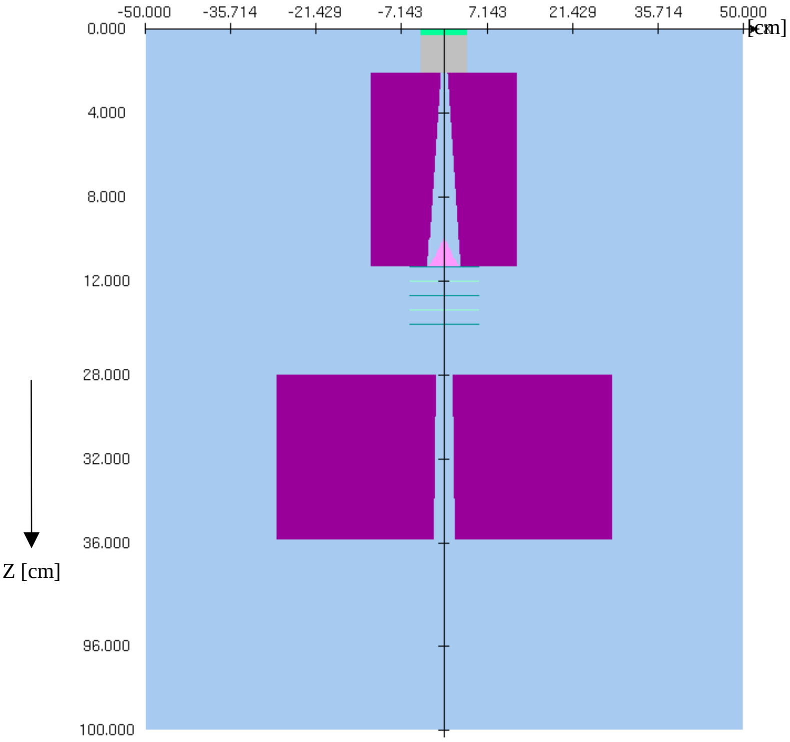

Figure 6.3. Schematic geometry of linac illustrating the open field modelled in Monte Carlo simulations.

6.2.3.3 MLC modelling

A multi-leaf collimator is a beam collimation device which consists of opposing pairs of motor driven leafs. The independent motion of the leaves makes it possible to define irregular field shapes therefore allowing the radiation field to be conformed to the tumour. MLCs are also used to block normal critical structures from receiving high radiation dose. The use of MLC in radiotherapy leads to the increase of the treatment efficiency by replacement of beam locks [123]. Beam blocks are made in special workshops (mould room) and may involve handling of toxic material (lead or cadmium).

The Varian 600 C/D linear accelerator is equipped with 80 MLC leaves (40 on each side of the treatment field). The BEAMnrc component model VARMLC was used to model the geometry of the MLC. The geometry of this component module is defined in Figure 6.4.

A symmetric MLC opening of 10 x 10 cm^2 field size was simulated. For this field the collimating jaws were positioned at 20 cm x 20 cm. Figure 6.5 illustrates the Monte Carlo model for the MLCs. A total of 10^8 particles were simulated and the phase space file was scored at 100 cm SSD from the target.

NOTE:
This figure is included on page 102
of the print copy of the thesis held in
the University of Adelaide Library.

Figure 6.4. Geometry of the VARMLC component module (courtesy [55]).

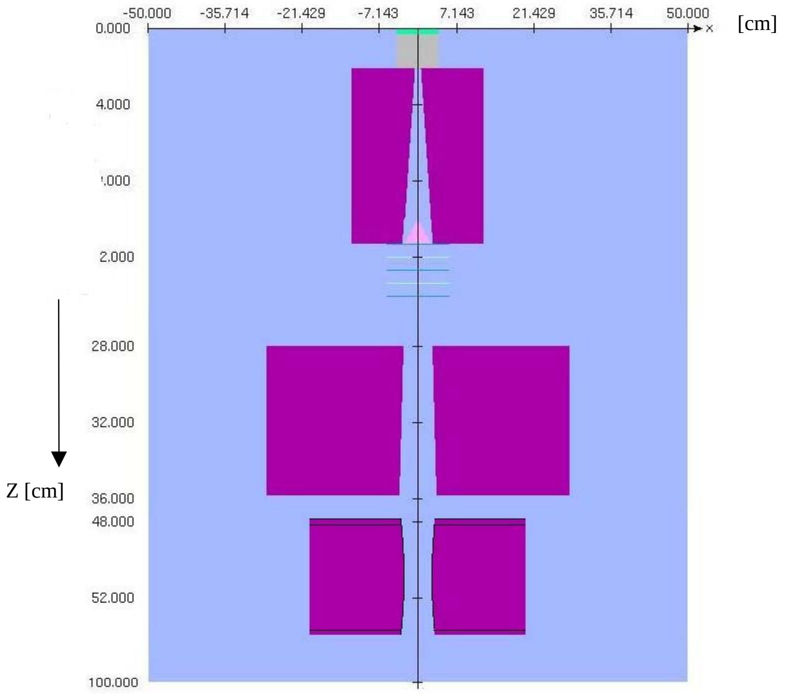

Figure 6.5. Schematic geometry of linac illustrating the MLC modelled in Monte Carlo simulations.

6.2.3.4 Physical wedges modelling

The Varian 600 C/D linear accelerator is facilitated with a set of physical wedges of angles 15^0, 30^0, 45^0 and 60^0. The physical wedges are mounted externally on the linac treatment head and are normally used to modify the dose distribution. 15^0 and 30^0 wedges are made of steel alloy with density of 7.86 g/cm^3. 45^0 and 60^0 are made of lead alloy with density of 11.20 g/cm^3.The Monte Carlo calculations were performed at 100 cm SSD for 10 x 10 cm^2 field size with four different wedge angles 15^0, 30^0, 45^0 and 60^0.

The PYRAMIDS component module, available within the BEAMnrc, was used to model the physical wedges of angle 15^0, 30^0, 45^0 and 60^0. The geometry of the PYRAMIDS CM is illustrated in Figure 6.6. Separate models were created for the different wedges. Figure 6.7 shows a Monte Carlo model for a 45^0 physical wedge. Up to 10^8 particles were run to generate different phase space files for wedged fields of angles of 15^0, $30^0$and 45^0. For the 60^0 physical wedge, 2 x10^8 particles were simulated to produce number of photons in the phase space file leading to 2% statistical uncertainty.

NOTE:
This figure is included on page 103
of the print copy of the thesis held in
the University of Adelaide Library.

Figure 6.6. Geometry of the PYRAMIDS component module (courtesy [55]).

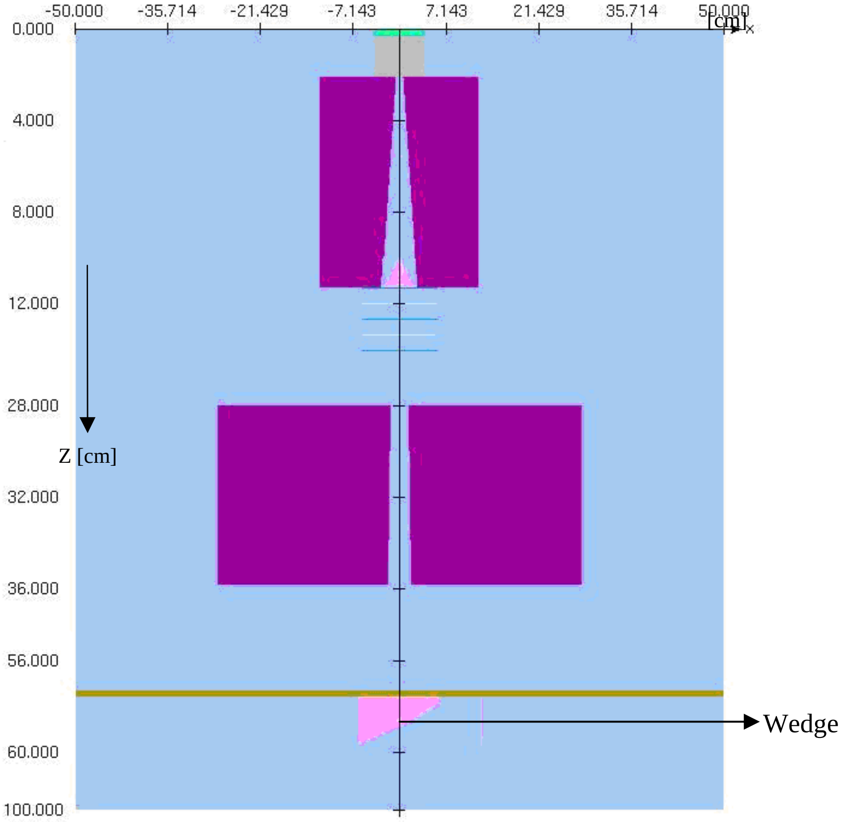

Figure 6.7. Schematic geometry of linac illustrating a 45^0 physical wedge modelled in Monte Carlo simulations.

6.2.4 Selection of variance reduction in BEAMnrc

To improve the calculation efficiency, various variance reduction techniques, such as range rejection and directional bremsstrahlung splitting were employed for the accelerator modelling.

6.2.4.1 Electron and photon transport parameters

The EGSnrc Monte Carlo code contains updated cross-sections for accurate photon and electron transport [124]. The following electron and photon transport parameters are widely used in the literature and were set in BEAMnrc simulation [55].

- Photon transport cutoff (PCUT) = AP = 0.01 MeV; this threshold was used in all the component modules in the simulations. This will result in photons with energies below 0.01 MeV being terminated and all their energy will be absorbed in the medium.

- Electron transport cutoff (ECUT) = AE = 0.700 MeV; which is the minimum energy of an electron in order to be terminated from the medium.

- Bound Compton scattering = OFF; this option corrects for the Klein-Nishina cross-section assumption that a Compton-electron is not bound during the interaction. This option is not included during the simulation because the photon energies are above 1 MeV.

- Pair angular sampling = Simple; it was set to default, which is the simplest model to determine the angle between the electron and positron during pair production. It was set to "Simple" since details of the electron and positron tracks are of less interest in this work.

- Photoelectron angular sampling = OFF; this option estimates the angular distribution of photoelectrons after a photoelectrical effects. Details of these tracks are of no interest in this work, therefore this option is not used during the simulations.

- Rayleigh scattering = OFF; this option is more relevant for energies under 100 keV.

- Atomic relaxation = OFF; this option is used to consider which process the atom undergoes to return to its ground state, when lacking an electron from a photoelectric effect or a Compton interaction.

- Global SMAX = 5 cm

- ESTEPE = 0.25 cm

- XIMAX = 0.5 cm
- Boundary crossing algorithm (BCA) = PRESTA-I

- Skin depth for BCA = 0

- Electron-step algorithm = PRESTA-II

- Spin effects = ON

- Bremsstrahlung angular sampling = Simple

- Bremsstrahlung cross section = BH

- Electron impact ionization = OFF

6.2.4.2 Range rejection

Range rejection is used for the charged particles to save computing time during the simulations. The method is based on calculating the range of a charged particle and terminating its history if its remaining energy is not sufficient to leave the current region or reach the bottom of the accelerator. ESAVE is a variable defining the maximum charged particle energy (in MeV) at which range rejection is considered [55]. In the current study, range rejection was set with an ESAVE value of 2 MeV. This value is widely applied for 6 MeV electrons incident on tungsten target [125].

6.2.4.3 Directional bremsstrahlung splitting

Bremsstrahlung photon splitting offers the user another variance reduction technique, which improves the statistics of Bremsstrahlung photons resulting from electron interactions. BEAMnrc offers three Bremsstrahlung splitting techniques, uniform Bremsstrahlung splitting (UBS), selective Bremsstrahlung splitting (SBS) and directional Bremsstrahlung (DBS). The simulations in this work were performed with the DBS.

In DBS, the bremsstrahlung photons will split during the time of creation in NBRSPL times. The NBRSPL (number of bremsstrahlung splitting) times is defined by the user. The DBS algorithm then determines whether those photons are aimed into splitting field or away. The splitting field is defined by parameters called FS and SSD. The splitting field is the field where the bremsstrahlung photons will split. The splitting field radius and the bremsstrahlung splitting number are defined by the user. For the photons aimed into the splitting field, their weight is reduced by a factor of 1/NBRSPL. For those photons outside the splitting field, a process called Russian roulette is selected. The Russian roulette compares a random number to a survival threshold of 1/NBRSPL of each photon outside the splitting field. If the random number is less than the survival threshold, then the photon is kept otherwise it is discarded.

Directional bremsstrahlung splitting results in greater dose efficiency improvement about 8 times higher than selective bremsstrahlung splitting and about 6 times higher than uniform bremsstrahlung splitting algorithms [55]. The directional bremsstrahlung splitting variance reduction technique was used in the current simulation with splitting field radius of 30 cm, and bremsstrahlung splitting number of 1000 for the 6 MV photon beam [126].

6.2.5 Phase space files

Monte Carlo simulation with BEAMnrc produces a phase space file that contains information of the position, direction, charge, *etc*., of every particle that crosses a specified plane. Phase space files can be scored below any component module. In the current work, all phase space files were recorded at 100 cm SSD from the target. A sufficient number of particles were simulated to produce a reasonable number of photons in the phase space files. It took several days of simulation to obtain a phase space file for the separate models.

6.2.6 Dose calculations with DOSXYZnrc code

The phase space files from BEAMnrc were used as input files in the DOSXYZnrc user code for calculating the dose distribution in a water phantom. The geometry of the water phantom used in the DOSXYZnrc is shown in Figure 6.8. The phantom dimensions were 30 x 30 x 30 cm^3 and were divided into different voxel sizes in X, Y and Z directions. The thickness was 0.3 cm for the first 3.0 cm depth, and 1.0 cm for further depths. The unequal divisions were to minimize the total number of voxels while maintaining good resolution where needed.

In DOSXYZnrc simulation, the media data file 700icru (discussed in Chapter 2, Section 2.4.1.2) was used for assigning the density of the phantom material (water) and the volume surrounding the phantom was set to vacuum. The global electron cut-off energy (ECUT) was set to 0.7 MeV and the global photon cut-off energy (PCUT) was set to 0.05 MeV. Up to 10^9 particles were simulated for each run. The number of particles for each simulation was set to obtain about 2% statistical uncertainty in each simulation. The computed data was compared against the measured beam data obtained during linac commissioning.

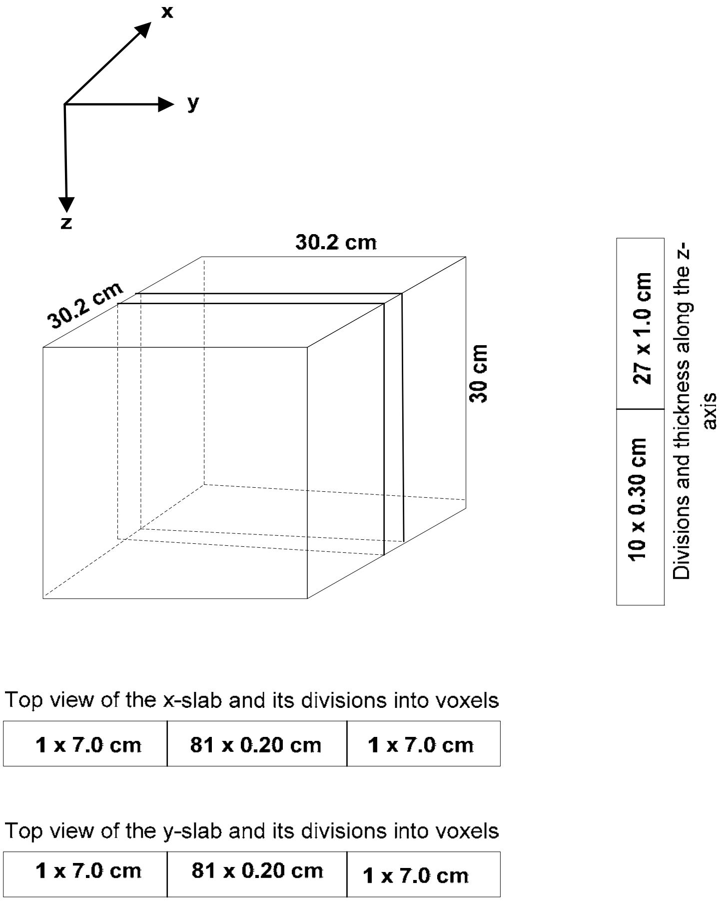

Figure 6.8. Voxel geometry used for calculation of dose deposition in a 30 cm x 30 cm x 30 cm water tank. The thickness was 0.3 cm for the first 3.0 cm depth, and 1.0 cm for further depths.

6.3 Results and discussion

The main objectives of the BEAMnrc code was to generate phase space data files that were used as input source files for the DOSXYZnrc code to calculate dose distributions in a water phantom. The present Monte Carlo calculations for open fields, blocked fields, MLC fields and wedged fields with four different angles were validated with measurements.

6.3.1 Open field

Figure 6.9 compares the percentage depth dose (PDD) curves computed with DOSXYZnrc Monte Carlo user code and ion chamber measurements in a water phantom. The PDD curves for the Monte Carlo simulation and measurements agree to within 1% or less over the whole region. The maximum dose is located at a depth of approximately 1.4 cm for the modelled square field as expected for 6 MV beams [127].

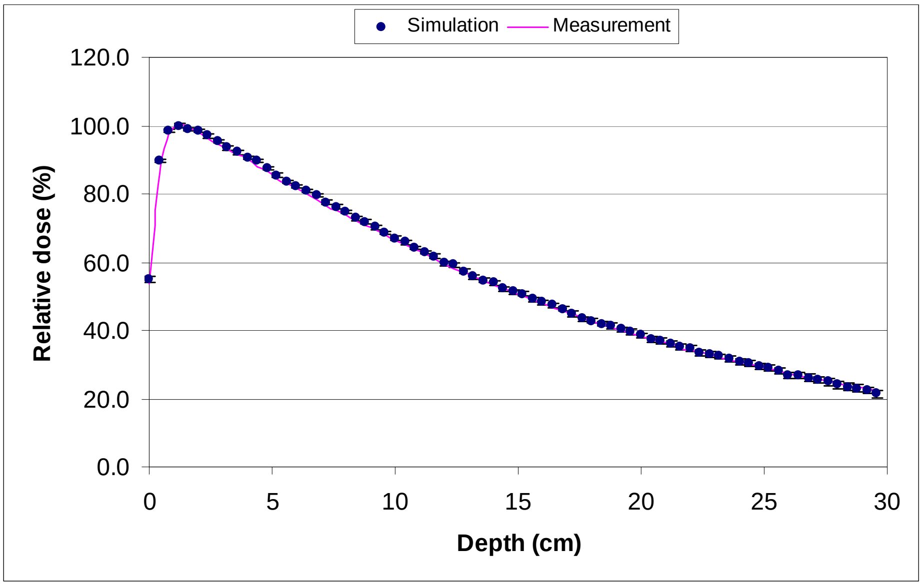

Figure 6.9. PDD curves comparing the Monte Carlo simulation and measurement in the water phantom for 10 x 10 cm^2 radiation field.

Figure 6.10 compares the cross-plane dose profiles calculated with the DOSXYZnrc Monte Carlo user code to the measurement data. The curves agree within 1% in the central region and within 3% or 2 mm in the high dose gradient region.

6.3.2 Asymmetric (half-blocked) field

Figure 6.11 presents a comparison between measured and Monte Carlo simulated profiles at 10 cm depth for asymmetric (half-blocked) field. The agreement between the measurements and calculation is within 1.5%.

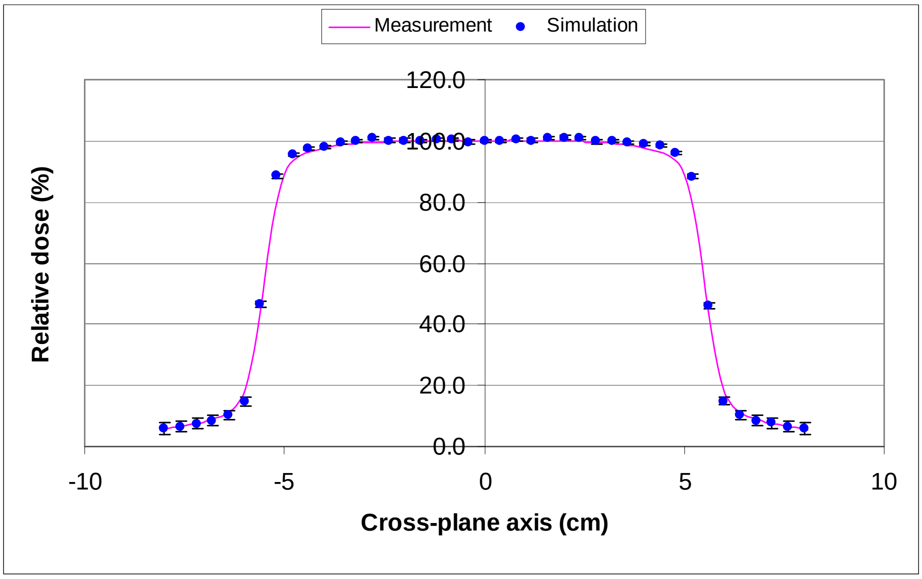

Figure 6.10. Cross-plane profiles comparison of the Monte Carlo simulation and measurements in the water phantom at 10 cm depth for 10 x 10 cm^2 field size.

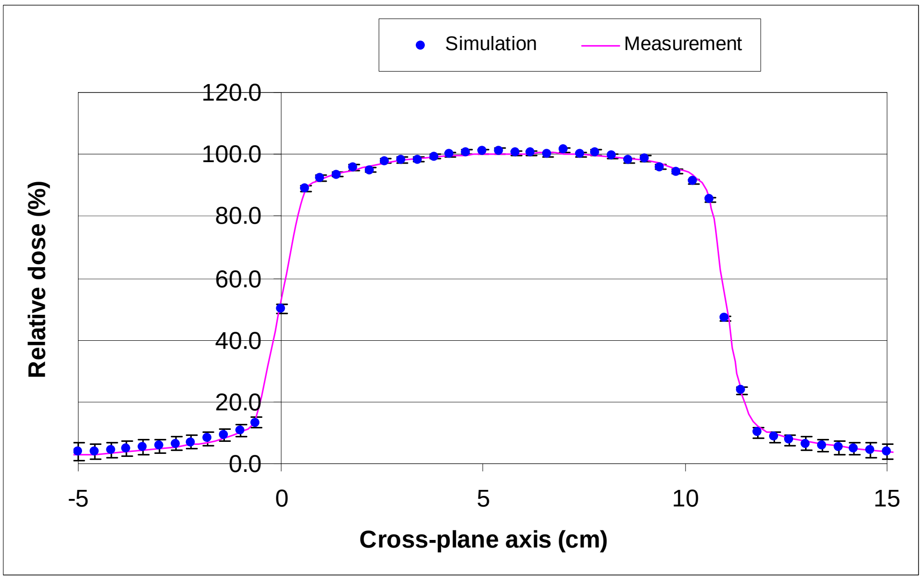

Figure 6.11. Cross-plane profiles comparison of the Monte Carlo simulation and ion chamber measurement in the water phantom at 10 cm depth for a half-blocked field.

6.3.3 MLC field

Measured dose profiles at the depth of maximum dose (1.4 cm) along the leaf axis (SSD = 100 cm) were compared with Monte Carlo simulations and are shown in Figure 6.12. The percentage difference between measurements and Monte Carlo calculations is within 2%, or within 2 mm in the region of high dose gradient. This shows that the MLC leaf position is accurately modelled.

6.3.2 Wedged field

The PDD curves were normalized to the depth of maximum dose ($d_{max} \approx 1.4$ cm for 6 MV photon beam) with the source to surface distance (SSD) equal to 100 cm. Figure 6.13 shows the calculated and measured depth dose curves for 10 x 10 cm^2 field size and 15^0 physical wedge. The relative error of the calculated dose for all depth bins is < 1%. Measured and calculated percentage depth dose were in agreement with about 0.7%. Figures 6.14-6.17 present comparisons of the plots of the profiles for 6 MV photon beams at d_{max}, 5 cm, 10 cm and 15 cm depths respectively for a 10 x 10 cm^2 field and 15^0 physical wedge. It can be seen from these figures that the Monte Carlo calculations agree with measurement within 2% or 2 mm in the high gradient region.

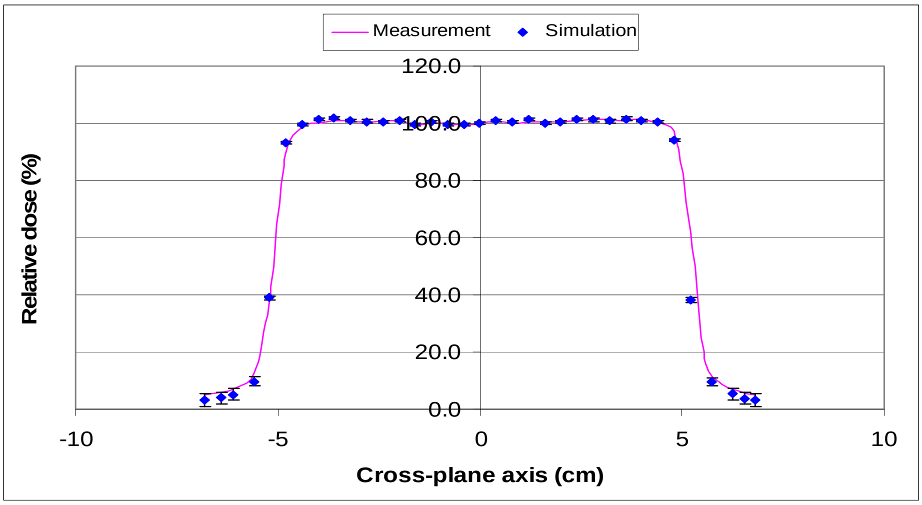

Figure 6.12. Measured and Monte Carlo simulated profiles along the leaf direction of a 10 x 10 cm^2 MLC shaped beam in water medium.

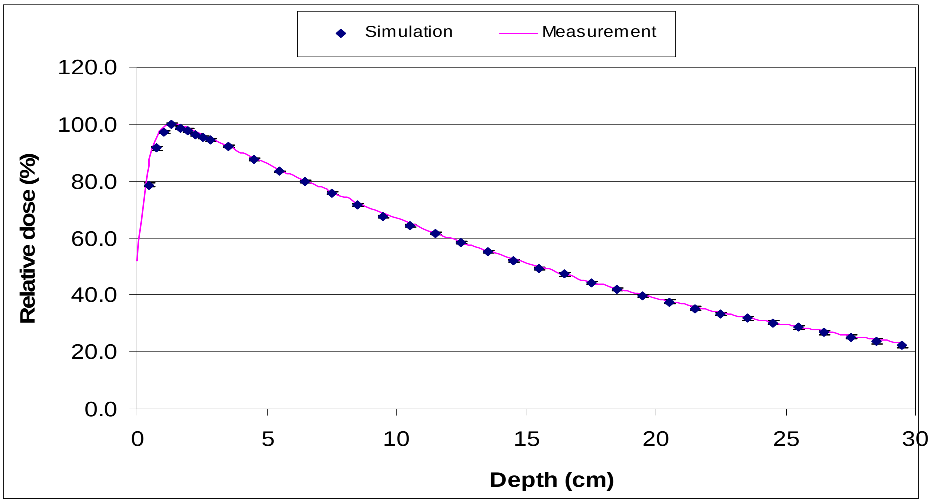

Figure 6.13. The measured and Monte Carlo simulation PDD curves for a 10 x 10 cm^2 field in water with a 15^0 physical wedge.

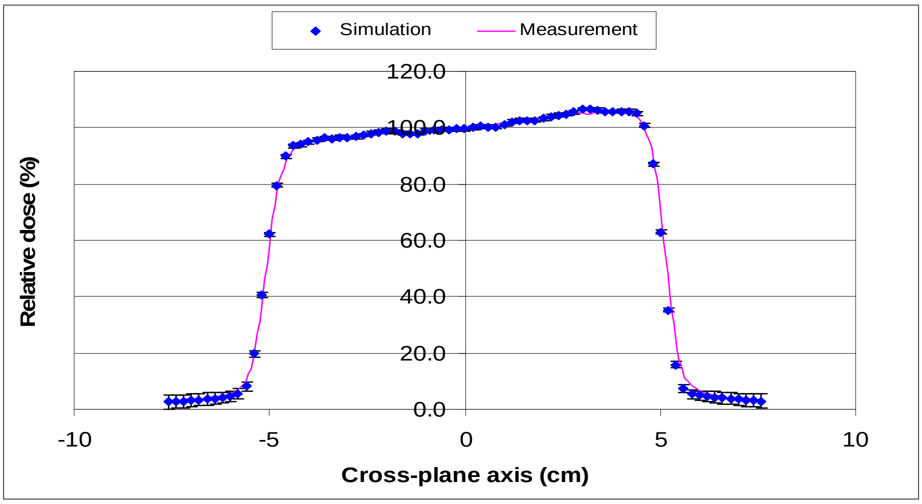

Figure 6.14. The measured and Monte Carlo simulation data for a 10 x 10 cm^2 field in water with a 15^0 physical wedge at d$_{max}$.

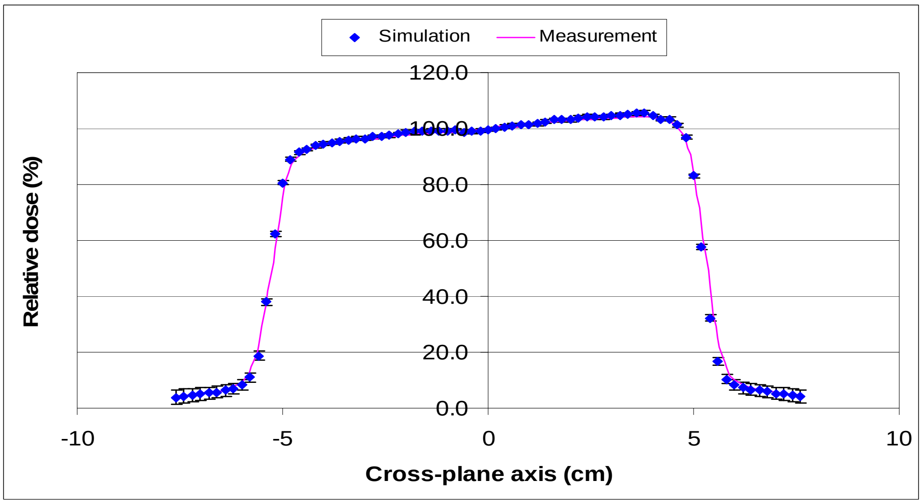

Figure 6.15. The measured and Monte Carlo simulation data for a 10 x 10 cm^2 field in water with a 15^0 physical wedge at 5 cm depth.

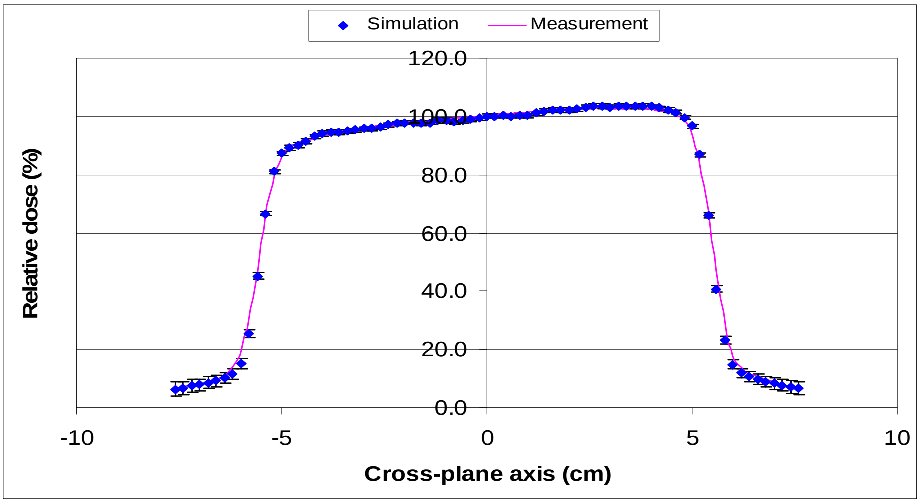

Figure 6.16. The measured and Monte Carlo simulation data for a 10 x 10 cm^2 field in water with a 15^0 physical wedge at 10 cm depth.

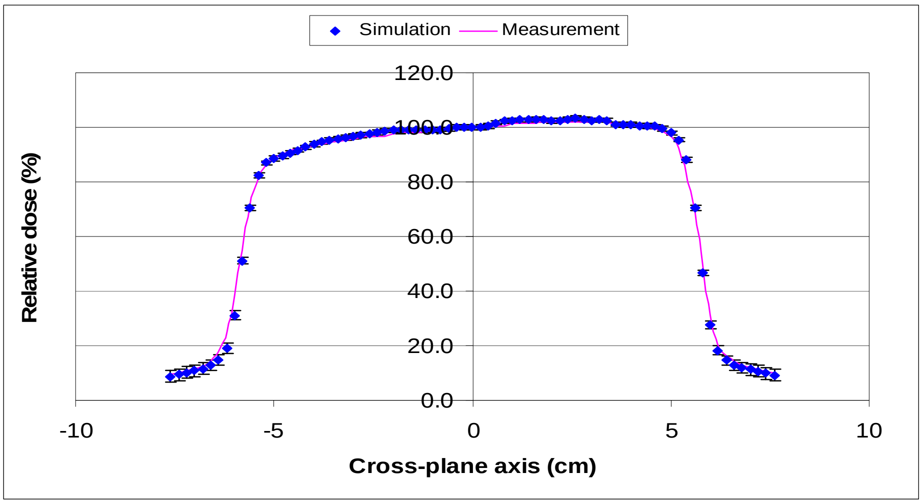

Figure 6.17. The measured and Monte Carlo simulation data for a 10 x 10 cm^2 field in water with a 15^0 physical wedge at 15 cm depth.

The PDD curves for the Monte Carlo simulated 30^0 wedge were in agreement with the measured PDD within 1% or better, see Figure 6.18. The Monte Carlo calculated cross-plane profiles at 5 cm and 10 cm depths were compared respectively with the measurements in Figures 6.19-6.20, showing an agreement within 2% away from the penumbra region. There is slight difference at the edges due to the volume of the chamber averaging at the high dose gradient region.

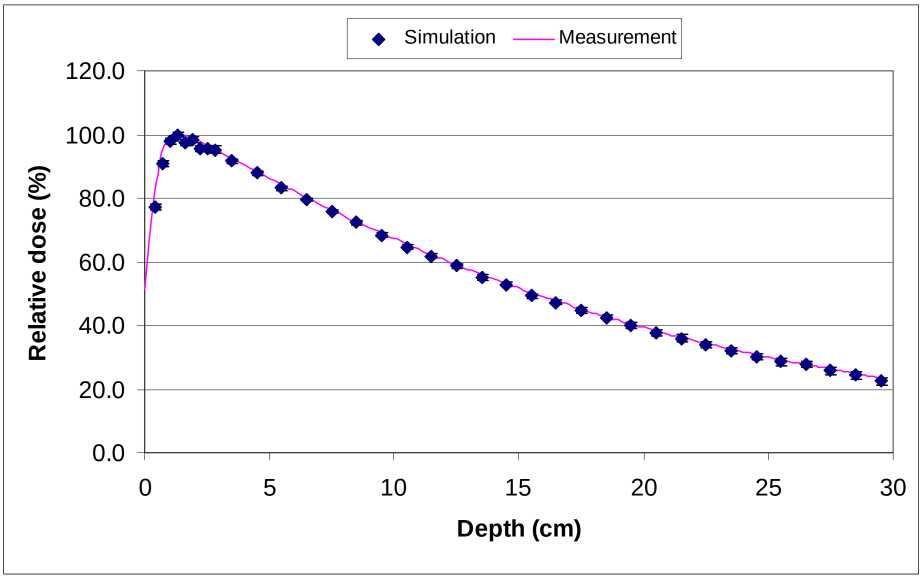

Figure 6.18. The measured and Monte Carlo simulation PDD curves for 10 x 10 cm^2 field in water with a 30^0 physical wedge.

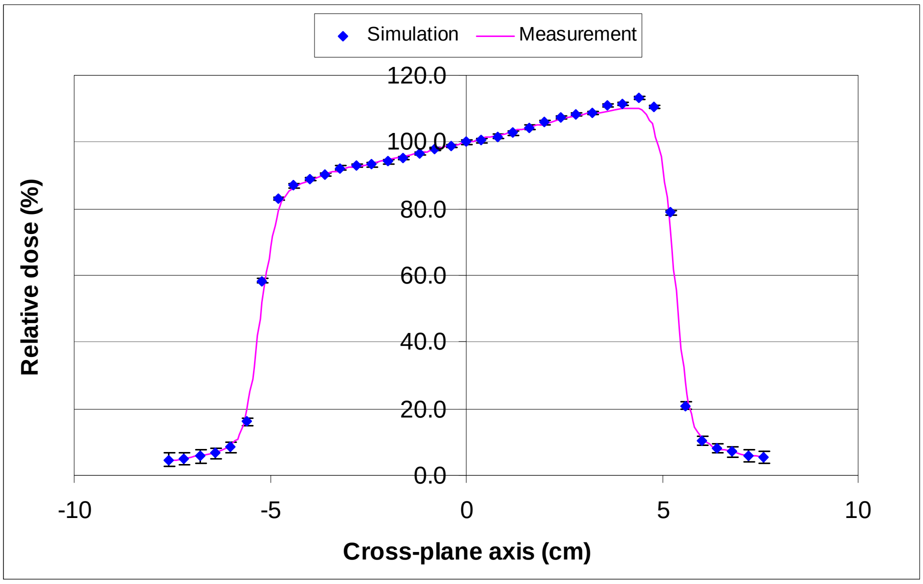

Figure 6.19. The measured and Monte Carlo simulation data for a 10 x 10 cm^2 field in water with a 30^0 physical wedge at 5 cm depth.

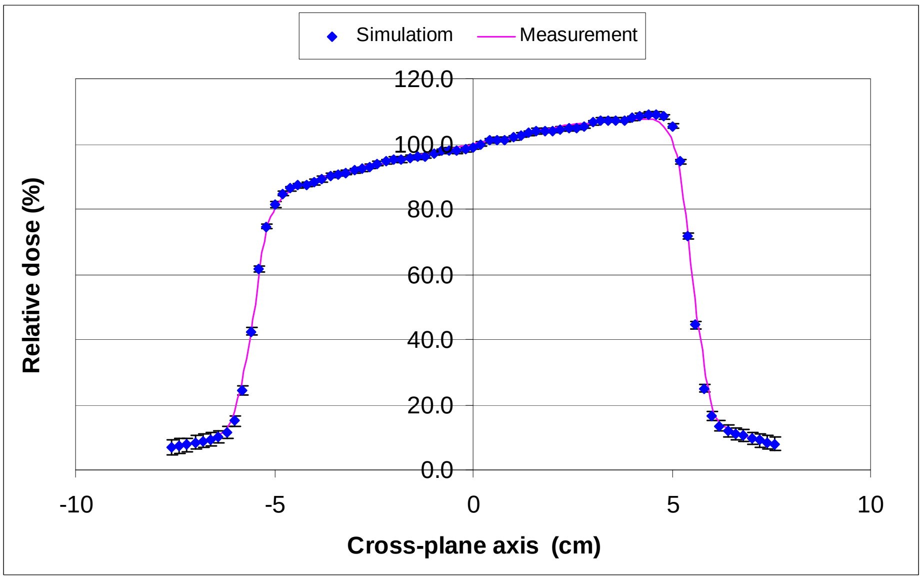

Figure 6.20. The measured and Monte Carlo simulation data for a 10 x 10 cm^2 field in water with a 30^0 physical wedge at 10 cm depth.

Figure 6.21 presents a comparison of the Monte Carlo simulations with measurements for a 45^0 physical wedge. Measured and computed percentage depth dose curves are in agreement to within better than 1%. The presence of the physical wedge causes the attenuation of low energy x-ray. This is known as beam hardening. To demonstrate the effects of beam hardening due to the presence of a physical, the PDD curve for the open field was included in Figure 6.21. Figure 6.22 shows a good agreement between Monte Carlo calculations and measurement for a 45^0 physical wedge cross-plane profile. A comparison is also made for cross-plane profiles at 5 cm and 10 cm depths for a 60^0 physical wedge. It is seen from Figure 6.23 and Figure 6.24 that the Monte Carlo simulations agree with measurement within 2% away from the high dose gradient region (penumbra).

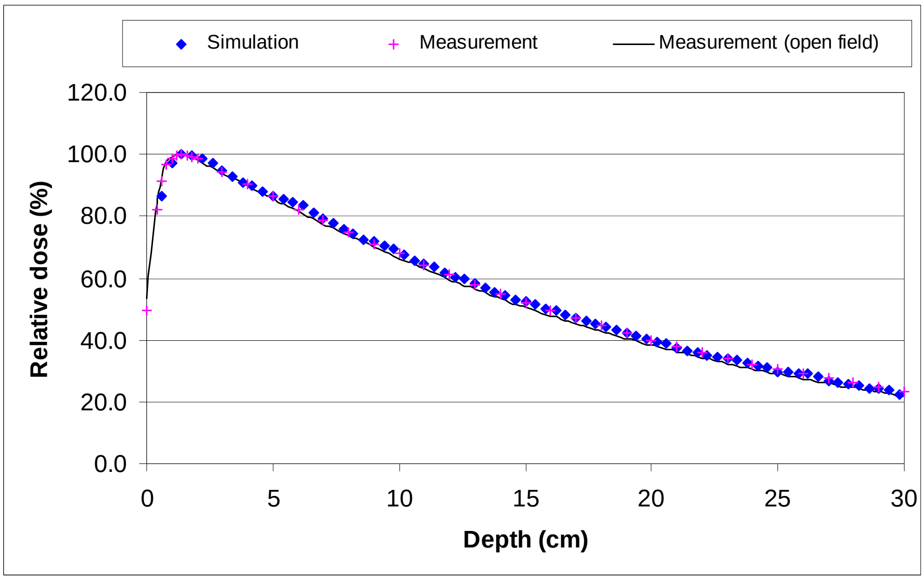

Figure 6.21. The measured and Monte Carlo simulation PDD profile for a 10 x 10 cm^2 field in water with a 45^0 physical wedge.

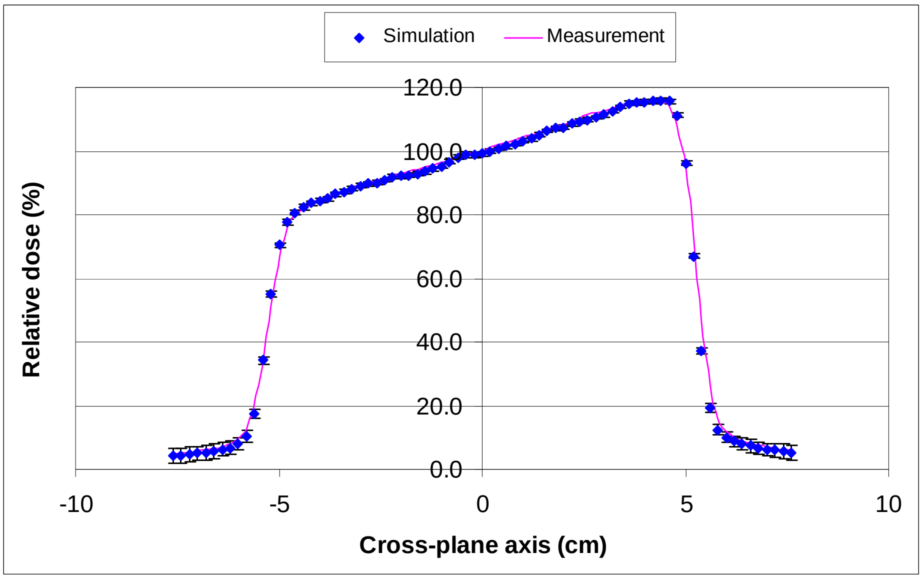

Figure 6.22. The measured and Monte Carlo simulation data for a 10 x 10 cm^2 field with a 45^0 physical wedge at 5 cm depth in water.

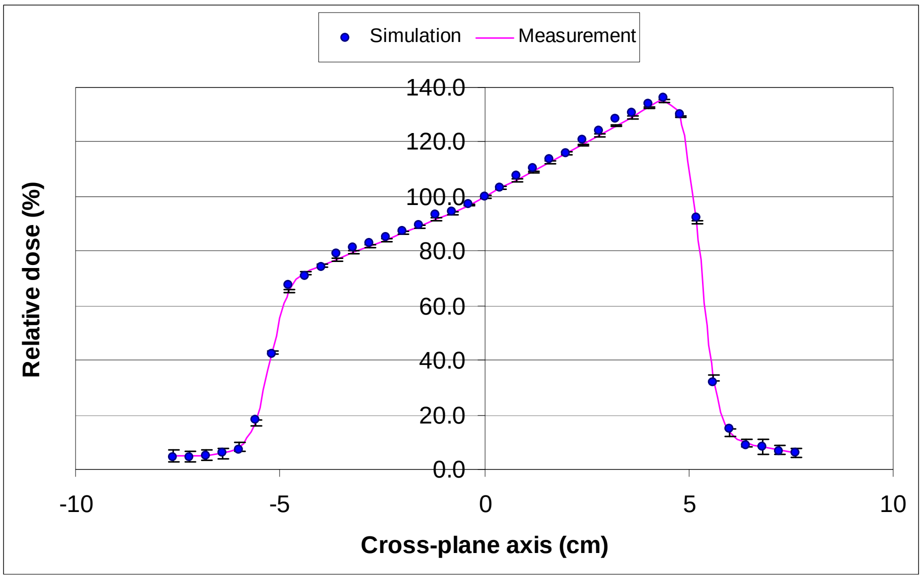

Figure 6.23. The measured and Monte Carlo simulation data for a 10 x 10 cm^2 field with a 60^0 physical wedge at 5 cm depth in water.

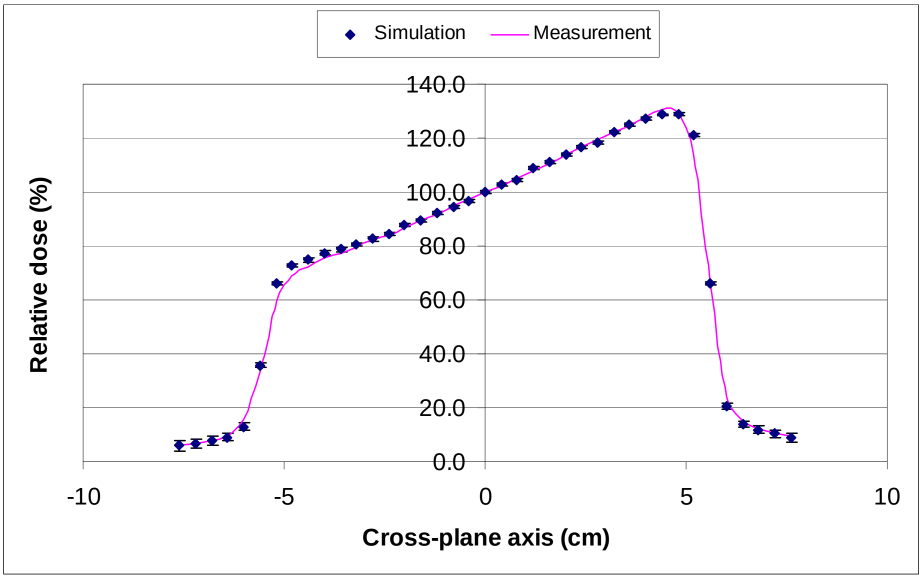

Figure 6.24. The measured and Monte Carlo simulation data for a 10 x 10 cm^2 field with a 60^0 physical wedge at 10 cm depth in water.

6.4 Conclusion

In this chapter, the BEAMnrc user code was used to model a Varian 600 C/D linac producing a 6 MV photon beam. The Monte Carlo model included open field, asymmetric field, MLC-shaped square field and wedged fields with various wedge angles. The linac model was built and verified against experimental data to ensure that the model is producing accurate results. Depth doses and beam profiles obtained during commissioning of the Varian 600 C/D linac were compared with Monte Carlo simulated depth doses and profiles.

The results showed that the dose differences between measurements and Monte Carlo simulations were less than 1% for depth doses, and within 2% for dose profiles inside the 80% field size (the region of low dose gradient). This demonstrated that the simulated phase space data were reliable and could be used for clinical patient dose calculations for future investigations. In the next chapter, the constructed linac model will be used to simulate clinical cases of breast cancer patients treated with lateral and medial tangential fields.

Chapter 7

Combined dose distributions for MammoSite breast brachytherapy and external beam whole breast irradiation

7.1 Introduction

The standard approach to breast conservation therapy for early stage breast cancer is the surgical removal of the primary breast tumour followed by whole breast radiotherapy. External beam radiation therapy (EBRT) is delivered daily to the whole breast over five weeks. To cover the entire breast volume, EBRT is delivered using 2 opposed high-energy x-ray beams, tangentially to the chest wall. At our centre, during the EBRT procedure a total of 50 Gy is generally prescribed to the isocentre, at 2 Gy per fraction daily over a 5 week period following the departmental protocol [3].

For some patients with early stage breast cancer, different radiation treatment modalities can be combined to prevent the risk of tumour recurrence. At our institution, patients with early stage breast cancer were treated with the combination of external beam radiotherapy and MammoSite brachytherapy (MB). The MammoSite brachytherapy was used as a boost delivering an additional 9-10 Gy to the tumour bed (at 10 mm from the balloon surface) in two fractions of 4.5-5 Gy at least 6 hours apart [2]. The choice of the boost technique depends on the site of the tumour bed and the thickness of the surrounding breast tissue [128].

For EBRT at our centre, the treatment plan is generated using the Pinnacle^3 treatment planning system (v6.26, Philips Medical Systems). The three-dimensional treatment planning process begins with acquisition of a computed tomography dataset (CT) using a Philips CT simulator. The CT data is transferred to the Pinnacle^3 planning server where planning target volumes and organs at risk are defined. The Pinnacle^3 treatment planning system makes use of a collapsed cone convolution/superposition algorithm for photon dose calculations [129]. In general terms, this class of algorithm calculates deposited dose by convolving a pencil beam dose kernel, obtained with Monte Carlo simulations in a water phantom, with the inhomogeneous patient dataset. The machine specific dose deposition kernel is based on a determination of the energy spectrum of the linac when operating at a given energy. This energy spectrum is determined using inverse optimization from data measured in water with the linac beam.

At our institution, high dose rate (HDR) Brachytherapy treatment planning is performed with Nucletron's Plato treatment planning system (Plato BPS v14.3.2, Nucletron B-V., Veenendaal, The Netherlands). Plato is run on a Unix-based Silicon Graphics (Silicon Graphics, Mountain View, CA) computer. Plato generates treatment plans for the Nucletron microSelectron-HDR remote afterloading unit. The HDR source is Ir-192. In Plato, treatment plans can be based on the information provided from either: (a) digitising in radiographs of the patient or (b) loading in CT scans of the patient. In each case the user identifies and inputs the positions of treatment catheters, source positions and dose calculation points. In addition CT based plans allow for 3D volumes to be created. Source positions can be manually or automatically placed within the catheters. For automatically placed source positions the dose algorithm can determine the best positions to place sources within the catheters in order to deliver the desired dose distribution. In addition to the source positions the dose algorithm determines the dwell times (i.e. length of time the source stops at a particular source position) for each source position. Plato calculates dose using a 3D dose algorithm based on AAPM Task Group 43 recommendations [37].

It would be beneficial (to the oncologist) to visualize the final (combined) dose distributions from the two modalities to assist with an assessment of treatment plans and the treatment outcome. Currently, combining the dose distributions from the two modalities is difficult to achieve because the two modalities use different planning systems and different dose calculations algorithms and the patient anatomy looks different (balloon is present for brachytherapy). In this chapter, two separate Monte Carlo simulations were constructed to simulate the dose distributions for external beam radiotherapy and MammoSite brachytherapy using patient CT images. A technique was also developed to combine the final dose distributions from the two modalities.

7.2 Materials and methods

7.2.1 Monte Carlo simulation of EBRT treatment

Initially, the Pinnacle^3 treatment planning system was used to develop external beam radiotherapy treatment plans using patient CT images. CT images for the MammoSite treatment were used for EBRT as well at this stage. This particular simplification allowed us to combine the dose distributions on a voxel-by-voxel basis, without the need to consider anatomical changes between the two modalities.

Details of the treatment setup for EBRT are shown in Table 7.1. The treatment plan consisted of two opposed wedged tangential fields (medial and lateral). The field size was chosen to cover the whole breast. Figure 7.1 shows the treatment set up. To account for the breast shape wedges were used to compensate for missing tissue. Multi-leaf collimators (MLCs) were also used to shape the beam to avoid radiation over-dosage to normal tissues.

Table 7.1. Summary of the whole breast external beam irradiation treatment plan.

Beam setup	Medial field		Lateral field	
Energy (MV)	6		6	
Gantry angle	305^0		131^0	
Lower jaws (cm)	X1	X2	X1	X2
	8.0	8.0	8.0	8.0
Upper jaws (cm)	Y1	Y2	Y1	Y2
	10.0	8.0	10.0	8.0
Blocks	MLC		MLC	
Wedge	15^0, up right		15^0, up left	
SSD (CM)	90.62		91.57	

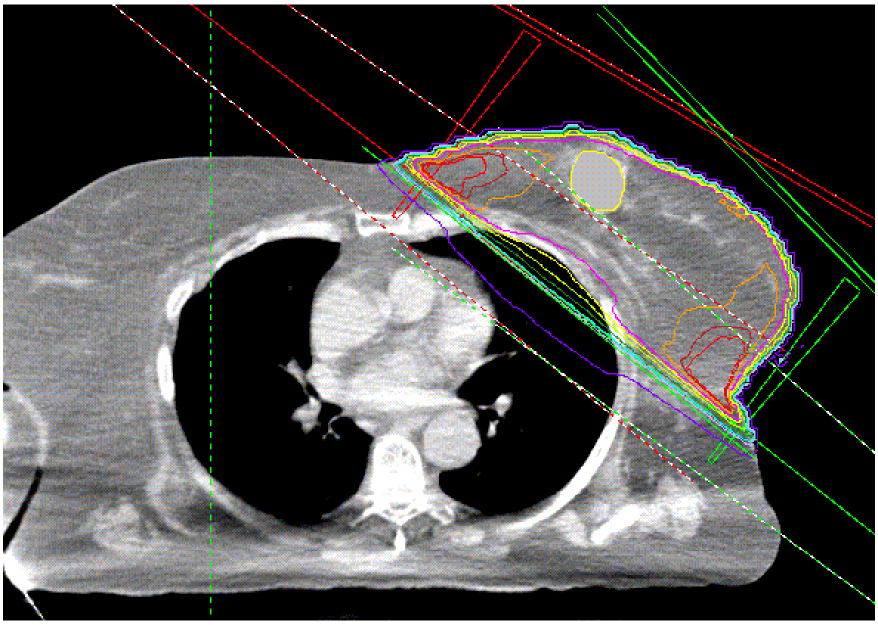

Figure 7.1. Standard external beam breast radiotherapy treatment plan. Two physical wedges are placed in the beam to compensate for missing tissue in order to achieve a conformal dose distribution throughout the irradiated breast.

The BEAMnrc Monte Carlo code was used subsequently to simulate a 6 MV Varian 600 C/D linac treatment head set up using the information from Table 7.1. The steps involved in simulating the linac treatment head were previously discussed in Chapter 2. Figure 7.2 summarizes the steps involved in the Monte Carlo modelling of the machine configuration for the given patient treatment plan. The positions of the MLCs were copied from the treatment plan and used in the Monte Carlo model. Figure 7.3 presents the shape of the MLCs model for the medial and lateral fields. The setup of the Monte Carlo model (medial field) is described in detail in Appendix D.

Up to 9 x10^7 electron histories were simulated to produce a phase-space data file below the physical wedge. The size of the phase-space data file was 5.9 Gigabytes for each linac treatment field model. It took 72 hours of simulation time. The phase space files, produced by the BEAMnrc simulations, were used for dose calculations using DOSXYZnrc. An input file for the DOSXYZnrc simulation is shown in Appendix D.

The CT images of a patient with the MammoSite balloon were imported to EGSnrc Monte Carlo system code. The CT images were converted to tissue data using the user code CTCREATE (as discussed in Chapter 2, Section 2.4.1.2). During the conversion, the CT dataset was clipped to remove some data not required for patient dose calculations. The air around the patient was clipped to reduce the volume of the CT data irrelevant to the simulation to reduce simulation time. The converted tissue data contained information such as CT number, electron density and voxel dimensions. A voxel size of 1.5 mm^3 was used for calculations.

For the simulation of EBRT, the patient’s left arm was removed to simulate the realistic patient position during treatment with arms raised above the head so that the lateral field didnot pass through the arm. While the balloon was left in place, the density of the balloon was set to that of the breast tissue. In a clinical situation, however, the balloon is never used as the EBRT treatment commences before the MB treatment.

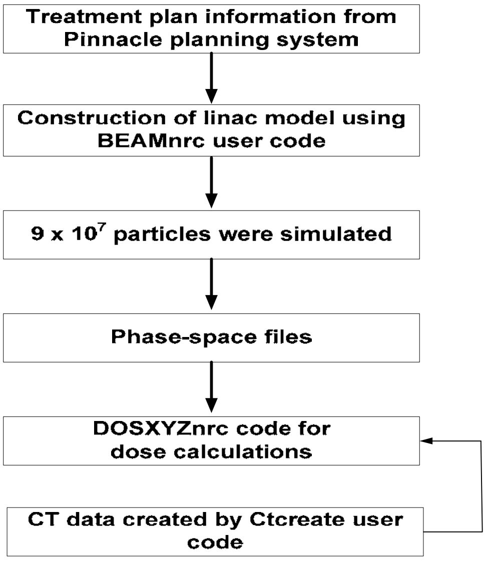

Figure 7.2. Summary of the steps involved in the construction of a linac model using BEAMnrc.

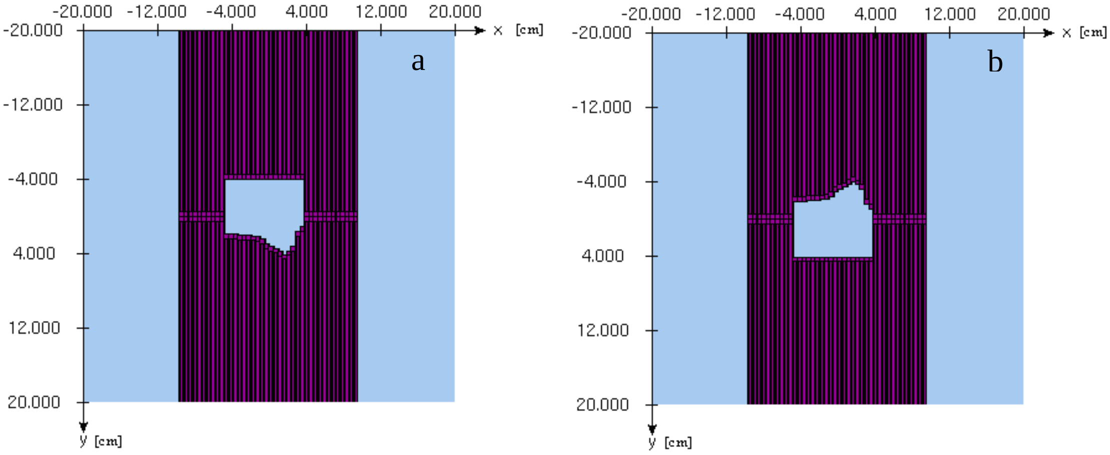

Figure 7.3. MLC shaping for (a) the medial, and (b) the lateral fields treatment plans.

7.2.2 Validation of EBRT model

The Monte Carlo model for the external beam radiotherapy was validated against the Pinnacle^3 planning system and measurements. For simplicity, in the Pinnacle^3 simulation the CT phantom was replaced by a water phantom and the dose was calculated for the medial field as planned. A 2D dose matrix was extracted at the isocentre plane. The 2D dose matrix was used for comparison with the Monte Carlo simulation. Similarly, the Monte Carlo simulation was performed in a water phantom for the medial field as well. A 2D dose map was extracted from the three dimensional Monte Carlo dose output using in-house developed Matlab code at the same plane as Pinnacle^3.

Further validation of the Monte Carlo model against measurement was also carried out. The measurement was conducted using the Mapcheck instrument (Sun Nuclear Corporation, Melbourne, FL, USA). Mapcheck is a 2 dimensional array of diode detectors used for dose plan verification of radiotherapy and intensity modulated radiotherapy (IMRT) treatments (see Figure 7.4). It has a total of 445 individual detectors spaced at 1 cm in the central 10 x 10 cm^2 field and at 2 cm in the outer section of the field. The total detecting area is 22 cm x 22 cm. On top of the detectors is a layer of plastic giving 2 g/cm^2 water equivalent build up.

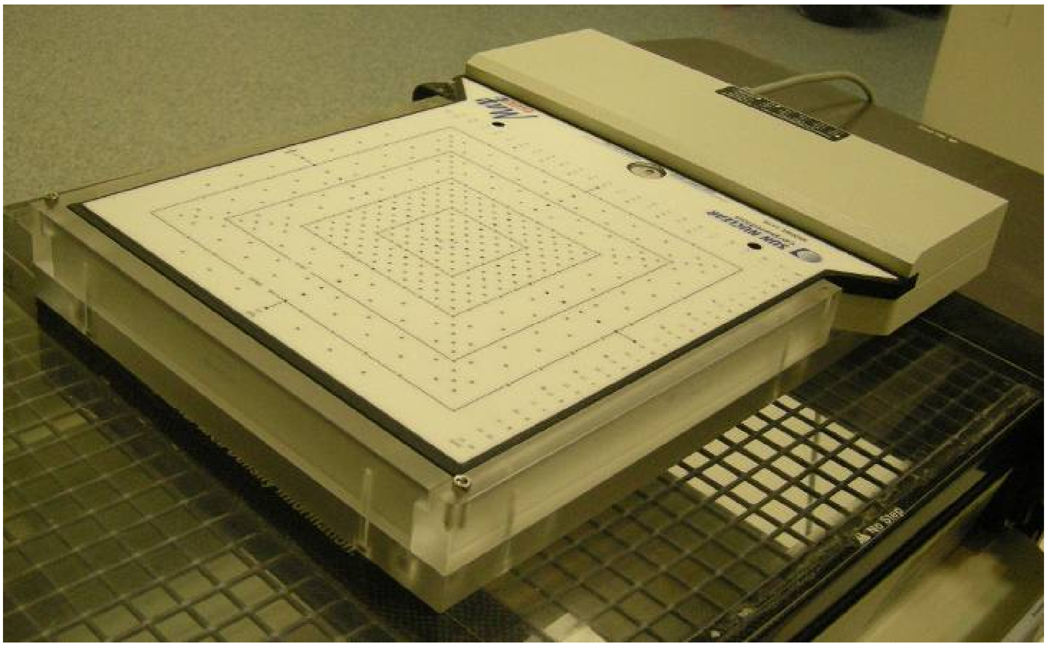

Figure 7.4. Mapcheck (Sun Nuclear Corporation) 2 dimensional detector for verification of radiotherapy dose distributions.

To deliver a treatment field (medial tangential field) on a linear accelerator, the patient plan must first be exported from the Pinnacle^3 treatment planning system to the record and verify (R&V) system which interfaces with the linac hardware. Our institution uses Aria (Varian Oncology Systems, Palo Alto, CA) as the R&V system. The test patient plan was loaded onto the treatment console, ready for delivery to the Mapcheck unit.

For the measurement, Mapcheck was placed on the treatment couch with the detector array located at 100 cm SSD as defined by the lasers in the treatment room. Prior to measurements, the Mapcheck detectors were calibrated for both relative and absolute measurements. For relative calibration the Mapcheck unit is irradiated with a large, 25 x 25 cm^2 treatment field and rotated on the couch through 180 degrees so that the sensitivity of individual detectors can be equalized. This is performed using the step by step procedures in the Mapcheck software. For absolute calibration, a known dose was delivered to Mapcheck in reference conditions and the absolute dose value delivered was assigned to the central detector of the array.

Once calibrated, the Mapcheck was centred in the cross hairs of the linac light field and the medial tangential field was delivered. The two-dimensional dose map recorded by Mapcheck was saved for analysis.

The Gamma function algorithm is the most commonly used method for comparison of measured and planned dose distributions, and it was proposed by Low et al [130, 131]. Using the γ-function method the Mapcheck software computes a gamma index: a unitless value used for comparison between the measured and calculated dose maps. The gamma index, $\gamma(r_r)$ is defined as the minimum of the gamma function, $\Gamma(r_r, r_e)$ for a measured point at position r_r and a calculated point at position r_e. They are expressed mathematically as follow:

$$\gamma(r_r) = \min\{\Gamma(r_r, r_e)\}\forall\{r_e\}, \tag{7.1}$$

where:

$$\Gamma(r_r, r_e) = \sqrt{\frac{r^2(r_r, r_e)}{\Delta d_M^2} + \frac{\delta^2(r_r, r_e)}{\Delta D_M^2}}, \tag{7.2}$$

$r(r_r, r_e) = \left|r_e - r_r\right|$, and $\delta(r_r, r_e) = D_e(r_e) - D_r(r_r)$.

$r(r_r, r_e)$ is the distance between the measured and computed points at r_r and r_e respectively and $\delta(r_r, r_e)$ is the dose difference between them. Δd_M and ΔD_M are the distance-to-agreement and the dose difference acceptance criteria respectively. Typical values of Δd_M and ΔD_M are generally 3 mm and 3% respectively [131, 132]. In the current study, the values of Δd_M and ΔD_M were set to 2 mm and 2% respectively so that an excellent agreement is obtained between measurements and Monte Carlo simulation. This will give us a good level of confidence in constructed Monte Carlo model.

When the two dose maps are compared, each pixel or measurement point is evaluated for its γ value. If the gamma index value is less than or equal to one, the investigated point passes the criteria. If the gamma index is greater than 1, the point fails. The gamma index is represented mathematically as follow:

$$\gamma(r_r) = \begin{cases} \leq 1, & passed \\ > 1, & failed \end{cases} \tag{7.3}$$

To enable the gamma comparison, the Monte Carlo data had to be imported into the Mapcheck software. This was achieved by copying the header and data structure of a planned data file that was previously imported from Pinnacle^3 into Mapcheck and replacing the data points in this file with the data generated by Monte Carlo. Once imported, the calculated data can be easily compared to the measured data using the software. The gamma comparisons were made with 2 mm distance and 2 % dose parameters and the detector points that fail the gamma comparison are highlighted either as blue (for under-dose) or red (for over-dose).

7.2.3 Monte Carlo simulation of MB treatment

As mentioned before, the same CT dataset was used for brachytherapy modelling. In the simulation of the MB treatment plan, the dose distribution was calculated using the DOSXYZnrc used code. The modelled ^{192}Ir source was placed at the centre of the balloon with its axis aligned with the balloon axis (discussed in Chapter 3). The voxel size for the Monte Carlo dose simulation was 1.5 mm^3. The simulation was run with up to 2 x10^8 particles, resulting in statistical error of less than 2% at 1 cm from the balloon surface. The required CPU running time was approximately 25 h.

7.2.4 Dose combination of MB and EBRT

Combining the dose distributions from the two modalities is not a straightforward task due to the differences in delivery mode, fraction size, dose rate and energy associated with each modality. Since these differences greatly influence the biological effectiveness, the concept of equivalent dose makes it possible to combine the final two dose distributions. In order to add the two dose distributions together, a standard reference modality needs to be selected for the calculation of the equivalent dose (D_{eq}). Therefore, in this study D_{eq} was calculated with respect to that for EBRT in 2 Gy fractions using the following equation [89]:

$$D_{eq} = \frac{BE_{ff}D}{1 + \frac{d_{ref}}{\alpha / \beta}}, \tag{7.4}$$

In equation (7.4), $BE_{ff}D$ is the biological effective dose, d_{ref} = 2 Gy is the reference dose per fraction for a conventionally fractionated EBRT treatment schedule and α/β are radiosensitivity coefficients (defined in Chapter 4). The α/β ratio for breast cancer was set to 10 Gy [111].

The Monte Carlo simulations produce three dimensional dose distribution data files which were used for data analysis. An in-house developed Matlab code (see Appendix B) was used to extract 2 dimensional dose distribution matrices for the different simulation runs. For EBRT simulation, the two dimensional dose distributions were extracted for the medial and lateral tangential fields at the isocentre planes (X_{iso}, Y_{iso}, Z_{iso}). The coordinates for the isocentre plane were obtained from the Pinnacle^3 treatment planning system. The two planes were then added together to produce a final planar dose distribution matrix for EBRT. The combined dose matrix was normalized to the isocentre point dose (X_{iso}, Y_{iso}). A normalization factor was then applied to the combined dose matrix so that the EBRT delivered a total physical dose of 50 Gy during the treatment course.

The biological effective dose ($BE_{ff}D$) was calculated by multiplying the total physical dose (TD) by a relative effectiveness factor (RE) using equation 4.1 described in Chapter 4 which is reproduced here [90]:

$$BE_{ff}D = TD \times RE, \tag{7.5}$$

The $BE_{ff}D$ formula employed for clinical applications in external beam fractionated radiotherapy is given by:

$$BE_{ff}D = TD \times (1 + \frac{d}{\alpha / \beta}), \qquad (7.6)$$

where *TD* is the total dose delivered over the course of treatment and d is the dose per fraction. The relative effectiveness (*RE*) is the factor in the parentheses.

$$RE = (1 + \frac{d}{\alpha / \beta}), \qquad (7.7)$$

For the EBRT matrix, no further conversions were necessary because the equivalent dose formula was based on 2 Gy fraction as commonly used for external beam treatment. By fitting equation 7.6 into equation 7.4 above, the equivalent dose for EBRT is given by:

$$D_{eq}(EBRT) = TD, \qquad (7.8)$$

For the MammoSite simulation, the two dimensional distribution matrix was extracted at the same plane as that of EBRT. The dose was then normalized to an isocentre point (X_{iso}, Y_{iso}). A normalization factor was applied using a dose of 10 Gy for the MammoSite as a boost.

To combine the final dose distributions from the two modalities, the concept of biological effective dose and equivalent dose were employed. The two dimensional dose distribution matrix, from the MammoSite treatment, was first converted to a two dimensional biological effective dose matrix by applying the relative effectiveness factor. The two dimensional based biological effective dose matrix was then converted into a two dimensional equivalent dose matrix using equation 7.4.

The 2 dimensional based equivalent dose distribution matrices were calculated for EBRT and MB and finally summed up pixel by pixel using the following relation:

$$TD(X_i, Y_i) = D_{eq,EBRT}(X_i, Y_i) + D_{eq,MB}(X_i, Y_i) \qquad (7.9)$$

7.3 Results

The 2D dose maps calculated by the Pinnacle^3 planning system were compared with the Monte Carlo dose maps. Figure 7.5 shows the planar dose distribution calculated by Monte Carlo simulation and the Pinnacle^3 treatment planning system. Monte Carlo dose Matrix was subtracted from the Pinnacle^3 dose matrix. The percentage difference between the Monte Carlo computed dose and Pinnacle^3 dose is less than 3% even in the region of high dose gradient, and less than 0.5% within the field (i.e. 90% isodose line) as shown in Figure 7.6. This agreement proved the validity of the Monte Carlo model.

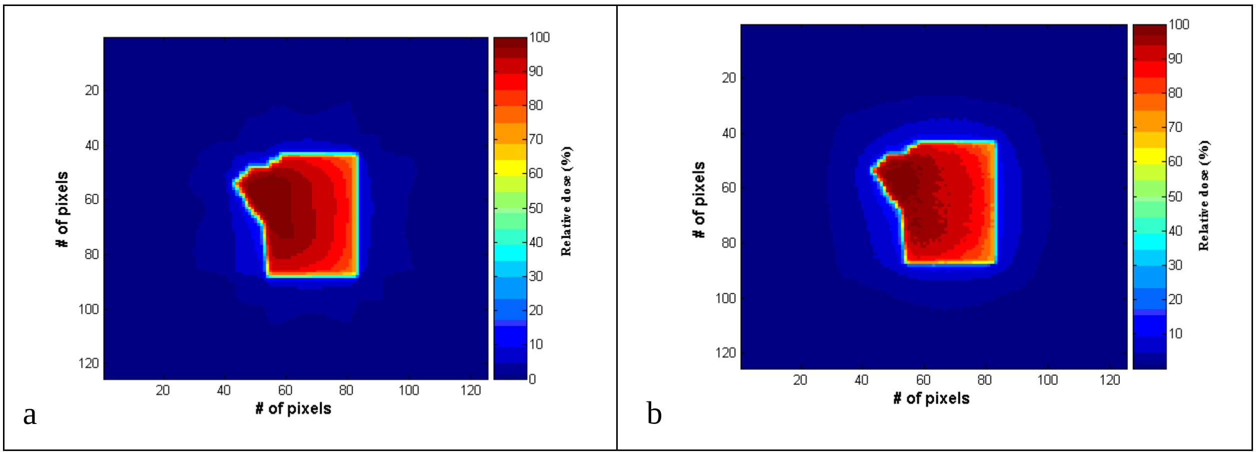

Figure 7.5. Two dimensional dose matrices extracted for the medial field from (a) the Pinnacle^3 treatment planning system and (b) Monte Carlo simulations.

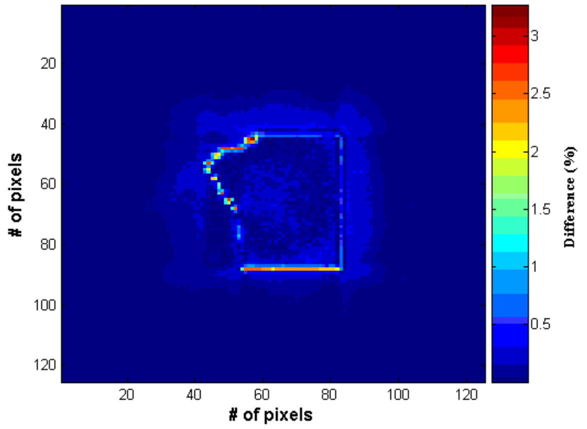

Figure 7.6. The difference between the Pinnacle^3 2 D dose matrix and Monte Carlo simulation.

The two dimensional dose maps measured by Mapcheck were compared with the calculated dose maps produced by Monte Carlo simulations. To compare the two fields the

Mapcheck software was used. The software can perform a gamma calculation to assess the agreement of measured and calculated doses at the location of each Mapcheck detector.

Figure 7.7 is a direct comparison between the measured relative dose (for the medial field) and Monte Carlo computed relative dose for the same field. The threshold parameter was set to 10% of dose (i.e. the tail region) as the points below this threshold have a high percentage of noise from the detector errors that may cause the points in the penumbra region to fail the 2 % and 2 mm dose criteria. This region is also of less clinical significance. 10% is the threshold commonly used with gamma comparisons in Mapcheck. It is seen that the gamma function results showed excellent agreement between the measured dose and computed Monte Carlo dose values for 2% and 2 mm criteria. As shown in Figure 7.7, the gamma analysis included a total of 338 points of which 336 passed while only 2 points failed the test. This indicated that 99.4% of the measured and calculated dose values agreed within the accepted criteria of 2% and 2 mm.

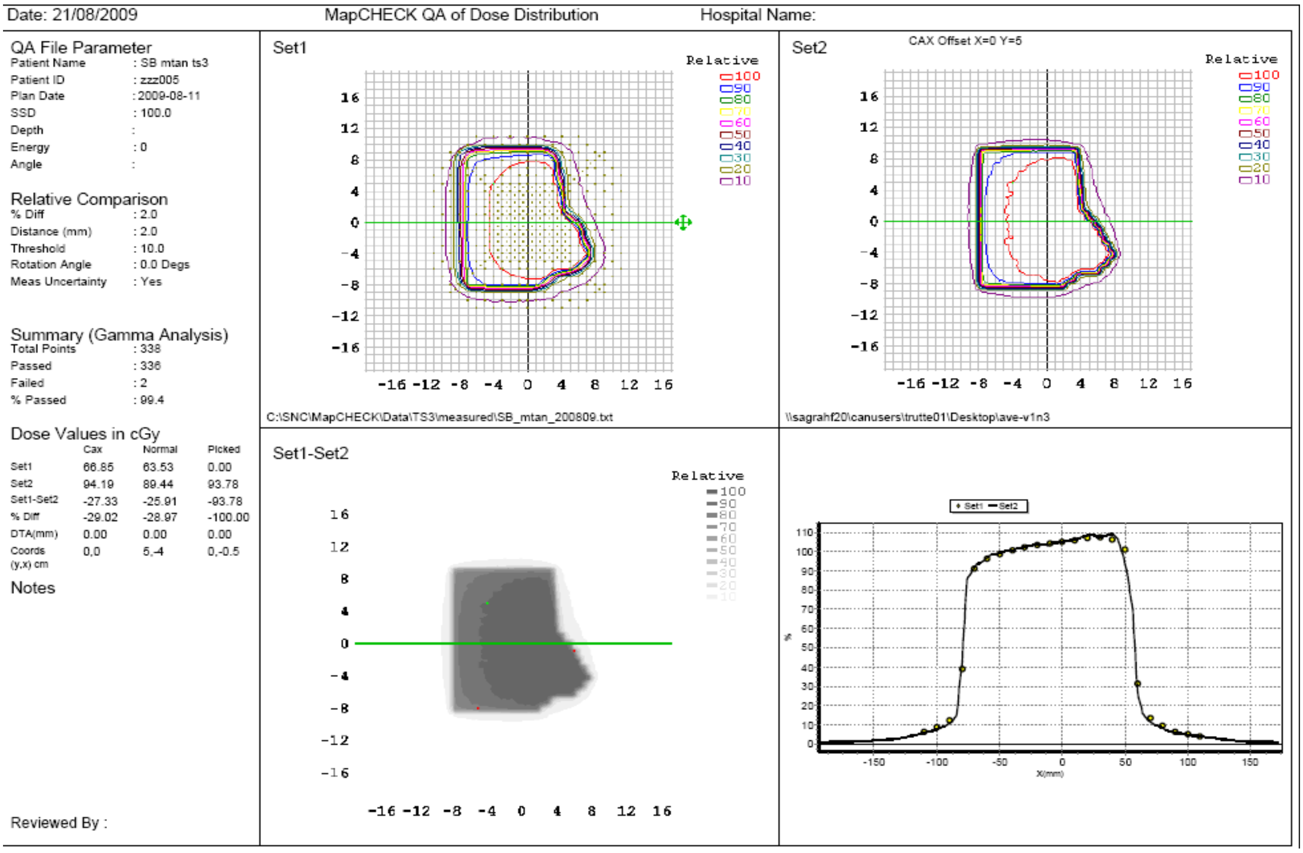
Date: 21/08/2009 MapCHECK QA of Dose Distribution Hospital Name:

QA File Parameter
Patient Name : SB mtan ts3
Patient ID : zzz005
Plan Date : 2009-08-11
SSD : 100.0
Depth :
Energy : 0
Angle :

Relative Comparison
% Diff : 2.0
Distance (mm) : 2.0
Threshold : 10.0
Rotation Angle : 0.0 Degs
Meas Uncertainty : Yes

Summary (Gamma Analysis)
Total Points : 338
Passed : 336
Failed : 2
% Passed : 99.4

Dose Values in cGy

	Cax	Normal	Picked
Set1	66.85	63.53	0.00
Set2	94.19	89.44	93.78
Set1-Set2	-27.33	-25.91	-93.78
% Diff	-29.02	-28.97	-100.00
DTA(mm)	0.00	0.00	0.00
Coords (y,x) cm	0,0	5,-4	0,-0.5

Notes

Reviewed By :

C:\SNC\MapCHECK\Data\TS3\measured\SB_mtan_200809.txt

\\sagrahf20\canusers\trutte01\Desktop\ave-v1n3

CAX Offset X=0 Y=5

Figure 7.7. Comparison between measured relative dose and Monte Carlo computed relative dose using γ algorithm in Mapcheck software. It showed that 99.4% of detectors passed the criteria of 2% (dose difference) and 2 mm (distance-to-agreement) which is acceptable in radiotherapy.

The combined dose distribution is shown in Figure 7.8. The tumour bed would receive an equivalent dose of 60 Gy. In order to obtain 3D dose distribution, the same process needed to be applied to the whole 3D dose matrices from both modalities.

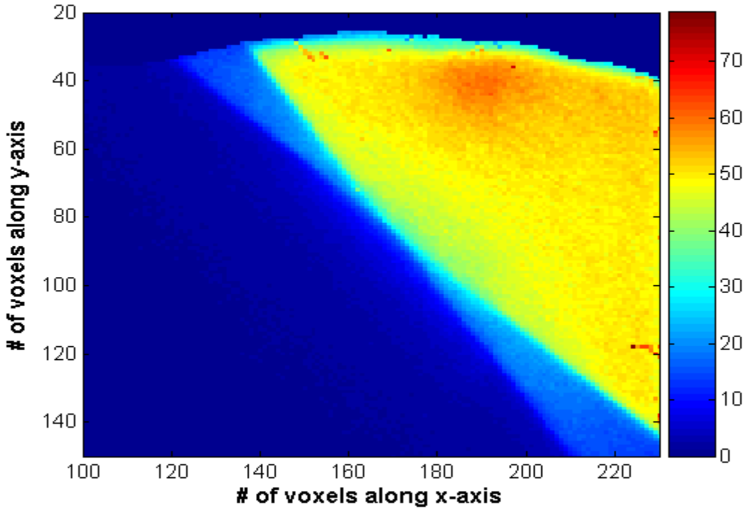

Figure 7.8. Combined dose distribution from EBRT and MB techniques.

7. 4 Discussion & conclusion

The Pinnacle[3] treatment planning system was used to generate an EBRT treatment plan, for breast cancer treatment, using the same patient CT image used for the MB. The treatment beams and the beam modifiers were modelled using the EGSnrc Monte Carlo code. Monte Carlo dose maps were compared with Pinnacle[3] dose maps and a good agreement was found of less than 3% in the high gradient region and of less than 0.5% in the low gradient region.

The Monte Carlo model was also validated against measurements taken with the Mapcheck instrument. The comparison between the two dose maps was made using the Mapcheck software. The gamma function analysis algorithm was used and the acceptance criteria for comparison were set to distance-to-agreement of 2 mm and 2% dose difference. An excellent agreement (99.4%) was found between the Monte Caro computed dose maps and the measured ones. This proved that a reliable Monte Carlo model was constructed and used for dose calculations from EBRT treatment. The simulated dose distribution from EBRT was combined with the simulated MammoSite dose distribution.

In-house developed Matlab code was used to extract two-dimensional dose matrices from the simulated three-dimensional dose distributions. The dose extraction for the MB model was made at the isocentre of the EBRT model. Normalization factors were applied to convert the dose (physical) to a clinically meaningful dose. The models of the biological effective dose and equivalent dose were employed to combine the dose distributions from the two modalities. In this study, the dose combination was done using the same CT dataset. The CT datasets had the same number of voxels and the same voxel size. Every point of one image corresponded to the same point in the other image.

However, factors were not considered when combining the dose distributions from the two modalities. They included the time gap between the EBRT and MB treatments. Also, organ deformation and other anatomical changes due to different anatomical position of tissue with (MammoSite) and without (EBRT) the balloon were not taken into account when combining the two modalities. To take such changes into account, deformable image registration (DIR) can be used for fusion of the data from the two modalities in future studies. Deformable image registration is a technique for mapping one image set onto another [133-137].

In this scenario, the two images are: a) the CT image set for EBRT treatments with no balloon inserted and b) CT image set for MammoSite treatment with the balloon applicator inserted. With a deformable image registration algorithm, all voxels in the MammoSite CT can be modified and mapped onto corresponding voxels in the EBRT CT. The dose information and isodose lines associated with the MammoSite CT will also be transferred to the EBRT CT so that the combined dose distribution from EBRT and MammoSite treatments can be accurately reconstructed for each voxel of tissue in the patient.

There are many mathematical algorithms existing in the literature for deformable image registration including algorithms based on warping of thin plate spline and B-splines [138-140], viscous fluids [141, 142], hammer [143] and demons algorithms [144, 145]. Some of these algorithms work on deformation of individual voxels with overall smoothness constraints and some use physical constraints such as elasticity of different organ structures. However, the use of the DIR method is beyond the scope of the current study.

Chapter 8

Conclusions and further work

8.1 Conclusions of the thesis

Patients with early stage breast cancer, following lumpectomy, can be treated with brachytherapy (MammoSite or interstitial) alone or external beam radiotherapy alone, or with a combination of the two modalities. The focus of the current work was to construct two separate Monte Carlo models for simulating the MammoSite brachytherapy and external beam radiotherapy treatment plans. The Monte Carlo models were applied to compute the dose distributions from the two modalities using patient CT images. Furthermore, a technique was developed to combine the dose distributions obtained from the two modalities.

In the MammoSite technique, a high dose rate ^{192}Ir source is driven into the balloon centre using a remote afterloader to deliver the prescribed dose at a plane 1 cm away from the balloon surface. There are several uncertainties that affect the dose distribution in the MammoSite brachytherapy. The first part of this work investigated the impact of uncertainties associated with the MammoSite brachytherapy on the dose distribution in the breast.

The EGSnrc Monte Carlo code was employed to model the ^{192}Ir brachytherapy source. The results of source modelling showed that the ^{192}Ir source could be modelled as a parallelepiped source using the DOSXYZnrc Monte Carlo user code.

The impact of voxel size in the Monte Carlo calculations on the accuracy of the dose distribution around the modelled ^{192}Ir was investigated. The dose was calculated with various voxels sizes. It was found that a voxel size of 1.5 mm^3 was suitable for performing Monte Carlo dose calculations, as reducing the voxel size further would not yield more information about the dose distribution and would only increase the simulation time. An in-house Matlab code was developed in this work and many of the results and the graphs were processed with this code. The developed Matlab code was useful for processing the three-dimensional dose distributions outputs computed by the EGSnrc Monte Carlo code. The source model was verified against measurements using TLD-100 chips. The TLDs were irradiated inside an in-house made breast phantom at various distances from the ^{192}Ir source. The dose fall-off as a function of distance from the source between the measured and computed data) was in excellent agreement (. The measurement uncertainty and Monte Carlo statistical error were 3% and 1.8% respectively.

The Monte Carlo simulations for the MammoSite treatment were performed using either actual CT images of a patient or CT images of an in-house tissue equivalent phantom. Since the EGSnrc Monte Carlo code does not work with individual CT slices but with the volume of datasets, a 3D CT model was generated and used in dose calculations during the study.

MammoSite treatment protocols allow for up to 4 mm balloon deformation. Uncertainties in the source positioning and MammoSite balloon deformation were explored as they could affect the dose within the treated volume or expose normal tissues to extra unnecessary dose. The Lyman-Kutcher and relative seriality models were used to estimate the normal tissues complications associated with the MammoSite dose distributions. The tumour control probability was calculated using the Poisson model. The study identified low probabilities for developing heart and lung complications. The probability of complications of the skin and normal breast tissues depended on the location of the source inside the balloon and the volume receiving high dose.

Incorrect source positioning caused significant reduction in the dose to regions of the planning target volume. A deviation of the source by 1 mm caused approximately 7% dose reduction in the treated target volume at 1 cm from the balloon surface whereas 2 mm source deviation caused about 14% dose reduction at the same point. A 4 mm source deviation produced underdosing of some portions of the PTV by 40% leading to poor treatment outcomes. A 4 mm balloon deformation resulted in the reduction of the tumour control probability by 24%. Furthermore, 4 mm uncertainties in source position lead to overdosing of regions outside the PTV by about 40%. This resulted in an excessive dose to the skin (not in the PTV) and increased the probability of skin complications. This study demonstrated the importance of keeping the spherical shape of the balloon and accurate positioning of the brachytherapy source at the balloon centre.

Unlike the Plato brachytherapy treatment planning system, our Monte Carlo model took into account variations in the dose caused by inhomogeneities. The presence of contrast medium in the MammoSite balloon represented an inhomogeneity to be investigated. The Monte Carlo simulations were performed for a clinical balloon of 4 cm diameter and various contrast concentrations. It was found that 100%, 50% and 15% contrast concentrations reduced the dose by 10%, 5% and 2% at the prescription point (1 cm from the surface of the balloon) respectively.

The Monte Carlo results were compared with measurements taken using LiF TLD-100 chips. The TLDs were first calibrated and the sensitivity normalization factor for each TLD-100 chip was measured. The linearity range for the TLDs was also measured and found to be within 6 Gy. The TLDs were irradiated inside a designed tissue equivalent breast phantom at various distances from the balloon surface using the HDR afterloading unit. The measurements were performed for a balloon filled with saline only, a balloon filled with contrast only and balloons filled with saline and 50% and 15% contrast concentrations. The measured and Monte Carlo computed relative doses were in excellent agreement all within the measurement uncertainty and Monte Carlo statistical errors. This investigation suggested that the amount of radiographic contrast used during MammoSite breast brachytherapy should be minimized (15%) to avoid potential significant reduction in the delivered dose.

The American Association of Physicists in Medicine (AAPM) Task Group 40 recommendation for intracavitary brachytherapy allows for ± 15% in the delivery of the prescribed dose contributing from all possible sources of uncertainties. Based on the current investigation, the combined uncertainties associated with the MammoSite brachytherapy technique, to the value of a 2 mm balloon deformation, a maximum source deviation of $\leq$ 1 mm and 15% contrast concentration, had little impact on the tumour control probability. As a result treatment protocols should be used that accept only 2 mm balloon deformation and contrast concentration values below 15%.

The EBRT treatment for early stage breast cancer is commonly delivered using 6 MV photon beams, applying asymmetric fields, physical wedges and multi-leaf collimators (MLCs). An accurate Monte Carlo model of the linac was generated. This was done by modelling the treatment head of a Varian 600 C/D with 6 MV x-ray beam energy. The models included open field, half-blocked (asymmetric) field, physical wedges of different angles and MLC fields. Dose distribution curves obtained from the linac model were compared with profiles measured in water for validation. The results showed that the dose differences between measurements and Monte Carlo simulations were less than 1% for depth doses, and within 2% for dose profiles inside the 80% field size (the region of low dose gradient). Therefore, an accurate model of the Varian 600 C/D linac was established to be used for patient dose calculations.

The Pinnacle^3 treatment planning system was used to develop a reference external beam radiotherapy treatment plan using patient CT images. The treatment plan included blocked beams, the direction of the incident beams (medial and lateral fields), MLCs and 15^0 physical wedge. The treatment plan was modelled and the dose distribution was calculated for both the medial and lateral fields. The CT images acquired for the MammoSite treatment were used for the simulation of external beam radiotherapy treatment as well. This particular simplification allowed us to combine the dose distributions on a voxel-by-voxel basis, without the need to consider anatomical changes between the two modalities.

The Monte Carlo simulations of the two modalities produced three dimensional dose distribution data files which were used for data processing. Combining the dose distributions from the two modalities was not a straightforward task due to the differences in delivery mode, fraction size, dose rate and energy associated with each modality. To account for these factors, the concept of equivalent dose was applied to combine the final two dose distributions.

An in-house developed Matlab code was used to extract two dimensional dose distribution matrices for individual simulation runs. For EBRT simulation, the 2D dose distributions were extracted for the medial and lateral tangential fields at the isocentre plane. The two distributions were then added together to produce a final planar dose distribution matrix for EBRT. The combined dose matrix was normalized to the isocentre point dose.

For the MammoSite simulation, the two dimensional distribution matrix was extracted at the same plane as that of EBRT. The dose was then normalized to an isocentre point. The 2D dose distribution matrix, from the MammoSite treatment, was first converted to biological effective dose matrix by applying the relative effectiveness factor. The two dimensional based biological effective dose matrix and then converted into a 2D equivalent dose matrix.

The 2D based equivalent dose distribution matrices for EBRT and MB were finally summed up pixel by pixel. In order to create a 3D dose distribution, the same process needed to be applied to the whole 3D dose matrices from both modalities. Combined dose distributions resulting from both radiotherapy techniques was acquired.

8.2 Future work

It was shown in this work that the EGSnrc Monte Carlo code could be used to combine the dose distributions from MammoSite brachytherapy and external beam radiotherapy techniques. However, there are issues that were not considered when combining the dose distributions from the two modalities. They included the time gap between the EBRT and MB treatments. Also, organ deformation, due to different anatomical position of tissue with (MammoSite) and without (EBRT) the balloon were not taken into account when combining the two modalities. To take such changes into account, deformable image registration (DIR) technique could be used for fusion of the data from the two modalities in future studies.

Appendix A. Source model input and list file

A.1 DOSXYZnrc input file

This input file was created in this work to model the HDR microSelectron ^{192}Ir brachytherapy source in Cartesian coordinate system.

```
Source dimensions model 3
2
H2O700ICRU
AIR700ICRU
0.521, 0.06, 0, 0, 0
-1, -1, -1, 1
-12.6
0.15, 168
-12.6
0.15, 168
-9.0
0.15, 120
1, 168, 1, 168, 1, 120, 1, 1.00
0, 0, 0, 0, 0, 0, 0, 0
0, 0, 0, 0, 0, 0, 0, 0
84, 84, 84, 84, 60, 60, 1, 0
0, 0, 0, 0, 0, 0, 0, 0
0, 6, -0.030, 0.030, -0.030, 0.030, -0.18, 0.18
1, 0, 2, 0, 0, 0, 0, 0
/home/bsaleh/henhouse/spectra/Ir192_microSelectron.spectrum
1000000000, 0, 500, 94, 35, 0, 0, 0, 1, 0, 0, -1, 0, 0, 30
 #########################
 :Start MC Transport Parameter:

 Global ECUT= 0.521
 Global PCUT= 0.06
 Global SMAX= 1e10
 ESTEPE= 0.25
 XIMAX= 0.5
 Boundary crossing algorithm= PRESTA-I
 Skin depth for BCA= 0
 Electron-step algorithm= PRESTA-II
 Spin effects= On
 Brems angular sampling= Simple
 Brems cross sections= BH
 Bound Compton scattering= On
 Pair angular sampling= Simple
 Photoelectron angular sampling= On
 Rayleigh scattering= Off
 Atomic relaxations= Off

 :Stop MC Transport Parameter:
 #########################
```

A.2 DOSXYZnrc List file

This file is an output of the source model 3. It shows parameters such as the position of the modelled source inside the water phantom and the number of energy bins read from the spectrum. It took approximately 32 hours to simulate 10^9 particles and obtain a statistical uncertainty of 0.1% near the vicinity of the source. These values are shown below at the bottom of the list file.

```
 Title:  source dimension model 3
Number of media (min = 1, max =  10, 0 => CT data): 2
Medium  1:                      H2O700ICRU
Medium  2:                      AIR700ICRU

ECUTIN,PCUTIN,(ESTEPE,SMAX--DUMMY INPUTS):0.521 0.060 0.000 0.000  0.000
# regions in x (max= 512),y (max= 512),z (max= 150) directions
(if<0,implies # groups of reg), IPHANT (1 to output a .egsphant file for
dosxyz_show, 0[default] to not output this file): -1 -1 -1 1

 Input boundaries in the x-direction
 ---------------------------------------
 Initial boundary:       -12.600
Width in this group, number of regions in group: 0.150  168
Boundaries
-12.600     -12.450     -12.300     -12.150     -12.000   11.850
-11.700     -11.550     -11.400     -11.250     -11.100   10.950
-10.800     -10.650     -10.500     -10.350     -10.200   10.050
-9.900      -9.750      -9.600      -9.450      -9.300    9.150
-9.000      -8.850      -8.700      -8.550      -8.400    8.250
-8.100      -7.950      -7.800      -7.650      -7.500    7.350
-7.200      -7.050      -6.900      -6.750      -6.600    6.450
-6.300      -6.150      -6.000      -5.850      -5.700    5.550
-5.400      -5.250      -5.100      -4.950      -4.800    4.650
-4.500      -4.350      -4.200      -4.050      -3.900    3.750
-3.600      -3.450      -3.300      -3.150      -3.000    2.850
-2.700      -2.550      -2.400      -2.250      -2.100    1.950
-1.800      -1.650      -1.500      -1.350      -1.200    1.050
-0.900      -0.750      -0.600      -0.450      -0.300    0.150
 0.000       0.150       0.300       0.450       0.600    0.750
 0.900       1.050       1.200       1.350       1.500    1.650
 1.800       1.950       2.100       2.250       2.400    2.550
 2.700       2.850       3.000       3.150       3.300    3.450
 3.600       3.750       3.900       4.050       4.200    4.350
 4.500       4.650       4.800       4.950       5.100    5.250
 5.400       5.550       5.700       5.850       6.000    6.150
 6.300       6.450       6.600       6.750       6.900    7.050
 7.200       7.350       7.500       7.650       7.800    7.950
 8.100       8.250       8.400       8.550       8.700    8.850
 9.000       9.150       9.300       9.450       9.600    9.750
 9.900      10.050      10.200      10.350      10.500   10.650
 10.800      10.950      11.100      11.250      11.400   11.550
 11.700      11.850      12.000      12.150      12.300   12.450
 12.600

 Input boundaries in the y-direction
 ---------------------------------------
 Initial boundary:       -12.600
Width in this group, number of regions in group: 0.150  168
Boundaries
-12.600     -12.450     -12.300     -12.150     -12.000   11.850
-11.700     -11.550     -11.400     -11.250     -11.100   10.950
-10.800     -10.650     -10.500     -10.350     -10.200   10.050
-9.900      -9.750      -9.600      -9.450      -9.300    9.150
-9.000      -8.850      -8.700      -8.550      -8.400    8.250
-8.100      -7.950      -7.800      -7.650      -7.500    7.350
-7.200      -7.050      -6.900      -6.750      -6.600    6.450
-6.300      -6.150      -6.000      -5.850      -5.700    5.550
-5.400      -5.250      -5.100      -4.950      -4.800    4.650
-4.500      -4.350      -4.200      -4.050      -3.900    3.750
-3.600      -3.450      -3.300      -3.150      -3.000    2.850
-2.700      -2.550      -2.400      -2.250      -2.100    1.950
-1.800      -1.650      -1.500      -1.350      -1.200    1.050
-0.900      -0.750      -0.600      -0.450      -0.300    0.150
 0.000       0.150       0.300       0.450       0.600    0.750
```

```
 0.900       1.050       1.200       1.350       1.500    1.650
 1.800       1.950       2.100       2.250       2.400    2.550
 2.700       2.850       3.000       3.150       3.300    3.450
 3.600       3.750       3.900       4.050       4.200    4.350
 4.500       4.650       4.800       4.950       5.100    5.250
 5.400       5.550       5.700       5.850       6.000    6.150
 6.300       6.450       6.600       6.750       6.900    7.050
 7.200       7.350       7.500       7.650       7.800    7.950
 8.100       8.250       8.400       8.550       8.700    8.850
 9.000       9.150       9.300       9.450       9.600    9.750
 9.900      10.050      10.200      10.350      10.500    10.650
 10.800      10.950      11.100      11.250      11.400   11.550
 11.700      11.850      12.000      12.150      12.300   12.450
 12.600

Input boundaries in the z-direction
-----------------------------------
Initial boundary:        -9.000
Width in this group, number of regions in group: 0.150  120
Boundaries
-9.000      -8.850      -8.700      -8.550      -8.400    8.250
-8.100      -7.950      -7.800      -7.650      -7.500    7.350
-7.200      -7.050      -6.900      -6.750      -6.600    6.450
-6.300      -6.150      -6.000      -5.850      -5.700    5.550
-5.400      -5.250      -5.100      -4.950      -4.800    4.650
-4.500      -4.350      -4.200      -4.050      -3.900    3.750
-3.600      -3.450      -3.300      -3.150      -3.000    2.850
-2.700      -2.550      -2.400      -2.250      -2.100    1.950
-1.800      -1.650      -1.500      -1.350      -1.200    1.050
-0.900      -0.750      -0.600      -0.450      -0.300    0.150
 0.000       0.150       0.300       0.450       0.600    0.750
 0.900       1.050       1.200       1.350       1.500    1.650
 1.800       1.950       2.100       2.250       2.400    2.550
 2.700       2.850       3.000       3.150       3.300    3.450
 3.600       3.750       3.900       4.050       4.200    4.350
 4.500       4.650       4.800       4.950       5.100    5.250
 5.400       5.550       5.700       5.850       6.000    6.150
 6.300       6.450       6.600       6.750       6.900    7.050
 7.200       7.350       7.500       7.650       7.800    7.950
 8.100       8.250       8.400       8.550       8.700    8.850
 9.000

Total # regions including exterior =   3386881
Input groups of regions for which density and medium are not defaults
Lower,upper i, j, k,  MEDIUM, DENSITY (  1 168)(  1 168)(  1 120) 1  1.000
Lower,upper i, j, k,  MEDIUM, DENSITY
Found blank line => end of this input

Input groups of regions for which ECUT and PCUT are not defaults
NB This option is disabled, just input 8 zeros.
Dummy values of lower,upper i, j, k,  ECUT, PCUT
Found blank line => end of this input

Enter 8 numbers on one line
3 pairs defininglower,upper x,y,z indicies of dose regions for which
results are to be output
IZSCAN:       non-zero for z-scan/page
MAX20:        if any one = 1, output summary of max 20 doses.
end signaled by first pair both zero for no dose printed, MAX20 is still
read from first line

84  84    84  84    60  60     1     0
Found blank line => end of this input

Read input energy spectrum from:
/home/bsaleh/henhouse/spectra/Ir192_microSelectron.spectrum
Have read   34 input energy bins from file Counts/MeV assumed
Energy ranges from     0.060 MeV to       0.885 MeV
```

```
Index ranges of source volume
-----------------------------
-0.030     0.030   i index ranges over i= 84 to  85
-0.030     0.030   j index ranges over j= 84 to  85
-0.180     0.180   k index ranges over k= 59 to  62

NCASE,IWATCH,TIMMAX,INSEED1,INSEED2,BEAM_SIZE,ISMOOTH,IRESTART,IDAT,
IREJECT,ESAVE_GLOBAL,NRCYCL,IPARALLEL,PARNUM,n_split:
1000000000 0 500.00 94 35 100.00 0 0 1 0 0.00 0 0 0 0 0

*****************************************************************
        Summary of source parameters (srcxyznrc Rev 1.6)
*********************************************************************
Uniform isotropically radiating parallelepiped within DOSXYZ volume
Electric charge of the source:            0
x-boundaries:       -0.0300 cm-    0.0300 cm
y-boundaries:       -0.0300 cm-    0.0300 cm
z-boundaries:       -0.1800 cm-    0.1800 cm
======================================================================
                   Electron/Photon transport parameter
======================================================================

Photon transport cutoff(MeV)                                 0.60E-01
Pair angular sampling                                        SIM
Pair cross sections                                          BH
Triplet production                                           Off
Bound Compton scattering                                     ON
Radiative Compton corrections                                Off
Rayleigh scattering                                          ON
Atomic relaxations                                           ON
Photoelectron angular sampling                               ON
Electron transport cutoff(MeV)                               0.70
Bremsstrahlung cross sections                                BH
Bremsstrahlung angular sampling                              SIM
Spin effects                                                 On
Electron Impact Ionization                                   0
Maxium electron step in cm (SMAX)                            5.0
Maximum fractional energy loss/step (ESTEPE)                 0.2500
Maximum 1st elastic moment/step (XIMAX)                      0.5000
Boundary crossing algorithm                                  PRESTA-I
Skin-depth for boundary crossing (MFP)                       324.3
Electron-step algorithm                                      PRESTAII
======================================================================
 Medium               AE        AP
H2O700ICRU          0.700     0.010
AIR700ICRU          0.700     0.010

No range rejection.
***************************************************************
Histories to be simulated for this run 1000000000
Histories to be analyzed after this run1000000000
***************************************************************
Elapsed wall clock time to this point=       3.654 s
CPU time so far for this run =       3.488 s
BATCH#  TIME-ELAPSED  TOTAL CPUTIME  RATIO  TIME OF DAY  RN pointers
    1      0.0            0.0      0.00    18:02:26   ixx jxx =   97  33
    2      11463.1        11463.2  1.00    21:13:29   ixx jxx =   26  59
Wall clock has gone past 24:00 hrs.
Elapsed time adjusted assuming batches took < 1 day to complete.
    3      22923.1        22923.3  1.00    00:24:29   ixx jxx =   41  74
    4      34382.2        34382.5  1.00    03:35:28   ixx jxx =   11  44
    5      45845.2        45845.1  1.00    06:46:31   ixx jxx =   57  90
    6      57305.1        57305.1  1.00    09:57:31   ixx jxx =   97  33
    7      68764.9        68764.8  1.00    13:08:31   ixx jxx =   42  75
    8      80232.5        80232.1  1.00    16:19:38   ixx jxx =   50  83
    9      91694.6        91694.3  1.00    19:30:40   ixx jxx =   25  58
   10      103155.7       103155.5 1.00    22:41:42   ixx jxx =   41  74
```

```
 Total CPU time for run =114614.6 s =  31.837 hr =>   31409612. hist/hr
 On i686-pc-linux-gnu (i686-pc-linux-gnu-f77)

 Fraction of incident energy deposited in the phantom  =      0.4117
 Number of charged particle steps simulated,   N_step  =      256276526
 Number of charged particle steps/incident fluence     =      2.56277E-01
 No. of PRESTA-II steps/total no. of charged particle steps = 0.40893

 Total number of incident particles =  1.00E+09
 DOSXYZnrc ($Revision: 1.24 $) Dose outputs (Dose/incident particle, Gy)

 for x=    -0.150 to     0.000     i= 84

ybounds: -0.150       0.000 j=       84
zbounds (-0.150) 0.000  60  1.015E-11- 0.1%

Total CPU time for this run =114636.1 s =  31.843 hr
END OF RUN          Aug  5 2008 01:52:59
```

Appendix B. Matlab code

This an in-house Matlab code has been developed to extract 2D dose matrix from Monte Carlo 3D dose distribution.

```
clear all
%filename1  =input ('please .....','s');
filename1 = '.3ddose';
fid  = fopen (filename1);
x_voxel= ;
% defines the number of voxels in x dirction
x_e = 1+x_voxel;
y_voxel= ;
% defines the number of voxels in y dirction
y_e = 1+y_voxel;
z_voxel= ;
% defines the number of voxels in z dirction
z_l =;
% defines the sensitive layer of the extraction
z_l=z_l-1;
z_e = 1+z_voxel;
element_read = x_voxel*y_voxel*z_l +3 + x_e + y_e + z_e;
read1 = fscanf (fid, '%g %g %g', [element_read 1]);
%clear read1;
mc = fscanf (fid, '%g %g %g', [x_voxel y_voxel]);
mc_max = max(max(mc));
%gives the maximum value
%mc = mc / mc_max * 100;
% normalization to maximum
mc = mc';
% change of matrix to transpose
%mc = mc *10e
% dose conversion
filename2   = input ('input please ...   ', 's');
% writes into Excel file
xlswrite(filename2,mc);
% saves into Excel file
```

Appendix C. determinations of sensitivity correction factors

The sensitivity correction factor was calculated for each TLD chip using the equations explained in Section 5.2.2.4. Table C1 shows the details of the calculations.

Table C1. Calculations of sensitivity correction factor for each TLD-100 chip.

TLD #	1^{st} reading (nC)	2^{nd} reading (nC)	3^{rd} reading (nC)	1^{st} normalized readout (nC)	2^{nd} normalized readout (nC)	3^{rd} normalized readout (nC)	Mean of normalized readouts (nC)	Sensitivity Correction Factor (SCF)
1	4023	3904	3800	3960.42	3878.76	3886.71	3908.63	1.014
2	4266	4124	4045	4199.64	4097.34	4137.30	4144.76	0.956
3	4108	3821	3716	4044.09	3796.30	3800.79	3880.40	1.021
4	3771	3733	3700	3712.34	3708.87	3784.43	3735.21	1.061
5	4043	3934	3810	3980.11	3908.570	3896.94	3928.54	1.009
6	4094	4080	3964	4030.31	4053.62	4054.45	4046.13	0.979
7	4021	3983	3902	3958.45	3957.25	3991.04	3968.91	0.999
8	4019	3920	3822	3956.48	3894.66	3909.21	3920.12	1.011
9	4088	4107	4062	4024.40	4080.45	4154.69	4086.51	0.970
10	4030	4086	3979	3967.31	4059.59	4069.79	4032.23	0.983
11	4049	3893	3843	3986.01	3867.83	3930.69	3928.18	1.009
12	4138	4040	3940	4073.63	4013.88	4029.90	4039.14	0.981
13	4064	4036	3912	4000.78	4009.91	4001.27	4003.98	0.990
14	4111	4036	3903	4047.05	4009.91	3992.06	4016.34	0.987
15	4124	4085	4004	4059.84	4058.59	4095.36	4071.27	0.973
16	3916	3958	3854	3855.08	3932.41	3941.94	3909.81	1.014
17	3931	3964	3849	3869.85	3938.37	3936.83	3915.02	1.012
18	4129	4163	4131	4064.77	4136.09	4225.26	4142.04	0.957
19	3992	4066	3970	3929.90	4039.72	4060.59	4010.07	0.988
20	4067	3963	3846	4003.73	3937.38	3933.76	3958.29	1.001
21	4128	3994	3860	4063.78	3968.18	3948.08	3993.35	0.992
22	4051	3985	3919	3987.98	3959.24	4008.43	3985.21	0.994
23	4026	3968	3846	3963.37	3942.35	3933.76	3946.49	1.004
24	4005	3994	3868	3942.70	3968.18	3956.26	3955.71	1.002
25	3838	3848	3716	3778.29	3823.12	3800.79	3800.74	1.043

Table C1 Continuous

TLD #	1st reading (nC)	2nd reading (nC)	3rd reading (nC)	1st normalized readout (nC)	2nd normalized readout (nC)	3rd normalized readout (nC)	Mean of normalized readouts (nC)	Sensitivity Correction Factor (SCF)
26	4068	4057	3952	4004.72	4030.77	4042.18	4025.89	0.984
27	3832	3779	3653	3772.39	3754.57	3736.36	3754.44	1.056
28	3916	3942	3827	3855.08	3916.52	3914.33	3895.31	1.017
29	3909	3978	3819	3848.19	3952.28	3906.14	3902.21	1.016
30	4143	4093	3971	4078.55	4066.54	4061.61	4068.90	0.974
31	3938	3933	3780	3876.74	3907.58	3866.25	3883.52	1.020
32	4191	3900	3718	4125.80	3874.79	3802.84	3934.48	1.007
33	3949	3864	3772	3887.57	3839.02	3858.07	3861.55	1.026
34	3968	3968	3859	3906.27	3942.35	3947.06	3931.89	1.008
35	4290	4102	3956	4223.26	4075.48	4046.27	4115.04	0.963
36	3936	3968	3818	3874.77	3942.35	3905.12	3907.41	1.014
37	4042	4127	3985	3979.12	4100.32	4075.93	4051.79	0.978
38	3898	3958	3818	3837.36	3932.41	3905.12	3891.63	1.018
39	3868	3996	3851	3807.83	3970.17	3938.87	3905.62	1.015
40	4078	4134	3973	4014.56	4107.28	4063.66	4061.83	0.976
41	4193	4051	3918	4127.77	4024.81	4007.40	4053.33	0.978
42	4102	4105	3969	4038.19	4078.46	4059.57	4058.74	0.976
43	4173	4025	3869	4108.08	3998.98	3957.28	4021.45	0.985
44	3840	3860	3750	3780.26	3835.05	3835.57	3816.96	1.038
45	4067	4035	3948	4003.73	4008.92	4038.09	4016.91	0.987
46	4104	4106	3910	4040.16	4079.46	3999.22	4039.61	0.981
47	3963	3907	3770	3901.35	3881.74	3856.03	3879.71	1.021
48	3955	4022	3989	3893.47	3995.99	4080.02	3989.83	0.993
49	3942	3870	3747	3880.68	3844.98	3832.50	3852.72	1.029
50	3889	3979	3851	3828.50	3953.28	3938.87	3906.88	1.014
Average	**4025.720**	**3988.880**	**3874.680**					

Mean of average readouts (nC) = (4025.72 + 3988.88 + 3874.68) / 3 = 3963.09

Appendix D. Monte Carlo modelling of the medial field

D.1 BEAMnrc model

This input file was generated to model the treatment head of the linac using information of a patient plan treated for breast cancer. The model includes the positions of the MLCs and a 15^0 physical wedge positioned up right for this field.

```
6mvbeam: creation of a patient model treated for breast cancer
AIR700ICRU
0, 0, 0, 0, 1, 2, 0,  IWATCH ETC.
90000000, 4, 148, 500.0, 2, 1000, 2, 0,  NCASE ETC.
20, 100, 0, 2, 14, 1,  DIRECTIONAL BREM OPTIONS
-1, 19, -0.13, 0.0, 0.0, 1.0,  0.0, 0.0, 0.0, 0.0,  IQIN, ISOURCE +
OPTIONS
0, MONOENERGETIC
5.7
0, 0, 0.7, 0.01, 0, 1, 2,  0 , ECUT,PCUT,IREJCT,ESAVE
0, 0, 0, 0, 0,  PHOTON FORCING
1, 8,  SCORING INPUT
0,1
0,  DOSE COMPONENTS
0.0, Z TO FRONT FACE
*********** start of CM SLABS with identifier TARGET
3.809, RMAX
X-RAY TARGET MADE OF TUNGSTEN AND COPPER
3, NSLABS
0.0, ZMIN
0.063, 0, 0, 0, 1, 0
W700ICRU
0.265, 0, 0, 0, 1, 0
CU700ICRU
1.772, 0, 0, 0, 1, 0
VACUUM
*********** start of CM FLATFILT with identifier FLATFILT
12.31, RMAX
primary collimator and flattening filter made of tungsten and lead
2.1, ZMIN
13, NUMBER OF LAYERS
1, 7.849, # CONES, ZTHICK OF LAYER 1
0.524,
2.481,
2, 0.036, # CONES, ZTHICK OF LAYER 2
0, 2.481,
0.126, 2.49,
2, 0.065, # CONES, ZTHICK OF LAYER 3
0.126, 2.49,
0.252, 2.506,
2, 0.164, # CONES, ZTHICK OF LAYER 4
0.252, 2.506,
0.504, 2.547,
2, 0.166, # CONES, ZTHICK OF LAYER 5
0.504, 2.547,
0.756, 2.588,
2, 0.154, # CONES, ZTHICK OF LAYER 6
0.756, 2.588,
1.08, 2.626,
2, 0.151, # CONES, ZTHICK OF LAYER 7
1.08, 2.626,
```

```
1.26, 2.664,
2, 0.141, # CONES, ZTHICK OF LAYER 8
1.26, 2.664,
1.512, 2.699,
2, 0.119, # CONES, ZTHICK OF LAYER 9
1.512, 2.699,
1.764, 2.729,
2, 0.103, # CONES, ZTHICK OF LAYER 10
1.764, 2.729,
2.016, 2.755,
2, 0.118, # CONES, ZTHICK OF LAYER 11
2.016, 2.755,
2.268, 2.784,
2, 0.021, # CONES, ZTHICK OF LAYER 12
2.268, 2.784,
2.419, 2.789,
2, 0.113, # CONES, ZTHICK OF LAYER 13
2.419, 2.789,
2.816, 2.817,
0.7, 0.01, 0, 3,
AIR700ICRU
0.7, 0.01, 0, 3,
W700ICRU
0.7, 0.01, 0, 4,
PB700ICRU
0.7, 0.01, 0, 3,
AIR700ICRU
0.7, 0.01, 0, 3,
W700ICRU
0.7, 0.01, 0, 4,
PB700ICRU
0.7, 0.01, 0, 3,
AIR700ICRU
0.7, 0.01, 0, 3,
W700ICRU
0.7, 0.01, 0, 4,
PB700ICRU
0.7, 0.01, 0, 3,
AIR700ICRU
0.7, 0.01, 0, 3,
W700ICRU
0.7, 0.01, 0, 4,
PB700ICRU
0.7, 0.01, 0, 3,
AIR700ICRU
0.7, 0.01, 0, 3,
W700ICRU
0.7, 0.01, 0, 4,
PB700ICRU
0.7, 0.01, 0, 3,
AIR700ICRU
0.7, 0.01, 0, 3,
W700ICRU
0.7, 0.01, 0, 4,
PB700ICRU
0.7, 0.01, 0, 3,
AIR700ICRU
0.7, 0.01, 0, 3,
W700ICRU
0.7, 0.01, 0, 4,
PB700ICRU
0.7, 0.01, 0, 3,
AIR700ICRU
0.7, 0.01, 0, 3,
```

```
W700ICRU
0.7, 0.01, 0, 4,
PB700ICRU
0.7, 0.01, 0, 3,
AIR700ICRU
0.7, 0.01, 0, 3,
W700ICRU
0.7, 0.01, 0, 4,
PB700ICRU
0.7, 0.01, 0, 3,
AIR700ICRU
0.7, 0.01, 0, 3,
W700ICRU
0.7, 0.01, 0, 4,
PB700ICRU
0.7, 0.01, 0, 3,
AIR700ICRU
0.7, 0.01, 0, 3,
W700ICRU
0.7, 0.01, 0, 4,
PB700ICRU
0.7, 0.01, 0, 3,
AIR700ICRU
0.7, 0.01, 0, 3,
W700ICRU
0.7, 0.01, 0, 4,
PB700ICRU
0.7, 0.01, 0, 3,
AIR700ICRU
0.7, 0.01, 0, 3,
W700ICRU
*********** start of CM CHAMBER with identifier ICHAMBER
6.0, RMAX
Use CHAMBER CM to model the ion chamber
11.31, ZMIN
0, 17, 0, N_TOP, N_CHM, N_BOT
5.9, 5.95, 5.98, RADII FOR CENTRAL PART
0.043, 0, ZTHICK, FLAG FOR LAYER 1 IN CENTRAL PART
0.7, 0.01, 0, 5,
STEEL700ICRU
0.314, 0, ZTHICK, FLAG FOR LAYER 2 IN CENTRAL PART
0.7, 0.01, 0, 5,
AIR700ICRU
0.027, 0, ZTHICK, FLAG FOR LAYER 3 IN CENTRAL PART
0.7, 0.01, 0, 5,
MICA700
0.314, 0, ZTHICK, FLAG FOR LAYER 4 IN CENTRAL PART
0.7, 0.01, 0, 5,
AIR700ICRU
0.027, 0, ZTHICK, FLAG FOR LAYER 5 IN CENTRAL PART
0.7, 0.01, 0, 5,
MICA700
0.314, 0, ZTHICK, FLAG FOR LAYER 6 IN CENTRAL PART
0.7, 0.01, 0, 5,
AIR700ICRU
0.027, 0, ZTHICK, FLAG FOR LAYER 7 IN CENTRAL PART
0.7, 0.01, 0, 5,
MICA700
0.314, 0, ZTHICK, FLAG FOR LAYER 8 IN CENTRAL PART
0.7, 0.01, 0, 5,
AIR700ICRU
0.038, 0, ZTHICK, FLAG FOR LAYER 9 IN CENTRAL PART
0.7, 0.01, 0, 5,
STEEL700ICRU
```

```
0.314, 0, ZTHICK, FLAG FOR LAYER 10 IN CENTRAL PART
0.7, 0.01, 0, 5,
AIR700ICRU
0.027, 0, ZTHICK, FLAG FOR LAYER 11 IN CENTRAL PART
0.7, 0.01, 0, 5,
MICA700
0.314, 0, ZTHICK, FLAG FOR LAYER 12 IN CENTRAL PART
0.7, 0.01, 0, 5,
AIR700ICRU
0.027, 0, ZTHICK, FLAG FOR LAYER 13 IN CENTRAL PART
0.7, 0.01, 0, 5,
MICA700
0.314, 0, ZTHICK, FLAG FOR LAYER 14 IN CENTRAL PART
0.7, 0.01, 0, 5,
AIR700ICRU
0.027, 0, ZTHICK, FLAG FOR LAYER 15 IN CENTRAL PART
0.7, 0.01, 0, 5,
MICA700
0.314, 0, ZTHICK, FLAG FOR LAYER 16 IN CENTRAL PART
0.7, 0.01, 0, 5,
AIR700ICRU
0.043, 0, ZTHICK, FLAG FOR LAYER 17 IN CENTRAL PART
0.7, 0.01, 0, 5,
STEEL700ICRU
0.7, 0.01, 0, 5,   chamber wall
STEEL700ICRU
0.7, 0.01, 0, 5,   gap
AIR700ICRU
0.7, 0.01, 0, 5,   container
AIR700ICRU
0, MRNGE
*********** start of CM MIRROR with identifier MIRROR
6.78, RMAX
mirror made of MYLAR at 35 degree about the x-axis
16.85, 9.02, ZMIN, ZTHICK
6.78, -6.1, XFMIN, XBMIN
1, # LAYERS
0.005,  thickness of layer 1
0.7, 0.01, 0, 6,
MYLAR700ICRU
0.7, 0.01, 0, 6,
AIR700ICRU
0.7, 0.01, 0, 6,
AIR700ICRU
*********** start of CM JAWS with identifier SEC_COL
28, RMAX
secondary collimator modelled using the CM JAWS
2, # PAIRED BARS OR JAWS
X
28, 35.8, 2.8, 3.58, -2.24, -2.864,
Y
36.7, 44.5, 2.936, 3.56, -2.936, -3.56,
0.7, 0.01, 0, 0,
0.7, 0.01, 0, 7,
W700ICRU
0.7, 0.01, 0, 7,
W700ICRU
*********** start of CM VARMLC with identifier mlc
20, RMAX
MLC TS3
0, 1, ORIENT, NGROUP
47.8345, ZMIN
6.131, ZTHICK
40, 0.4757
```

```
-9.75, START
0.3129, 0.3023, WSCREW, HSCREW
0.0597, 2.5451, 49.6486, WTONGUE, HTONGUE, ZTONGUE
0.06477, 2.9769, 49.4327, WGROOVE, HGROOVE, ZGROOVE
0.005, LEAFGAP
0, ENDTYPE
8.001, ZFOCUS or RADIUS of leaf ends
0, ZFOCUS of leaf sides
0, 0, 10
-4.0618, 1.8477, 1
-4.0618, 1.868,  1
-4.0618, 1.9189, 1
-4.0618, 1.9749, 1
-4.0618, 1.9953, 1
-4.0618, 2.0462, 1
-4.0618, 2.0716, 1
-4.0618, 2.1225, 1
-4.0618, 2.4533, 1
-4.0618, 2.9166, 1
-4.0618, 3.2169, 1
-4.0618, 3.4256, 1
-4.0618, 3.7768, 1
-4.0618, 4.0822, 1
-4.0618, 3.6801, 1
-4.0618, 3.1914, 1
-4.0618, 1.6644, 1
-4.0618, 1.0842, 1
0, 0, 12
0.7, 0.01, 0, 0,
AIR700ICRU
0.7, 0.01, 0, 0, 1,
W700ICRU
*********** start of CM SLABS with identifier POLY
50, RMAX
air filled region
1, NSLABS
57.29, ZMIN
0.3, 0.7, 0.01, 0, 0, 0
POLYSTY700ICRU
*********** start of CM PYRAMIDS with identifier WEDGE
12.67, RMAX
WEDGE
4, 1, #LAYERS, SPECIFY MATERIAL OUTSIDE
57.6, 57.87, 12.67, 12.67, -12.67, -12.67, 6.25, 6.25, -6.25, -6.25,
12.67, 12.67,
57.88, 57.93, 12.67, 12.67, -12.67, -12.67, 6.25, 5.69, -6.25, -6.25,
12.67, 12.67,
57.94, 58.12, 12.67, 12.67, -12.67, -12.67, 5.69, 3.59, -6.25, -6.25,
12.67, 12.67,
58.13, 58.82, 12.67, 12.67, -12.67, -12.67, 3.59, -6.24, -6.25, -6.25,
12.67, 12.67,
0.7, 0.01, 0, 0, ECUT ETC. FOR AIR
0.7, 0.01, 0, 0,
STEEL700ICRU
0.7, 0.01, 0, 0,
AIR700ICRU
0.7, 0.01, 0, 0,
STEEL700ICRU
0.7, 0.01, 0, 0,
AIR700ICRU
0.7, 0.01, 0, 0,
STEEL700ICRU
0.7, 0.01, 0, 0,
AIR700ICRU
```

```
0.7, 0.01, 0, 0,
STEEL700ICRU
0.7, 0.01, 0, 0,
AIR700ICRU
*********************end of all CMs
 #########################
 :Start MC Transport Parameter:

 Global ECUT= 0.7
 Global PCUT= 0.01
 Global SMAX= 1e10
 ESTEPE= 0.25
 XIMAX= 0.5
 Boundary crossing algorithm= PRESTA-I
 Skin depth for BCA= 0
 Electron-step algorithm= PRESTA-II
 Spin effects= On
 Brems angular sampling= Simple
 Brems cross sections= BH
 Bound Compton scattering= On
 Pair angular sampling= Simple
 Photoelectron angular sampling= Off
 Rayleigh scattering= Off
 Atomic relaxations= On
 Electron impact ionization= Off

 :Stop MC Transport Parameter:
 #########################
```

D.2 DOSXYZnrc model

This input files was generated to simulate the dose distribution using patient CT dataset. It includes many parameters such the angle of the tangential medial field, the phase space file, the number of simulated particle and the Monte Carlo transport parameters.

Input file using phase-space data from BEAMnrc model of the medial field

```
0
/home/bsaleh/henhouse/omega/progs/ctcreate/CT/Pinnacle/ImageSet_11.egspha
nt
0.7, 0.05, 0, 0, 0
1, 0, 1
2, 2, 8.2, -82.80, 3.0, 90.0, 235.0, 41.18, 0.0
2, 0, 0, 0
/home/bsaleh/egshome/BEAM_medial/medial.egsphsp1
800000000, 0, 900, 97, 33, 20, 0, 0, 0, 1, 3, 0, 0, 0, 1
 #########################
 :Start MC Transport Parameter:

 Global ECUT= 0.7
 Global PCUT= 0.05
 Global SMAX= 5
 ESTEPE= 0.25
 XIMAX= 0.5
 Boundary crossing algorithm= PRESTA-I
 Skin depth for BCA= 0
 Electron-step algorithm= PRESTA-II
 Spin effects= On
 Brems angular sampling= Simple
 Brems cross sections= BH
```

```
Bound Compton scattering= Off
Pair angular sampling= Simple
Photoelectron angular sampling= Off
Rayleigh scattering= Off
Atomic relaxations= Off

:Stop MC Transport Parameter:
#########################
```

Bibliography

[1]. World Health Organization. http://www.who.int/cancer/en/. 2006.

[2]. Borg M, Yeoh E, Bochner M, et al. Feasibility study on the MammoSite in early-stage breast cancer: initial experience. *Australas Radiol* 2007; 51: 53-61.

[3]. Borg M, Yeoh E. Guidelines for the radiotherapeutic management of breast cancer. 1997: The Royal Adelaide Hospital, Adelaide.

[4]. Blichert-Toft M, Brincker H, Andersen J, et al. A Danish randomized trial comparing breast-preserving therapy with mastectomy in mammary carcinoma. Preliminary results. *Acta Oncol* 1988; 27: 671-7.

[5]. Fisher B, Redmond C, Poisson R, et al. Eight-year results of a randomized clinical trial comparing total mastectomy and lumpectomy with or without irradiation in the treatment of breast cancer. *N Engl J Med* 1989; 320: 822-8.

[6]. Sarrazin D, Le M, Arriagada R, et al. Ten-year results of a randomized trial comparing a conservative treatment to mastectomy in early breast cancer. *Radiother Oncol* 1989; 14: 177-84.

[7]. Van Dongen J, Bartelink H, Fentiman I, et al. Randomized clinical trial to assess the value of breast-conserving therapy in stage I and II breast cancer, EORTC 10801 trial. *J Natl Cancer Inst Monogr* 1992; 11: 15-8.

[8]. Veronesi U, Banfi A, Del Vecchio M, et al. Comparison of Halsted mastectomy with quadrantectomy, axillary dissection, and radiotherapy in early breast cancer: long-term results. *Eur J Cancer Clin Oncol* 1986; 22: 1085-9.

[9]. Athas WF, Adams-Cameron M, Hunt WC, Amir-Fazli A, Key CR. Travel distance to radiation therapy and receipt of radiotherapy following breast-conserving surgery. *J Natl Cancer Inst* 2000; 92: 269-71.

[10]. Edmundson GK, Vicini FA, Chen PY, Mitchell C, Martinez AA. Dosimetric characteristics of the MammoSite RTS, a new breast brachytherapy applicator. *Int J Radiat Oncol Biol Phys* 2002; 52: 1132-9.

[11]. Kassas B, Mourtada F, Horton JL, Lane RG. Contrast effects on dosimetry of a partial breast irradiation system. *Med Phys* 2004; 31: 1976-9.

[12]. Kirk MC, Hsi WC, Chu JC, et al. Dose perturbation induced by radiographic contrast inside brachytherapy balloon applicators. *Med Phys* 2004; 31: 1219-24.

[13]. Vicini FA, Kestin LL, Goldstein NS. Defining the clinical target volume for patients with early-stage breast cancer treated with lumpectomy and accelerated partial breast irradiation: a pathologic analysis. *Int J Radiat Oncol Biol Phys* 2004; 60: 722-30.

[14]. Dickler A, Kirk M, Choo J, et al. Treatment volume and dose optimization of MammoSite breast brachytherapy applicator. *Int J Radiat Oncol Biol Phys* 2004; 59: 469-74.

[15]. Khan AJ, Kirk MC, Mehta PS, et al. A dosimetric comparison of three-dimensional conformal, intensity-modulated radiation therapy, and MammoSite partial-breast irradiation. *Brachytherapy* 2006; 5: 183-8.

[16]. Major T, Niehoff P, Kovacs G, Fodor J, Polgar C. Dosimetric comparisons between high dose rate interstitial and MammoSite balloon brachytherapy for breast cancer. *Radiother Oncol* 2006; 79: 321-8. Epub 2006 May 26.

[17]. Weed DW, Edmundson GK, Vicini FA, Chen PY, Martinez AA. Accelerated partial breast irradiation: a dosimetric comparison of three different techniques. *Brachytherapy* 2005; 4: 121-9.

[18]. Keisch M, Vicini F, Kuske RR, et al. Initial clinical experience with the MammoSite breast brachytherapy applicator in women with early-stage breast cancer treated with breast-conserving therapy. *Int J Radiat Oncol Biol Phys* 2003; 55: 289-93.

[19]. Dragun AE, Harper JL, Jenrette JM, Sinha D, Cole DJ. Predictors of cosmetic outcome following MammoSite breast brachytherapy: a single-institution experience of 100 patients with two years of follow-up. *Int J Radiat Oncol Biol Phys* 2007; 68: 354-8. Epub 2007 Mar 26.

[20]. Niehoff P, Polgar C, Ostertag H, et al. Clinical experience with the MammoSite radiation therapy system for brachytherapy of breast cancer: results from an international phase II trial. *Radiother Oncol* 2006; 79: 316-20. Epub 2006 Jun 14.

[21]. Jeruss JS, Vicini FA, Beitsch PD, et al. Initial outcomes for patients treated on the American Society of Breast Surgeons MammoSite clinical trial for ductal carcinoma-in-situ of the breast. *Ann Surg Oncol* 2006; 13: 967-76. Epub 2006 May 16.

[22]. Keisch ME, Vicini F, Kuske R, et al. Two-year outcome with the MammoSite breast brachytherapy applicator: Factors associated with optimal cosmetic outcome when performing partial breast irradiation. *Int J Radiat Oncol Biol Phys* 2003; 57: S311.

[23]. Keisch ME, Vicini F, Scroggins T, et al. Thirty months results with the MammoSite breast brachytherapy applicator:Cosmesis, toxicity and local control in partial breast irradiation. *Int J Radiat Oncol Biol Phys* 2004; 60: S272.

[24]. Shah NM, Tenenholz T, Arthur D, et al. MammoSite and interstitial brachytherapy for accelerated partial breast irradiation: factors that affect toxicity and cosmesis. *Cancer* 2004; 101: 727-34.

[25]. Dickler A, Kirk MC, Choo J, et al. Cosmetic outcome and incidence of infection with the MammoSite breast brachytherapy applicator. *Breast J* 2005; 11: 306-10.

[26]. DiFronzo LA, Tsai PI, Hwang JM, et al. Breast conserving surgery and accelerated partial breast irradiation using the MammoSite system: initial clinical experience. *Arch Surg* 2005; 140: 787-94.

[27]. Harper JL, Jenrette JM, Vanek KN, Aguero EG, Gillanders WE. Acute complications of MammoSite brachytherapy: a single institution's initial clinical experience. *Int J Radiat Oncol Biol Phys* 2005; 61: 169-74.

[28]. Vicini FA, Beitsch PD, Quiet CA, et al. First analysis of patient demographics, technical reproducibility, cosmesis, and early toxicity: results of the American Society of Breast Surgeons MammoSite breast brachytherapy trial. *Cancer* 2005; 104: 1138-48.

[29]. Benitez PR, Streeter O, Vicini F, et al. Preliminary results and evaluation of MammoSite balloon brachytherapy for partial breast irradiation for pure ductal carcinoma in situ: a phase II clinical study. *Am J Surg* 2006; 192: 427-33.

[30]. Sadeghi A, Prestidge B, Lee JM, Rosenthal A. Evaluation of the surface radiation dose and dose gradient in early stage breast cancer using high-dose-rate brachytherapy MammoSite applicator. *Brachytherapy* 2006; 5: 230-4.

[31]. Chao KK, Vicini FA, Wallace M, et al. Analysis of treatment efficacy, cosmesis, and toxicity using the MammoSite breast brachytherapy catheter to deliver accelerated partial-breast irradiation: the william beaumont hospital experience. *Int J Radiat Oncol Biol Phys* 2007; 69: 32-40. Epub 2007 Apr 30.

[32]. Chen S, Dickler A, Kirk M, et al. Patterns of failure after MammoSite brachytherapy partial breast irradiation: a detailed analysis. *Int J Radiat Oncol Biol Phys* 2007; 69: 25-31.

[33]. Benitez PR, Keisch ME, Vicini F, et al. Five-year results: the initial clinical trial of MammoSite balloon brachytherapy for partial breast irradiation in early-stage breast cancer. *Am J Surg* 2007; 194: 456-62.

[34]. Richards GM, Berson AM, Rescigno J, et al. Acute toxicity of high-dose-rate intracavitary brachytherapy with the MammoSite applicator in patients with early-stage breast cancer. *Ann Surg Oncol* 2004; 11: 739-46. Epub 2004 Jul 12.

[35]. Agawal A, Beriwa lS, Heron DE, et al. Accelerated partial breast irradiation: Single institutional experience of 100 patients using MammoSite brachytherapy. *Int J Radiat Oncol Biol Phys* 2005; 63 (Suupl 1): s6-s7.

[36]. Evans SB, Kaufman SA, Price LL, Cardarelli G, Dipetrillo TA, Wazer DE. Persistent seroma after intraoperative placement of MammoSite for accelerated partial breast irradiation: incidence, pathologic anatomy, and contributing factors. *Int J Radiat Oncol Biol Phys* 2006; 65: 333-9. Epub 2006 Mar 20.

[37]. Nath R, Anderson LL, Luxton G, Weaver KA, Williamson JF, Meigooni AS. Dosimetry of interstitial brachytherapy sources: recommendations of the AAPM Radiation Therapy Committee Task Group No. 43. American Association of Physicists in Medicine. *Med Phys* 1995; 22: 209-34.

[38]. Kawrakow I. Accurate condensed history Monte Carlo simulation of electron transport. I. EGSnrc, the new EGS4 version. *Med Phys* 2000; 27: 485-98.

[39]. Rogers D, Faddegon B, Ding G, Ma C, Wei J, Mackie T. BEAM: A Monte Carlo code to simulate radiotherapy treatment units. *Med Phys* 1995; 22: 503-24.

[40]. Kawrakow I, Rogers DWO. The EGSnrc code system: Monte Carlo simulation of electron and photon transport, Technical Report PIRS-701 National Research Council of Canada, 2000.

[41]. Nelson WR, Hirayama H, Rogers DWO. The EGS4 code system. Stanford Linear Accelerator Centre Report SLAC-265, Stanford, CA 1985.

[42]. Briesmeister JF. MCNP^{TM}-A General Monte Carlo N-Particle Transport code, Version 4C Technical Report No la-13709-M, Los Alamos National Laboratory. 2000.

[43]. Waters LS. MCNPX-Users Manual Version 2.4.0, Report LA-CP-02-408, Los Alamos National Laboratory,. 2002.

[44]. Salvat F, Fernández-Varea JM, Sempau J. Penelope-A code system for Monte Carlo simulation of electron and photon transport. Issy-les-Moulineaux, France, 2003.

[45]. Agostinelli S, Allison J, Amako K, et al. GEANT4-a Simulation Toolkit *J Nucl Instrum Meth* 2003; A506.

[46]. Bielajew AF. *Fundamentals of the Monte Carlo method for neutral and charged particle transport*. University of Michigan, 2001.

[47]. Rogers DWO, Bielajew AF. "Monte Carlo Techniques of Electron and Photon Transport for Radiation Dosimetry", The dosimetry of Ionizing Radiation. New York: Academic Press, 1990: 427-539.

[48]. Attix F. *Introduction to radiological physics and radiation dosimetry*. John Wiley and Son, USA, 1986.

[49]. Berger MJ. Monte Carlo calculation of the penetration and diffusion of fast charged particles. *Methods Comput Phys* 1963; 1: 135-215.

[50]. Cygler J, Battista JJ, Scrimger JW, Mah E, Antolak J. Electron dose distributions in experimental phantoms: a comparison with 2D pencil beam calculations. *Phys Med Biol* 1987; 32: 1073-86.

[51]. Mah E, Antolak J, Scrimger JW, Battista JJ. Experimental evaluation of a 2D and a 3D electron pencil beam algorithm. *Med Phys* 1989; 34: 1179-94.

[52]. Jette D, Walker S. Electron dose calculation using multiple-scattering theory: evaluation of a new model for inhomogeneities. *Med Phys* 1992; 19: 1241-54.

[53]. Shiu AS, Hogstrom KR. Pencil-beam redefinition algorithm for electron dose distributions. *Med Phys* 1991; 18: 7-18.

[54]. Shortt KR, Ross C, Bielajew AF, Rogers DWO. Electron beam dose distributions near standard inhomogeneities. *Phys Med Biol* 1986; 31: 235-48.

[55]. Rogers DWO, Walters B, Kawrakow I. BEAMnrc users manual, NRC Report PIRS-0509(A)revK. National Research Council of Canada, 2006.

[56]. Walters B, Kawrakow I, Rogers DWO. DOSXYZnrc users manual NRC Report PIRS-794 revB. National Research Council of Canada, 2005.

[57]. McGowan HCE, Faddegon BA, Ma C-M. STATDOSE for 3D dose distributions. NRC Report PIRS 509f, 1995.

[58]. Kawrakow I. The dose visualization tool dosxyz_show. NRCC Report PIRS-0624, 2006.

[59]. Williamson JF, Li Z. Monte Carlo aided dosimetry of the microselectron pulsed and high dose-rate ^{192}Ir sources. *Med Phys* 1995; 22: 809-19.

[60]. Valicenti RK, Kirov AS, Meigooni AS, Mishra V, Das RK, Williamson JF. Experimental validation of Monte Carlo dose calculations about a high-intensity Ir-192 source for pulsed dose-rate brachytherapy. *Med Phys* 1995; 22: 821-9.

[61]. Borg J, Rogers DW. Spectra and air-kerma strength for encapsulated ^{192}Ir sources. *Med Phys* 1999; 26: 2441-4.

[62]. Angelopoulos A, Baras P, Sakelliou L, Karaiskos P, Sandilos P. Monte Carlo dosimetry of a new ^{192}Ir high dose rate brachytherapy source. *Med Phys* 2000; 27: 2521-7.

[63]. Toye WC, Das KR, Todd SP, Kenny MB, Franich RD, Johnston PN. An experimental MOSFET approach to characterize ^{192}Ir HDR source anisotropy. *Phys Med Biol* 2007; 52: 5329-39.

[64]. Papagiannis P, Angelopoulos A, Pantelis E, et al. Dosimetry comparison of ^{192}Ir sources. *Med Phys* 2002; 29: 2239-46.

[65]. Granero D, Perez-Calatayud J, Ballester F. Monte Carlo study of the dose rate distributions for the Ir2.A85-2 and Ir2.A85-1 Ir-192 afterloading sources. *Med Phys* 2008; 35: 1280-7.

[66]. Baltas D, Karaiskos P, Papagiannis P, Sakelliou L, Loeffler E, Zamboglou N. Beta versus gamma dosimetry close to Ir-192 brachytherapy sources. *Med Phys* 2001; 28: 1875-82.

[67]. Mohan R, Chui C, Lidofsky L. Energy and angular distributions of photons from medical linear accelerators. *Med Phys* 1985; 12: 592-7.

[68]. Kim JL, Lee JI, Ji YH, Kim BH, Kim JS, Chang SY. Energy responses of the LiF series TL pellets to high-energy photons in the energy range from 1.25 to 21 MV. *Radiat Prot Dosimetry* 2006; 119: 353-6. Epub 2006 Apr 27.

[69]. Sichani BT, Sohrabpour M. Monte Carlo dose calculations for radiotherapy machines: Theratron 780-C teletherapy case study. *Phys Med Biol* 2004; 49: 807-18.

[70]. McKenzie AL. Cobalt-60 gamma-ray beams. *BJR Suppl* 1996; 25: 46-61.

[71]. Blazy L, Baltes D, Bordy JM, et al. Comparison of PENELOPE Monte Carlo dose calculations with Fricke dosimeter and ionization chamber measurements in heterogeneous phantoms (18 MeV electron and 12 MV photon beams). *Phys Med Biol* 2006; 51: 5951-65.

[72]. Schach von Wittenau AE, Bergstrom PM, Jr., Cox LJ. Patient-dependent beam-modifier physics in Monte Carlo photon dose calculations. *Med Phys* 2000; 27: 935-47.

[73]. Ma C-M, Reckwerdt P, Holmes M, Rogers DWO, Geiser B, Walters B. 1996 DOSXYZ user manual. Ottawa: NRCC Report PIRS-0509B, 1996.

[74]. Shih R, Li X, Chu J. Dynamic wedge versus physical wedge: a Monte Carlo study. *Med Phys* 2001; 28: 612-9.

[75]. Ma C-M, Rogers DWO, Walters BR. DOSXYZ99 users manual. Ottawa: National Research Council of Canada Report PIRS-0509B (revD), 1999.

[76]. van der Zee W, Welleweerd J. A Monte Carlo study on internal wedges using BEAM. *Med Phys* 2002; 29: 876-85.

[77]. Verhaegen F, Liu HH. Incorporating dynamic collimator motion in Monte Carlo simulations: an application in modelling a dynamic wedge. *Phys Med Biol* 2001; 46: 287-96.

[78]. Shih R, Lj X, Hsu W. Dosimetric characteristics of dynamic wedged fields: a Monte Carlo study. *Phys Med Biol* 2001; 46: N281-92.

[79]. De Vlamynck K, Palmans H, Verhaegen F, De Wagter C, De Neve W, Thierens H. Dose measurements compared with Monte Carlo simulations of narrow 6 MV multileaf collimator shaped photon beams. *Med Phys* 1999; 26: 1874-82.

[80]. Kim J, Siebers J, Keall P, Arnfield M, Mohan R. A Monte Carlo study of radiation transport through multileaf collimators. *Med Phys* 2001; 28: 2497-506.

[81]. kapur A, Ma C-M, Boyer A. Monte Carlo simulations for multileaf collimator leaves:design and dosimetry. *Proc Chicago 2000 World Congress on Medical Physics and Biomedical Engineering* 2000.

[82]. Heath E, Seuntjens J. Development and validation of a BEAMnrc component module for accurate Monte Carlo modelling of the Varian dynamic Millennium multileaf collimator. *Phys Med Biol* 2003; 48: 4045-63.

[83]. Lydon JM. Theoretical and experimental validation of treatment planning for narrow MLC defined photon fields. *Phys Med Biol* 2005; 50: 2701-14.

[84]. Cheng CW, Mitra R, Li XA, Das IJ. Dose perturbations due to contrast medium and air in mammosite treatment: an experimental and Monte Carlo study. *Med Phys* 2005; 32: 2279-87.

[85]. Ye SJ, Brezovich IA, Shen S, Kim S. Dose errors due to inhomogeneities in balloon catheter brachytherapy for breast cancer. *Int J Radiat Oncol Biol Phys* 2004; 60: 672-7.

[86]. Rogers DWO, Kawrakow I, seuntjens JP, Walters BR, Mainegra-Hing E. NRC user codes for EGSnrc. . NRCC Report PIRS-702(rev B), 2010.

[87]. Karaiskos P, Angelopoulos A, Sakelliou L, et al. Monte Carlo and TLD dosimetry of an 192Ir high dose-rate brachytherapy source. *Med Phys* 1998; 25: 1975-84.

[88]. Borg j, Rogers DWO. Monte Carlo calculation of photon spectra in air from Ir-192 sources. NRC Report PIRS-629r, 1999.

[89]. Nag S, Gupta N. A simple method of obtaining equivalent doses for use in HDR brachytherapy. *Int J Radiat Oncol Biol Phys* 2000; 46: 507-13.

[90]. Dale RG. The application of the linear-quadratic dose-effect equation to fractionated and protracted radiotherapy. *Br J Radiol* 1985; 58: 515-28.

[91]. Bentzen SM, Overgaard M. Relationship between early and late normal-tissue injury after postmastectomy radiotherapy. *Radiother Oncol* 1991; 20: 159-65.

[92]. Bentzen SM, Saunders MI, Dische S. Repair halftimes estimated from observations of treatment-related morbidity after CHART or conventional radiotherapy in head and neck cancer. *Radiother Oncol* 1999; 53: 219-26.

[93]. Hall EJ. *Radiobiology for the Radiologist*. Philadelphia, PA: Williams & Williams) pp352-356, 2000.

[94]. Turesson I, Thames HD. Repair capacity and kinetics of human skin during fractionated radiotherapy: erythema, desquamation, and telangiectasia after 3 and 5 year's follow-up. *Radiother Oncol* 1989; 15: 169-88.

[95]. Lyman JT. Complication probability as assessed from dose-volume histograms. *Radiat Res Suppl* 1985; 8: S13-9.

[96]. Kutcher GJ, Burman C. Calculation of complication probability factors for non-uniform normal tissue irradiation: the effective volume method. *Int J Radiat Oncol Biol Phys* 1989; 16: 1623-30.

[97]. Alexander MA, Brooks WA, Blake SW. Normal tissue complication probability modelling of tissue fibrosis following breast radiotherapy. *Phys Med Biol* 2007; 52: 1831-43. Epub 2007 Mar 7.

[98]. Burman C, Kutcher GJ, Emami B, Goitein M. Fitting of normal tissue tolerance data to an analytic function. *Int J Radiat Oncol Biol Phys* 1991; 21: 123-35.

[99]. Gagliardi G, Lax I, Ottolenghi A, Rutqvist L. Long-term cardiac mortality after radiotherapy of breast cancer--application of the relative seriality model. *Br J Radiol* 1996; 69: 839-46.

[100]. Kwa SL, Lebesque JV, Theuws JC, et al. Radiation pneumonitis as a function of mean lung dose: an analysis of pooled data of 540 patients. *Int J Radiat Oncol Biol Phys* 1998; 42: 1-9.

[101]. Steel G. *Basic Clinical Radiology*. London: Arnold p34, 2002.

[102]. Kallman P, Agren A, Brahme A. Tumour and normal tissue responses to fractionated non-uniform dose delivery. *Int J Radiat Biol* 1992; 62: 249-62.

[103]. Raphael C. Mathematical modelling of objectives in radiation therapy treatment planning. *Phys Med Biol* 1992; 37: 1293-311.

[104]. Webb S, Nahum AE. A model for calculating tumour control probability in radiotherapy including the effects of inhomogeneous distributions of dose and clonogenic cell density. *Phys Med Biol* 1993; 38: 653-66.

[105]. Wang JZ, Li XA. Evaluation of external beam radiotherapy and brachytherapy for localized prostate cancer using equivalent uniform dose. *Med Phys* 2003; 30: 34-40.

[106]. Brenner DJ, Hall EJ. Conditions for the equivalence of continuous to pulsed low dose rate brachytherapy. *Int J Radiat Oncol Biol Phys* 1991; 20: 181-90.

[107]. Dale RG. Radiobiological assessment of permanent implants using tumour repopulation factors in the linear-quadratic model. *Br J Radiol* 1989; 62: 241-4.

[108]. Thames H. An 'incomplete-repair' model for survival after fractionated and continuous irradiations. *Int J Radiat Biol Relat Stud Phys Chem Med* 1985; 47(3): 319-39.

[109]. Bovi J, Qi XS, White J, Li XA. Comparison of three accelerated partial breast irradiation techniques: treatment effectiveness based upon biological models. *Radiother Oncol* 2007; 84: 226-32. Epub 2007 Aug 10.

[110]. Fourquet A, Campana F, Mosseri V, et al. Iridium-192 versus cobalt-60 boost in 3-7 cm breast cancer treated by irradiation alone: final results of a randomized trial. *Radiother Oncol* 1995; 34: 114-20.

[111]. Guerrero M, Li XA. Analysis of a large number of clinical studies for breast cancer radiotherapy: estimation of radiobiological parameters for treatment planning. *Phys Med Biol* 2003; 48: 3307-26.

[112]. Haustermans K, Fowler J, Geboes K, Christiaens MR, Lerut A, van der Schueren E. Relationship between potential doubling time (Tpot), labeling index and duration of DNA synthesis in 60 esophageal and 35 breast tumors: Is it worthwhile to measure Tpot? *Radiother Oncol* 1998; 46: 157-67.

[113]. Mitra R, Cheng C, Das I. Dose perturbations due to contrast medium in MammoSite: dosimetric investigation of dose calculation accuracy [abstract]. *Med Phys* 2003; 30: 1388.

[114]. ICRU. International Commission and Radiation Units and Measurements. (ICRU, 44,, 1989.

[115]. Kawrakow, Hing-Mainegra E, Rogers DWO. EGSnrcMP: the multi-platform environment for EGSnrc. NRCC Report PIRS-877), 2004.

[116]. Horowitz YS. The theoretical and microdosimetric basis of thermoluminescence and applications to dosimetry. *Phys Med Biol* 1981; 26: 765-824.

[117]. Furetta C, Santopietro F, Sanipoli C, Kitis G. Thermoluminescent (TL) properties of the perovskite KMgF3 activated by Ce and Er impurities. *Appl Radiat Isot* 2001; 55: 533-42.

[118]. Fairbanks EJ, DeWerd LA. Thermoluminescent characteristics of LiF:Mg,Ti from three manufacturers. *Med Phys* 1993; 20: 729-31.

[119]. Yu C, Luxton G. TLD dose measurement: a simplified accurate technique for the dose range from 0.5 cGy to 1000 cGy. *Med Phys* 1999; 26: 1010-6.

[120]. Meigooni AS, Mishra V, Panth H, Williamson J. Instrumentation and dosimeter-size artifacts in quantitative thermoluminescence dosimetry of low-dose fields. *Med Phys* 1995; 22: 555-61.

[121]. Kutcher GJ, Coia L, Gillin M, et al. Comprehensive QA for radiation oncology: report of AAPM Radiation Therapy Committee Task Group 40. *Med Phys* 1994; 21: 581-618.

[122]. Thuc P. Simulation of the transmitted dose in EPID using a Monte Carlo Method. *MSc thesis, University of Adelaide* 2009.

[123]. Das IJ, Desobry GE, McNeeley SW, Cheng EC, Schultheiss TE. Beam characteristics of a retrofitted double-focused multileaf collimator. *Med Phys* 1998; 25: 1676-84.

[124]. Kawrakow I, Rogers DWO. The EGSnrc code system: Monte Carlo simulation of electron and photon transport. Ottawa, National Research Council of Canada, 2003.

[125]. Sheikh-Bagheri D, Rogers D, Ross C, Seuntjens J. Comparison of measured and Monte Carlo calculated dose distributions from the NRC linac. *Med Phys* 2000; 27: 2256-66.

[126]. Kawrakow I, Rogers DWO, Walters B. Large efficiency improvements in BEAMnrc using directional bremsstrahlung splitting. *Med Phys* 2004; 31(10): 2883-98.

[127]. Central axis depth dose data for use in radiotherapy. A survey of depth doses and related data measured in water or equivalent media. *Br J Radiol Suppl* 1983; 17: 1-147.

[128]. Jacobs H. Breast conserving therapy: Experience with HDR Afterloading Iridium-192 implants. In: Martinez AA, Orton CG, Mould R, eds. *Proceedings Brachytherapy Meeting Remote Afterloading: State of the Art*. Dearborn, Michigan, USA: Nucletron Corporation, 1989: 251-6.

[129]. Mackie TR, Scrimger JW, Battista JJ. A convolution method of calculating dose for 15-MV x rays. *Med Phys* 1985; 12: 188-96.

[130]. Low DA, Dempsey JF. Evaluation of the gamma dose distribution comparison method. *Med Phys* 2003; 30: 2455-64.

[131]. Low DA, Harms WB, Mutic S, Purdy JA. A technique for the quantitative evaluation of dose distributions. *Med Phys* 1998; 25: 656-61.

[132]. Agazaryan N, Solberg TD, DeMarco JJ. Patient specific quality assurance for the delivery of intensity modulated radiotherapy. *J Appl Clin Med Phys* 2003; 4: 40-50.

[133]. Kaus MR, Brock KK, Pekar V, Dawson LA, Nichol AM, Jaffray DA. Assessment of a model-based deformable image registration approach for radiation therapy planning. *Int J Radiat Oncol Biol Phys* 2007; 68: 572-80.

[134]. Yan D, Jaffray DA, Wong JW. A model to accumulate fractionated dose in a deforming organ. *Int J Radiat Oncol Biol Phys* 1999; 44: 665-75.

[135]. Moore CS, Liney GP, Beavis AW. Quality assurance of registration of CT and MRI data sets for treatment planning of radiotherapy for head and neck cancers. *J Appl Clin Med Phys* 2004; 5: 25-35.

[136]. Lu W, Olivera GH, Chen Q, et al. Deformable registration of the planning image (kVCT) and the daily images (MVCT) for adaptive radiation therapy. *Phys Med Biol* 2006; 51: 4357-74.

[137]. Foskey M, Davis B, Goyal L, et al. Large deformation three-dimensional image registration in image-guided radiation therapy. *Phys Med Biol* 2005; 50: 5869-92.

[138]. Loeckx D, Slagmolen P, Maes F, Vandermeulen D, Suetens P. Nonrigid image registration using conditional mutual information. *IEEE Trans Med Imaging* 2009; 29: 19-29.

[139]. Rueckert D, Aljabar P, Heckemann RA, Hajnal JV, Hammers A. Diffeomorphic registration using B-splines. *Med Image Comput Comput Assist Interv* 2006; 9: 702-9.

[140]. Rueckert D, Sonoda LI, Hayes C, Hill DL, Leach MO, Hawkes DJ. Nonrigid registration using free-form deformations: application to breast MR images. *IEEE Trans Med Imaging* 1999; 18: 712-21.

[141]. Christensen GE, Rabbitt RD, Miller MI. Deformable templates using large deformation kinematics. *IEEE Trans Image Process* 1996; 5: 1435-47.

[142]. Studholme C, Drapaca C, Iordanova B, Cardenas V. Deformation-based mapping of volume change from serial brain MRI in the presence of local tissue contrast change. *IEEE Trans Med Imaging* 2006; 25: 626-39.

[143]. Shen D, Davatzikos C. HAMMER: hierarchical attribute matching mechanism for elastic registration. *IEEE Trans Med Imaging* 2002; 21: 1421-39.

[144]. Nithiananthan S, Brock KK, Daly MJ, Chan H, Irish JC, Siewerdsen JH. Demons deformable registration for CBCT-guided procedures in the head and neck: convergence and accuracy. *Med Phys* 2009; 36: 4755-64.

[145]. Vercauteren T, Pennec X, Perchant A, Ayache N. Non-parametric diffeomorphic image registration with the demons algorithm. *Med Image Comput Comput Assist Interv* 2007; 10: 319-26.